A Rigorous Test of Bell's Inequality and Quantum Teleportation Employing Single Atoms

Daniel Burchardt

München 2017

A Rigorous Test of Bell's Inequality and Quantum Teleportation Employing Single Atoms

Daniel Burchardt

Dissertation
an der Fakultät für Physik
der Ludwig–Maximilians–Universität
München

vorgelegt von
Daniel Burchardt
aus Augsburg

München, den 06.12.2017

Erstgutachter: Prof. Dr. Harald Weinfurter
Zweitgutachter: Prof. Dr. Immanuel Bloch
Tag der mündlichen Prüfung: 02.02.2018

Zusammenfassung

1935 verwiesen Einstein, Podolsky und Rosen auf Widersprüche zwischen der Quantenmechanik und klassischen Theorien, die auf den Prinzipien Realismus (physikalische Eigenschaften existieren unabhängig von Beobachtung) und Lokalität (Wechselwirkung zwischen Teilchen kann sich nicht schneller als mit Lichtgeschwindigkeit ausbreiten) basieren. Insbesondere die starken Korrelationen zwischen den Messresultaten verschränkter Teilchen bekräftigten ihre Folgerung, dass die Quantenmechanik unvollständig sei. Auf Grundlage dieser Analyse wurde eine Erweiterung der Quantenmechanik mit zusätzlichen Parametern, sogenannten lokal verborgenen Variablen (LHV), vorgeschlagen, um eine komplette, lokal-realistische Theorie zu erhalten. Eine Methode, um experimentell zu überprüfen, ob die Natur durch eine lokal-realistische Theorie beschrieben werden kann, ist ein Test der Bell'schen Ungleichung, der eine Grenze für Korrelationen zwischen zwei Teilchen bietet, die mit LHVs beschrieben werden. Durch die starken Hinweise der seit den 1970ern durchgeführten Experimente gegen lokal-realistische Theorien ist es wünschenswert, solche Experimente mit einer minimalen Anzahl an Annahmen durchzuführen, um Schlupflöcher zu vermeiden, die trotz der Messungen eine lokal-realistische Beschreibung zulassen. Das erste bedeutende Schlupfloch betrifft die Lokalität. Es kann vermieden werden, wenn die Messungen raumartig getrennt durchgeführt werden. Das zweite ist das Detektionsschlupfloch, das entsteht, wenn ein unzureichender Anteil an Teilchen detektiert wird und man annehmen muss, dass die detektierten Teilchen eine faire Stichprobe bilden. Bis vor kurzem konnte keiner der durchgeführten Bell Tests beide Schlupflöcher gleichzeitig schließen.

Diese Dissertation präsentiert einen genauen Test der Bell'schen Ungleichung, in dem sowohl das Detektions- als auch das Lokalitätsschlupfloch geschlossen werden. Dazu werden zwei verschränkte $^{87}\mathrm{Rb}$ Atome verwendet, die $398\,\mathrm{m}$ voneinander getrennt sind. Zur Verschränkung der Atome über diese Distanz wird das „entanglement swapping" Protokoll verwendet. Zuerst wird jedes Atom mit einem spontan emittierten Photon verschränkt. Projektion der Photonen auf einen verschränkten Zustand erzeugt Verschränkung zwischen den Atomen, auch über große Distanzen. Der Nachweis der Verschränkung zwischen zwei entfernten Atomen ist eine große Herausforderung. Der experimentelle Ablauf beinhaltet Zeitverzögerungen zwischen der Erzeugung der Atom-Photon Verschränkung und der Zustandsanalyse von etwa $11\,\mu\mathrm{s}$, was eine Erhaltung des Atomzustands mit hoher Fidelity auf dieser Zeitskala erfordert. Die relevanten Zeemanzustände des Atoms sind empfindlich auf magnetische und optische Felder, die zur Dephasierung der Atomzustände führen. Wichtige Verbesserungen der Kompensation magnetischer Felder und eine Analyse der Dephasierungsmechanismen gefangener Atome ermöglichten es uns, die erforderte Stabilität zu erreichen.

Die Bell'sche Ungleichung wird durch schnell durchgeführte Korrelationsmessungen an getrennten Atomen getestet, wobei die Messrichtungen von einem Quantenzufallszahlengenerator bestimmt werden. In unserem Test erhielten wir für 10000 gemessene Ereignisse eine Verletzung

der Bell'schen Ungleichung von $S = 2.222 \pm 0.033$, verglichen mit dem für lokal-realistische Theorien maximalen Wert von $S = 2$. Die Möglichkeit, dass das Experiment lokal-realistisch erklärt werden kann, ist mit einem statistischen Signifikanzlevel (p-Wert) von 1.739×10^{-10} ausgeschlossen. Die Verletzung ist sehr signifikant und schließt fast alle LHV-Theorien aus.

Eine weitere Anwendung der Atom-Photon Verschränkung ist Quantenteleportation, eines der wichtigsten Protokolle der Quantenkommunikation. Es ermöglicht die Übertragung eines unbekannten Quantenzustands auf ein anderes Quantensystem. Diese Dissertation präsentiert die Teleportation des Polarisationszustands eines abgeschwächten Laserpulses auf ein Rb Atom über eine Distanz von $20\,\mathrm{m}$. Obwohl eine Laserquelle keine ideale Einzelphotonenquelle darstellt, konnten wir, durch die hohe Qualität der atomaren Einzelphotonenquelle, Fidelities des teleportierten Zustands von mehr als 0.76 erreichen.

Abstract

In 1935, Einstein, Podolsky, and Rosen pointed at contradictions between quantum mechanics and classical theories which obey the principles of realism (physical properties exist without observation) and locality (interactions between particles can propagate at most at the speed of light). In particular, the strong correlations between the measurement results of particles in an entangled state supported their conclusion that quantum mechanics is incomplete. On the basis of this analysis, an extension of quantum mechanics by additional parameters, now called local hidden variables (LHVs), was suggested to achieve a complete, local-realistic theory. A method to test experimentally whether nature can be described in a local-realistic way is a test of Bell's inequality which provides a bound for correlations between particles governed by LHVs. Given the strong evidence against local-realistic theories achieved with Bell tests since the 1970s, it is desirable to perform such experiments with a minimal set of assumptions to avoid so-called loopholes enabling LHV-theories to describe the results. The first major loophole is the locality loophole that can be avoided by performing space-like separated measurements on the particles to exclude any communication. The second one is the detection efficiency loophole which opens if an insufficient fraction of particles is detected and one has to assume that the measured particles fairly represent the entire sample. Until recently, no Bell test could close both loopholes simultaneously.

This thesis presents a rigorous test of Bell's inequality closing both the detection efficiency and the locality loophole employing two entangled $^{87}\mathrm{Rb}$ atoms separated by a distance of $398\,\mathrm{m}$. To generate entanglement of atoms over this distance we use the entanglement swapping protocol. Each atom is first entangled with a photon which is emitted in a spontaneous decay. A joint measurement of the photons then projects the atoms onto an entangled state. Observing long-distance entanglement of atoms is a challenging task. The experimental sequence includes time delays between the generation of the initial atom-photon entanglement and the final atomic state analysis of about $11\,\mu\mathrm{s}$ which requires to preserve the atomic states on this time scale with very high fidelity. The relevant Zeeman states of the atom are susceptible to magnetic and optical fields which lead to dephasing. Major improvements of the compensation of magnetic fields and analyzing dephasing mechanisms of the trapped atoms allowed us to provide the required stability of the atomic states.

Bell's inequality was tested by performing fast correlation measurements on separated atoms using analysis directions determined by a quantum random number generator. For 10000 measured events, we obtain a violation of Bell's inequality of $S = 2.222 \pm 0.033$ compared to the limit for local-realistic theories of $S = 2$. This rules out any explanation with local-realistic theories with a statistical level of significance (p-value) of 1.739×10^{-10}. The obtained violation thus is very significant and rejects almost all classes of LHV-theories.

A further application of atom-photon entanglement is quantum teleportation, one of the most

important protocols in quantum communication. It allows the transfer of an unknown quantum state to another quantum system. In this work, the teleportation of the polarization state of an attenuated laser pulse onto a Rb atom over a distance of $20\,\mathrm{m}$ is presented. Although a laser is not an ideal source of single photons for this purpose, the high quality of the atomic source of single photons still allowed to reach fidelities of the teleported state of more than 0.76.

Contents

1. Introduction **1**

2. Basics of the experiment **5**
2.1. Atomic quantum system 5
2.2. Laser and vacuum system 5
2.3. Trapping single atoms 7
2.3.1. Magneto optical trap (MOT) 7
2.3.2. Optical dipole trap (ODT) 8
2.3.3. Confocal microscope setup 9
2.4. Atom-photon entanglement 9
2.5. Atomic state readout 10
2.5.1. State-selective ionization 11
2.5.2. Limitations of the state analysis 13
2.5.3. Performance of the scheme 14
2.6. Atom-atom entanglement 15
2.6.1. Entanglement swapping 15
2.6.2. Photonic Bell-state projection 16
2.6.3. Two-photon interference 17

3. Quantum teleportation of the polarization state of a laser pulse onto an atom **18**
3.1. Theoretical concept 18
3.2. Requirements for the Bell-state measurement 20
3.2.1. Overlap of photons from different sources 20
3.2.2. Attenuation of the laser pulse 20
3.2.3. Achievable event rate 24
3.3. Setup and experimental procedure 25
3.3.1. Atom-photon entanglement 25
3.3.2. Preparation of the laser pulses 28
3.3.3. Connection and communication links 32
3.4. Experimental quantum teleportation 33
3.4.1. Fidelity estimation 33
3.4.2. Results and analysis 35
3.5. Summary 39

4. Towards long-distance atom-atom entanglement 41
4.1. Location and control of the experiment . . . 41
4.1.1. Map of the trap locations . . . 41
4.1.2. Control and synchronization . . . 43
4.2. Experimental sequence . . . 44
4.2.1. Loading of two atom traps . . . 44
4.2.2. Excitation sequence . . . 45
4.2.3. Photon detection and switching to state measurement . . . 46
4.2.4. Signal transmission times . . . 46
4.3. Optimization of the event rate . . . 47
4.3.1. State preparation by optical pumping . . . 47
4.3.2. Improving the pumping scheme . . . 49
4.3.3. Measuring the pumping efficiency . . . 50
4.4. Repetition rate and expected event rate . . . 50
4.5. Summary . . . 51

5. Coherence properties of the atomic qubit 53
5.1. Atomic state evolution in magnetic and optical fields . . . 53
5.1.1. Zeeman effect in a spin-1 system . . . 53
5.1.2. Compensation of magnetic fields . . . 57
5.1.3. Drifts of the feedback sensor . . . 59
5.1.4. Calibration of the feedback sensor . . . 62
5.1.5. Preventing errors in the calibration program . . . 65
5.1.6. AC-Stark effect in the dipole trap . . . 66
5.1.7. Long-term stability . . . 69
5.2. Effects of strong focusing and oscillation of the atoms in the dipole trap . . . 71
5.2.1. Polarization of the dipole trap beam around the focus . . . 71
5.2.2. Time evolution of states for an atom in the field of the ODT . . . 72
5.2.3. Simulation of atomic oscillations . . . 75
5.2.4. Analysis of the atomic state evolution . . . 79
5.3. Atomic state analysis after the time delay . . . 85
5.3.1. Atom-photon correlation measurements and error analysis . . . 85
5.3.2. Calibration for two-atom experiments . . . 88
5.4. Summary . . . 89

6. Violation of Bell's inequality simultaneously closing the detection and the locality loophole 91
6.1. Bell's inequality . . . 91
6.2. Loopholes . . . 92
6.2.1. Detection efficiency loophole . . . 92
6.2.2. Locality loophole . . . 93
6.2.3. Closing the two main loopholes in one experiment . . . 93
6.2.4. Further frequently mentioned loopholes . . . 93

6.3. Closing the locality loophole . . . 94
6.3.1. Atomic state analysis . . . 94
6.3.2. Timings of the state analysis procedure . . . 98
6.3.3. Space-like separation . . . 100
6.4. Experimental results . . . 101
6.4.1. Evaluation of Bell's inequality . . . 101
6.4.2. Analysis of the results . . . 101
6.4.3. Hypothesis test . . . 103
6.5. Summary . . . 104

7. Summary and Outlook **105**

A. Physical constants and abbreviations **107**

B. Laser system and transition frequencies **108**

C. Photonic and atomic measurement bases **110**

D. Quantum teleportation scheme **113**

E. Calculation of the magnetic field generated by the MOT coils **115**

Bibliography **115**

1. Introduction

The successful development of quantum mechanics in the first half of the 20th century opened a fast advancing field in physics. It enabled the explanation of phenomena, in particular in the microscopic domain, that were not understood before and it made a variety of new predictions. In quantum mechanics, the description of the state of a quantum system has special features. Without a measurement, the quantum system can be in a coherent superposition of several states. The measurement then projects the system onto an eigenstate of the observable. One key element in quantum mechanics is entanglement. Entangled particles are in a common quantum state that can not be expressed as a product of two independent states. The measurable physical properties of such particles show strong correlations that have no analogy in what is nowadays called "classical" physics. The very special features of quantum mechanics are the basis for the fields of quantum information and quantum communication, but they also caused skepticism about this theory due to the necessity of abandoning certain well-established (classical) concepts.

In 1935, Einstein, Podolsky, and Rosen questioned the completeness of quantum mechanics by pointing at contradictions (the so-called EPR-paradox) when observing two particles in a common quantum state. In their famous publication "Can quantum-mechanical description of physical reality be considered complete?" [1] they assumed that a suitable theory should obey the principles of locality and realism. Locality thereby means that any influence and signal can propagate at most at the speed of light such that if the particles can be separated by a sufficient distance there is no interaction between them. As criterion for realism they demanded that if a physical quantity can be predicted with certainty, then there is an element of physical reality that corresponds to this quantity. They found that in the case of observing non-commuting observables, quantum mechanics is in contradiction with these principles and concluded that the theory of quantum mechanics might be incomplete.

If quantum mechanics is incomplete the question arises if it can be extended. Therefore, the introduction of additional parameters in a quantum state (called local hidden variables (LHV)) was suggested that predetermine the measurement results of particles. With the help of LHVs, quantum mechanics could be formulated as local-realistic theory. However, there was no possibility to experimentally test the existence of such hidden variables until John Bell in 1964 found statistical bounds for LHV-theories that do not hold for quantum mechanics [2]. He considered Stern-Gerlach measurements on spin-$1/2$ particles in the singlet state and analyzed the expectation values of measurements under the assumption that they are ruled by a LHV-theory. The central result is that the statistical predictions of quantum mechanics cannot be reproduced with parameters that predetermine the measurement outcomes. This conflict is expressed in Bell's inequality that can be tested in experiments. Since then, the aim has been to experimentally test Bell's inequality where a violation would exclude the possibility of LHVs. Later, Clauser, Horne, Shimony and Holt (CHSH) developed a formulation that is more suitable for experiments [3]. It

requires measurements of correlations between the two particles in 4 different combinations of measurement directions which allows to evaluate a characteristic parameter (often called S). The CHSH-inequality then states that this parameter is bounded by $S \leq 2$ for local-realistic theories. On the contrary it can reach values of up to $S = 2\sqrt{2}$ in quantum mechanics. First experiments of Bell's inequality agreed with the predictions of quantum mechanics [4, 5, 6], however, due to experimental imperfections they had to rely on additional assumptions. Thus they left open so-called loopholes for local-realistic descriptions. The two main loopholes are the locality and the detection efficiency loophole. To close the locality loophole on the one hand, the measurements on the two particles must not influence each other, requiring space-like separation. On the other hand, to avoid the detection efficiency loophole, a sufficient fraction of particles has to be detected to guarantee fair sampling of the measured pairs. It required vast improvements of experimental methods to close, in a first step, the locality [7] and the detection efficiency loophole [8, 9, 10] individually. However, by closing only one of the two loopholes, local-realistic descriptions are still allowed.

Because of the importance of the fundamental results provided by Bell tests, the final aim is to close all loopholes in a single experiment. Very recently this was achieved for the two main loopholes by different groups [11, 12, 13, 14] as well as in this thesis [15]. Our approach thereby relied on fast correlation measurements on two atoms that are entangled over a distance of $398\,\mathrm{m}$. Although it seems to be clear by now that the observed phenomena with entangled particles can not be explained by a local-realistic theory, the work to further reduce assumptions in Bell tests continues. While the mentioned experiments used physical quantum random number generators [16, 17] to guarantee independence of the measurement settings, latest experiments were performed with "cosmic" random numbers extracted from the light of stars [18]. This enables to avoid assumptions on the randomness of the generators, e.g. that the random number does not depend on any process or event in the past (up to hundreds of years). The progress in the experimental realizations nowadays leave little space for remaining local-realistic formulations of physics.

Meanwhile, the generation of entangled particles has reached a very high level of the achievable fidelities of entangled states in a variety of quantum systems. After the first demonstrations of entanglement achieved with photons emitted in an atomic cascade [19], entanglement was realized in many quantum systems using different techniques. An important achievement was the generation of hybrid entanglement between an atom and a photon [20, 21, 22]. This hybrid system consists of a stationary matter particle, that is favorable for storing quantum information, and a mobile photon which can be transfered to distant locations. The generation of long-distance atom-photon entanglement is a crucial step towards the entanglement of two atoms over a long distance. Consequently, this was reached both by a direct atom-photon interaction [23] based on the coherent absorption of the photon and by using the entanglement swapping protocol [24]. The latter requires the generation of two entangled atom-photon pairs at a certain distance. The photons are sent to a measurement apparatus that projects them onto a maximally entangled Bell-state. This joint measurement projects the atoms onto an entangled state [25]. Besides using atoms, there are similar techniques to generate entanglement between other quantum systems and photons which was for example used to generate entanglement between electron spins in color centers (NV-centers) in diamond [26].

Long-distance entanglement of particles enables several applications in quantum communication. It allows performing secure communication by using quantum key distribution (QKD) protocols with entangled particles [27]. The security proof thereby relies on a violation of Bell's inequality. By using loophole-free violations of Bell's inequality, these protocols can be extended to provide security even if the measurement devices themselves are not trustworthy. Proposals for such device-independent QKD (DIQKD) schemes and the respective security proofs are already developed [28, 29, 30], but they have not been realized in experiments yet, due to their high experimental requirements. Another achievement in quantum communication is the teleportation of quantum states between remote locations [31, 32]. By splitting and distributing an entangled pair of particles to the two locations as a resource, the transfer of an arbitrary quantum state from one location to the other is possible without moving the particle itself. This method works for many different types of particles and different degrees of freedom. Recently, complex systems were used for teleportation, e.g., the simultaneous teleportation of two degrees of freedom of a photon was reported [33]. While most experiments do not exceed teleportation distances of several meters, it has already been demonstrated over several kilometers [34, 35, 36].

To provide entanglement of stationary particles over even longer distances is difficult due to losses of photons in fibers which increase exponentially with the distance. A solution could be the development of quantum repeaters [37]. By combining methods to generate entangled stationary particles over a long distance with quantum repeaters the development of a large-scale quantum network [38] is possible that consists of many quantum nodes. Quantum information can then be sent between the nodes, e.g. by quantum teleportation.

This work presents experiments on long-distance atom-photon and atom-atom entanglement with neutral Rubidium 87 atoms. There are two key parts of this thesis, the first one being quantum teleportation of the polarization state of an attenuated laser pulse onto an atom at a distance of $20\,\mathrm{m}$. This demonstrates the possibility to use a laser source for quantum teleportation even though it has fundamental differences to the usually used single-photon sources. The second and larger part of this thesis is about the generation of atom-atom entanglement over $398\,\mathrm{m}$ which enables a violation of Bell's inequality with both the detection efficiency and the locality loophole closed. I will focus on the challenges to generate atom-atom entanglement over the large distance and to measure the atomic states with high fidelity. Together with a fast atomic state analysis, this allows us to perform space-like separated measurements that are crucial to close the locality loophole. By simultaneously closing the detection efficiency loophole which was already achieved in earlier experiments in our group [25], Bell's inequality was violated avoiding the two major loopholes in a single experiment.

The structure of this thesis is the following. Chapter 2 introduces the basic principles of the experiment that were already developed in previous work. This includes the trapping of single $^{87}\mathrm{Rb}$ atoms, the generation of atom-photon and atom-atom entanglement, and the employed methods to measure the atomic states. In chapter 3, I will present the quantum teleportation experiment and in particular discuss requirements for the laser source in order to reach high fidelities of the teleported state. This method is then used to transfer different states onto the atom located in another laboratory at a distance of $20\,\mathrm{m}$. From chapter 4 on the focus will be on the atom-atom entanglement experiments over $398\,\mathrm{m}$. While chapter 4 deals with the generation of entanglement, chapter 5 will discuss the relevant coherence properties necessary to analyze

the atomic states with high fidelity. Finally, in chapter 6, I will present the experimental details and results of the performed Bell test that violates Bell's inequality with significant statistics and therefore allows to exclude almost all classes of LHV-theories for the description of nature.

2. Basics of the experiment

Generation of long-distance atom-photon and atom-atom entanglement as needed for this work requires a setup with a high degree of control of the quantum systems which was developed in several PhD theses over the last years [39, 40, 41, 42, 43, 44, 45]. In this chapter I will summarize the basics of this experiment, including the results of previous work and the theoretical concepts that form the basis for this thesis.

2.1. Atomic quantum system

Our quantum system of choice is a single, neutral $^{87}\mathrm{Rb}$-atom. Rubidium is an alkaline atom with one valence electron and a well known level structure and transitions [46]. $^{87}\mathrm{Rb}$ has a nuclear spin of $I = \frac{3}{2}$, leading to a hyperfine structure of which the relevant levels are shown in the level diagram in figure 2.1. The ground level $5^2S_{1/2}$ splits into the hyperfine levels $F = 1$ and $F = 2$. Hyperfine levels of the two relevant excited levels $5^2P_{1/2}$ and $5^2P_{3/2}$ are denoted by F'. The atomic qubit is encoded in the Zeeman states $m_F = \pm 1$ of the level $5^2S_{1/2},\ F = 1$ with the state $|m_F = -1\rangle_z$ corresponding to the spin state $|\downarrow\rangle_z$ and $|m_F = +1\rangle_z$ corresponding to the spin state $|\uparrow\rangle_z$. The degeneracy of the three ground states with $F = 1$ is lifted in magnetic and optical fields. In the absence of such shifts, the ground states are stable and long coherence times of the qubit are possible. The qubit states form a Λ-type structure with the level $5^2P_{3/2},\ F' = 0$ which is used to generate atom-photon entanglement [41]. Furthermore, $5^2S_{1/2},\ F = 2 \rightarrow 5^2P_{3/2},\ F' = 3$ is a closed transition which can be used for efficient laser cooling.

2.2. Laser and vacuum system

One technical advantage in using Rubidium is the availability of laser diodes at wavelengths matching the atomic transitions, especially the D1 and D2 line at $780.24\,\mathrm{nm}$ and $794.98\,\mathrm{nm}$, which are commercially available. They are operated with an external grating [47], allowing for frequency stabilization to the required transitions using Doppler-free saturation spectroscopy. Different hyperfine levels of the excited states are then addressed by fine-tuning the light frequency with acousto-optic modulators (AOMs). A scheme of the used laser transitions and their labeling can be found in appendix B.

Experiments with single trapped atoms require an ultra-high vacuum (UHV) (in our case about $10^{-10}\,\mathrm{mbar}$) to avoid interactions with the residual gas. This is achieved by using a vacuum chamber that is evacuated and the pressure is maintained by an ion-getter pump (Varian, UHV-24p). The atom trap is located in a glass cell that is attached to the vacuum chamber and provides

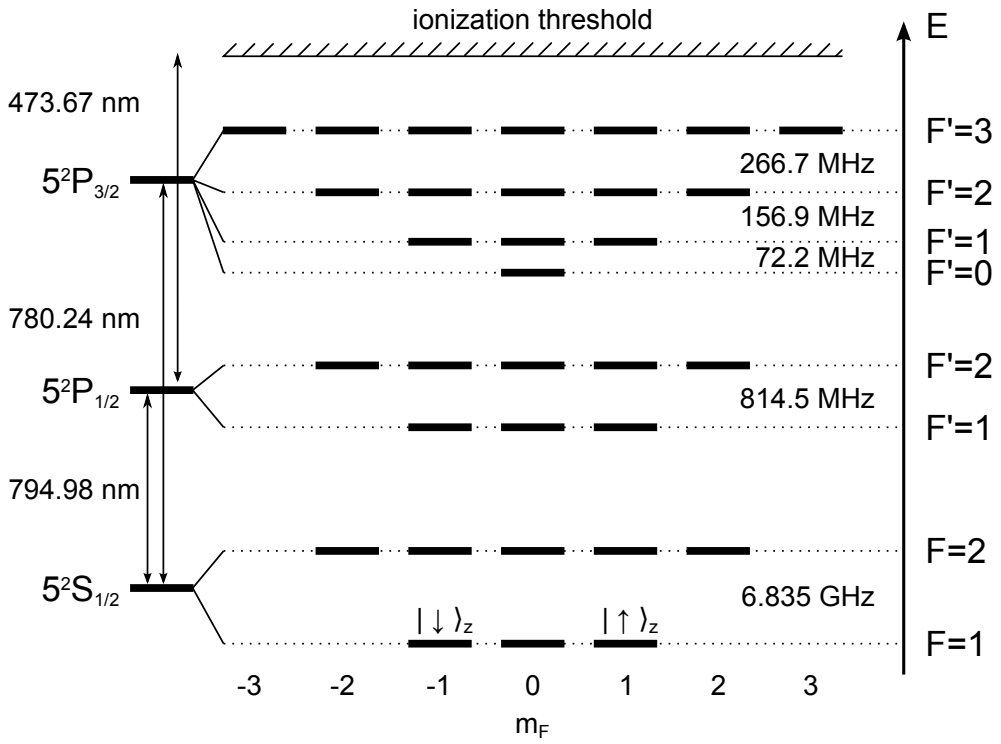

Figure 2.1.: Level scheme of $^{87}\mathrm{Rb}$. The ground level $5^2S_{1/2}$ splits into the hyperfine levels $F = 1$ and $F = 2$ separated by $6.835\,\mathrm{GHz}$. The atomic qubit is encoded in the Zeeman states $|\downarrow\rangle_z = |m_F = -1\rangle_z$ and $|\uparrow\rangle_z = |m_F = +1\rangle_z$ of the $F = 1$ ground level. Also shown are the states of the first two excited levels $5^2P_{1/2}$ and $5^2P_{3/2}$ that are coupled to the ground state with different lasers at wavelengths of $780.24\,\mathrm{nm}$ and $794.98\,\mathrm{nm}$. The ionization threshold of the $5^2P_{1/2}$ level is at a wavelength of $473.67\,\mathrm{nm}$.

optical access from most directions. Rubidium is available from a vapor dispenser, which is a small metallic tube that is heated by applying an electric current to vaporize atoms. To increase the lifetime of these dispensers and to reduce the contamination of internal parts of the vacuum setup, we use UV-light to evaporate atoms that stick to the glass cell or other parts of the setup. More details on the design and the properties of the vacuum setup can be found in reference [45].

2.3. Trapping single atoms

Optimal control of an atomic system requires a high level of isolation from external influences. Only then the possible observation times are long enough to execute complex manipulations and measurements on the system. Especially when analyzing single emitted photons, the collection efficiency of the fluorescence by an objective depends on the localization of the single atom. Strong confinement is achieved by using a far off-resonant, tightly focused optical dipole trap (ODT) [48] with a depth of the trapping potential on the order of $k_B \cdot 1\,\mathrm{mK}$. For loading atoms into the shallow ODT potential we use a magneto-optical trap (MOT) that is able to reduce the kinetic energy of atoms [49, 50].

2.3.1. Magneto optical trap (MOT)

Cooling of neutral atoms can be done by radiation pressure using the Doppler effect [51, 52]. A laser beam that is red detuned to an atomic transition will preferentially excite atoms that are moving in the opposite direction of its propagation since their transition frequency is shifted and the detuning is reduced. If this is done with light from all directions (e.g. with 3 beam pairs), the atoms will get decelerated. This process is called Doppler cooling and can reach temperatures down to the so-called Doppler limit which is $146\,\mu\mathrm{K}$ for Rubidium [46]. While this limit is derived for two-level systems, one can go considerably below this temperature by polarization-gradient cooling [53]. To effectively cool the atoms, we use 6 laser beams from different directions (pairwise counter-propagating, all pairs of beams are ideally perpendicular) that are red detuned by $18\,\mathrm{MHz}$ to the atomic transition $5^2\mathrm{S}_{1/2},\ F = 2 \rightarrow 5^2\mathrm{P}_{3/2},\ F' = 3$ (cooling laser). The laser beams are circularly polarized and cross at the center of the trap. Although this transition is closed it is possible that atoms decay to the $F = 1$ ground level if they were off-resonantly excited to $F' = 2$. To maintain the cooling cycle, the cooling beams are overlapped with additional repump beams resonant to the transition $5^2\mathrm{S}_{1/2},\ F = 1 \rightarrow 5^2\mathrm{P}_{3/2},\ F' = 2$.

To achieve in addition a confinement of atoms, a magnetic quadrupole field is generated by coils in an anti-Helmholtz configuration around the vacuum cell. The resulting magnetic field gradient shifts the states of atoms in dependence of their position and, in combination with the cooling beams with appropriate polarization, leads to a force directed towards the center. The MOT forms a cold cloud of several thousands of atoms in a small volume with a diameter of about $1\,\mathrm{mm}$ [39]. The atoms in this cloud have a much lower temperature than at room temperature and their density is increased which enables the loading into the ODT.

2.3.2. Optical dipole trap (ODT)

The optical dipole trap is generated by a tightly focused laser beam at $852\,\mathrm{nm}$ that is far red detuned to the atomic transitions from the ground state. Atoms in this light field experience an AC-Stark shift [54] that lowers the energy of the ground state and forms an attractive potential depending on the local intensity of the laser beam. We use a single Gaussian laser beam that is strongly focused by the objective of a microscope. In this case the AC-Stark shift is maximal at the center of the focus and decreases in all other directions. Therefore, atoms will experience an attractive force towards the center. To achieve an actual single atom trap we use the collisional blockade effect [55]. When the trap volume is small enough, collisions become the dominant loss mechanism if two or more atoms are loaded. This limits the atom number in the trap and loading of more than one atom is not possible. The polarization of the dipole trap laser beam has to be linear in order to shift all Zeeman states of the ground level by the same amount. Otherwise the degeneracy of the ground states would be lifted which leads to undesired decoherence that will be further discussed in chapter 5.

To load atoms into the trap, the center of the MOT and thereby the position of the cold atom cloud is adjusted to the focus of the dipole trap beam. The continuous cooling in the MOT reduces the kinetic energy of particles moving in the focal region and the atoms get trapped in this potential. After the loading operation is finished, the magnetic field of the MOT is switched off. The cooling lasers are further used in certain parts of the experimental sequence to counteract heating and keep the atomic temperature low which increases the lifetime of atoms in the trap.

The geometrical trap parameters are defined by the focal size of the dipole trap beam which has a Gaussian waist of $w_0 = 1.92\,\mu\mathrm{m}$ corresponding to a Rayleigh length of $z_R = 13.6\,\mu\mathrm{m}$. The depth of the trap potential U_0 can be tuned via the power of the dipole trap beam and is set to values of $k_B \cdot 1.6...3.2\,\mathrm{mK}$ depending on the specific requirement. This corresponds to powers of $30...60\,\mathrm{mW}$ which are available from commercially available laser diodes. Assuming a three dimensional harmonic oscillator for the trap potential which is a good approximation for low atomic temperatures this leads to trap frequencies [39]

$$\omega_T = \sqrt{\frac{4\,U_0}{m\,w_0^2}} = 2\pi \cdot 65...92\,\mathrm{kHz}, \tag{2.1}$$

$$\omega_L = \sqrt{\frac{2\,U_0}{m\,z_R^2}} = 2\pi \cdot 9...13\,\mathrm{kHz}, \tag{2.2}$$

where ω_T is the frequency of the motion perpendicular (transversal) to the optical axis of the dipole trap beam and ω_L is the longitudinal frequency along the optical axis. Important influences of the dipole trap on the atomic state were studied in this work and will be shown in detail in chapter 5.

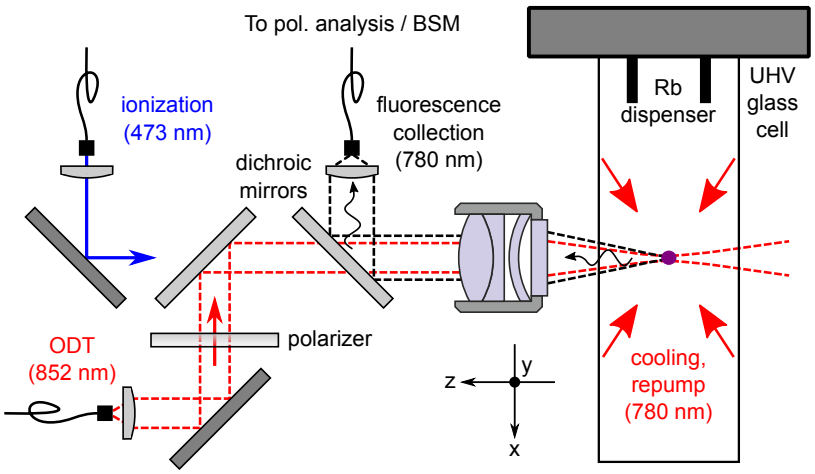

Figure 2.2.: Setup of the confocal microscope used to focus the dipole trap beam and the ionization beam to the atom and to collect fluorescence of the trapped atom. The fluorescence is coupled into an optical single-mode fiber that leads to a polarization analysis or a Bell-state measurement (BSM) apparatus. The shown layout corresponds to the trap 1 setup. Another atom trap (trap 2) used for this work has a different order of dichroic mirrors.

2.3.3. Confocal microscope setup

For observing the trapped atoms the same microscope is used as for focusing the dipole trap beam which results in a confocal arrangement (figure 2.2). The collected fluorescence light is separated from the dipole trap light by a dichroic mirror, coupled into a single-mode fiber and registered by single photon detectors (avalanche photo diodes (APDs)). There, the count rate and the polarization of registered photons is analyzed. Loading of an atom into the trap is verified by a sharp rise of the count rate at the detectors that is caused by collected fluorescence photons from the cooling transition when the position of the trap and the collection optics overlap. This way, during times where the cooling lasers are switched on it is easy to detect the presence of an atom. Once the atom gets lost, indicated by a drop of the observed fluorescence, the setup automatically changes the trap operation and reloads a new atom before the experimental sequence continues. The confocal microscope additionally consists of the optics necessary to focus the ionization laser beam (see section 2.5) at the atom. More details about the layout and characterization of the microscope can be found in reference [45].

2.4. Atom-photon entanglement

Atom-photon entanglement is generated in spontaneous emission from a well-defined state into at least two different final states [21, 40]. In our case, the atoms are prepared in the state $|m_F = 0\rangle_z$ of the $5^2\mathrm{S}_{1/2}$, $F = 1$ level by optical pumping (Details will be discussed in section 4.3.1) and excited to the state $|m_{F'} = 0\rangle_z$ of the $5^2\mathrm{P}_{3/2}$, $F' = 0$ level by a short pulse of the excitation

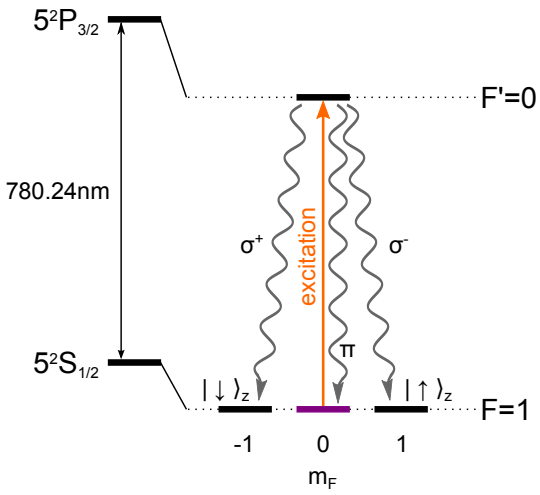

Figure 2.3.: Level scheme and transitions for the atom-photon entanglement generation.

laser that transfers the state population with a high probability to the desired state. The excited state has a life time of $26.2\,\mathrm{ns}$ and the atom decays back to one of the three ground states of the $5^2\mathrm{S}_{1/2},\ F = 1$ manifold by emitting a photon (see figure 2.3). To satisfy the angular momentum conservation, different final states lead to different polarizations of the emitted photons, i.e. σ^+-, σ^-- and π- polarization correspond to decays to the $|m_F = -1\rangle_z$, $|m_F = +1\rangle_z$ and $|m_F = 0\rangle_z$ state, respectively (the polarizations are defined in appendix C). The different radiation characteristics for $\sigma^\pm$- and π-emission allows us to distinguish these decays, since only σ-light is collected along the quantization axis [40]. Therefore, whenever we observe a photon that has been collected by the confocal microscope and coupled into the detection fiber, a σ-decay has occurred and this coherent process results in the entangled atom-photon state

$$|\Psi\rangle_{\mathrm{atom-photon}} = \frac{1}{\sqrt{2}}\left(|\downarrow\rangle_z\,|\sigma^+\rangle + |\uparrow\rangle_z\,|\sigma^-\rangle\right). \tag{2.3}$$

Atom-photon entanglement can be verified by measuring correlations between the photonic polarization and the atomic spin. This is done by collecting the photon into a single-mode fiber that guides the photons to a polarization analysis unit which consists of a polarizing beam splitter (PBS) with single photon detectors (APDs) at each output. A combination of a half- and a quarter wave plate in front of the PBS allows the projection onto an arbitrary polarization state. After the detection of the photon, the atomic state is measured as well. The scheme for the atomic state measurement will be discussed in the next section.

2.5. Atomic state readout

For the experiments described in this thesis, in particular the violation of Bell's inequality, the atomic state measurement has to satisfy the following requirements:

- a simple way to select the measurement basis

- a high fidelity of the atomic state analysis
- a short measurement time to enable space-like separation

Reaching a short measurement time (in the μs-range) is difficult with atomic qubits. Atomic state measurement schemes are mainly based on photon counting where a selected state is excited and decays in a closed transition and where the emitted photons are detected. Due to low detection efficiency of photons ($\approx 10^{-3}$) this cycle has to be repeated many times before it is possible to distinguish whether the transition occurred or not. Fluorescence based state measurements of matter particles using conventional collection optics typically take times in the ms-range and even advanced approaches, e.g. with cavities, need at least a few microseconds [11, 56, 57] which would consequently result in requiring long distances for space-like separation.

2.5.1. State-selective ionization

To avoid these limitations a scheme was developed which is based on state-selective ionization and a direct detection of the ionization fragments [42, 44, 45, 58] (figure 2.4). Atoms in a certain superposition state (bright state $|\Psi_\mathrm{B}\rangle$) of the qubit are excited by a $795\,\mathrm{nm}$ readout laser to the state $|m_{F'}=0\rangle_z$ of the $5^2\mathrm{P}_{1/2}$, $F'=1$ level. Atoms in the orthogonal state (dark state $|\Psi_\mathrm{D}\rangle$) on the contrary are not excited, because the transition is not allowed by selection rules. This gets obvious in the case of a σ^+-polarized readout beam. Then, atoms in the state $|m_F=-1\rangle_z$ are excited, while the respective target state for atoms in the state $|m_F=+1\rangle_z$ does not exist. The same argument holds for the inverse case of σ^--polarization in which atoms in the state $|m_F=+1\rangle_z$ are excited. In general, any polarization of the readout beam can be expressed as superposition of σ^+ and σ^- and the bright and dark states are selected by the polarization $|\chi\rangle$ of the readout beam

$$|\chi\rangle \;=\; \cos(\alpha)|H\rangle + e^{i\phi}\sin(\alpha)|V\rangle, \tag{2.4}$$

with the angles α and ϕ according to

$$|\Psi_\mathrm{B}\rangle \;=\; \sin(\alpha)\,|\uparrow\rangle_x - e^{i\phi}\cos(\alpha)\,|\downarrow\rangle_x\,, \tag{2.5}$$
$$|\Psi_\mathrm{D}\rangle \;=\; \cos(\alpha)\,|\uparrow\rangle_x + e^{i\phi}\sin(\alpha)\,|\downarrow\rangle_x\,, \tag{2.6}$$

with the atomic states $|\uparrow\rangle_x = \frac{1}{\sqrt{2}}\left(|\uparrow\rangle_z + |\downarrow\rangle_z\right)$ and $|\downarrow\rangle_x = \frac{i}{\sqrt{2}}\left(|\uparrow\rangle_z - |\downarrow\rangle_z\right)$ (for transformations between photonic and atomic states see appendix C). The setting of an arbitrary measurement basis is therefore possible by the choice of the polarization of the readout beam.

Atoms in the excited state get directly ionized by a simultaneously applied laser pulse at $473\,\mathrm{nm}$ and the ionization fragments are split into an ion and an electron. This offers the possibility to directly measure the ionization fragments to distinguish between the dark and bright state. The fragments are accelerated in a strong electric field (typical acceleration voltages $3.6\,\mathrm{kV}$...$4.6\,\mathrm{kV}$ [45]) towards two channel-electron-multipliers (CEM) where they impinge on

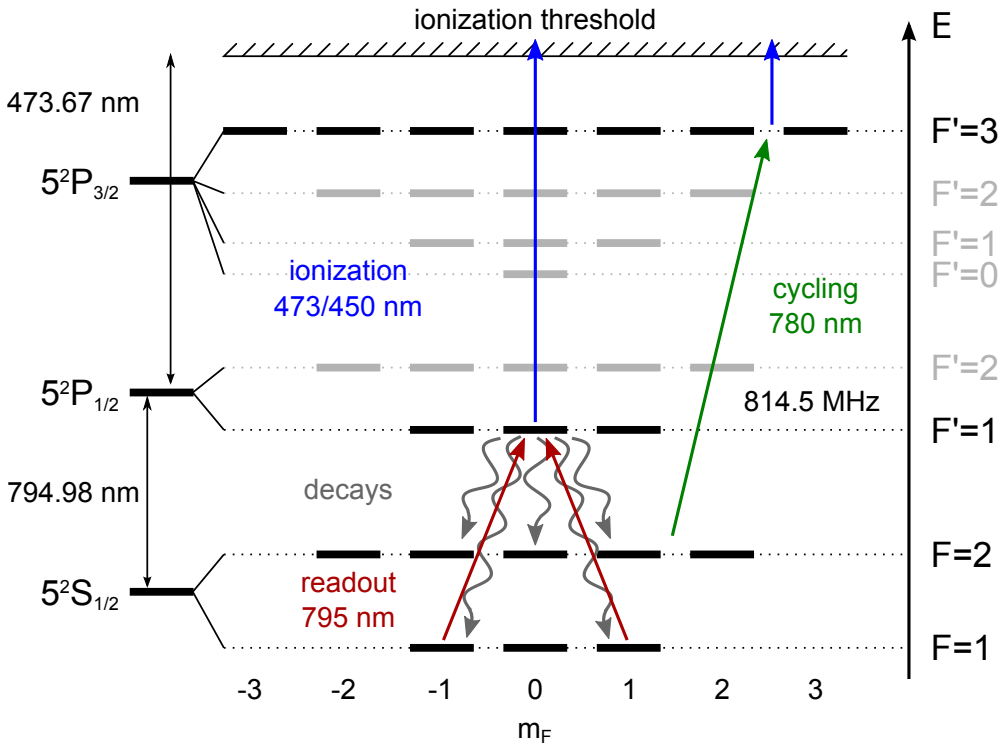

Figure 2.4.: Scheme of the atomic state measurement. Atoms in a selected superposition state (bright state) get excited and directly ionized whereas atoms in the orthogonal dark state are not affected. Possible decays of the excited state before the ionization can, for certain decay channels, be re-excited by the readout or cycling laser.

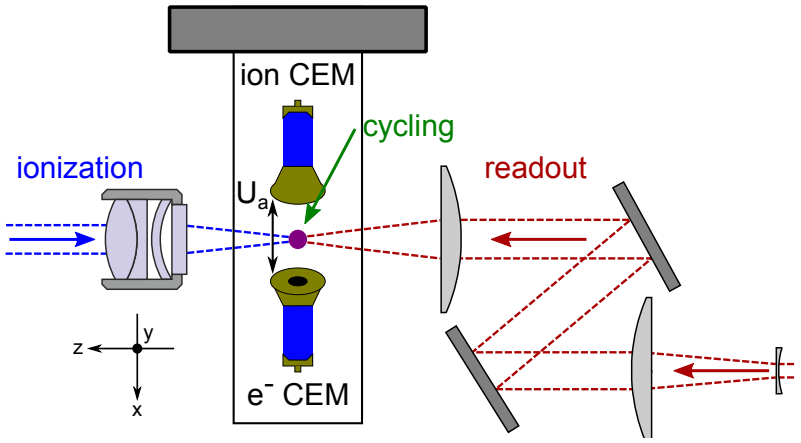

Figure 2.5.: Schematic of the setup with the respective laser beams of the state analysis. The readout and ionization beams are applied from opposite directions along the z-axis. The cycling beam is applied from the top. Channel-electron-multipliers (CEM) are placed inside the vacuum cell to detect the electron and the ion after an ionization event. The acceleration voltage between the two CEMs is $U_\mathrm{a} \approx 3.6\,\mathrm{kV}...4.6\,\mathrm{kV}$.

the active area and initiate an electron avalanche. This avalanche is amplified in a channel with an applied acceleration field and leads to a small current pulse at the rear part of each CEM. A comparator is used to transform this signal into a logic TTL-pulse. Altogether, atoms in the bright state will get excited, ionized and their fragments will cause output signals at the single particle detectors, whereas atoms in the dark state remain unaffected and do not cause such a signal. We thus identify the dark state by the absence of a signal. The setup of the relevant components is shown in figure 2.5.

2.5.2. Limitations of the state analysis

The fidelity of this scheme is limited by the following processes:

1. atoms are ionized despite being in the dark state
2. atoms in the bright state are not ionized
3. both ionization fragments are not detected.

The first one happens when atoms in the dark state get off-resonantly excited to the $F' = 2$ level that is separated by $814.5\,\mathrm{MHz}$ to the resonant transition to $F' = 1$. In this case the atoms will get ionized and give a "wrong" event at the CEM detector. A less likely reason for such events can be a misalignment of the polarization of the readout pulse. When the readout beam is not aligned perfectly parallel to the quantization axis, there can be π-components in the polarization of the readout beam and atoms in the dark state can get excited.

The second effect results mainly from decays of the excited state (figure 2.4). The ionization rate for atoms in the excited state is limited by the applicable intensity of the ionization laser.

Hence, the atom can decay back to the ground state before it gets ionized. Whether this actually reduces the measurement fidelity depends on the final state and therefore the probability for wrong results can be calculated from the Clebsch-Gordan coefficients [46] that give the (relative) transition probabilities P_{rel} for different states. For decays to the bright state ($P_{rel} = \frac{1}{12}$) the atom can be excited again by the readout pulse and will be ionized as well. Therefore, this fraction does not limit the measurement fidelity. The most likely decay is to one of the sub-states of the $F = 2$ level ($P_{rel} = \frac{5}{6}$). For these cases, we use an additional laser (called cycling) to excite the atom to the $F' = 3$ level from where it is also ionized. Therefore, the only contribution of decays which actually decreases the measurement fidelity is a decay to the dark state ($P_{rel} = \frac{1}{12}$). From this state the atom can not be ionized anymore and the measurement provides the wrong result.

The third limitation is caused by the finite detection efficiency of the CEMs. They are in the range of $\eta_\mathrm{e} = 0.75...0.9$ for detecting electrons and $\eta_\mathrm{i} = 0.9...0.94$ for detecting ions. Since the background is negligible, detection of one fragment is already enough to determine the atomic state yielding a combined detection efficiency of $\eta \gtrsim 0.98$.

2.5.3. Performance of the scheme

As measure for the quality of the state measurement we use the maximal contrast. It is determined by preparing atoms in the dark and bright state of a certain basis and evaluating the probability to correctly analyze the state. The maximal contrast is then the probability to correctly detect the atoms in the dark state minus the probability for wrong detection events of atoms in the bright state. The achievable contrast of the state-selective ionization scheme was optimized and reaches values as high as $93.8\,\%$ [45].

The measurement time is composed of the maximal time needed to ionize the atoms which is typically about $200\,\mathrm{ns}$ and of the time-of-flight of fragments to the detectors. This time (for ions) is typically several hundred ns providing a total measurement time of about $1\,\mu\mathrm{s}$ [45]. A detailed analysis of all times relevant for the state measurement in a Bell test will be given in chapter 6.

The measurement scheme explained here also allows us to evaluate data with a photon counting method additional to the CEM analysis. This is possible since ionized atoms get lost from the ODT. If the atom was ionized the fluorescence will drop and the accumulated photon counts will be below a specific threshold at background level. If the atom was in the dark state it will stay in the trap and the fluorescence will be above this threshold. This allows us to directly compare the results of both methods and to analyze the detection efficiency of the CEMs. Depending on the purpose the different measurements presented in this thesis are evaluated with one of those analysis modes and will be labeled with fluorescence analysis or CEM analysis. The actual difference between the two methods is however very small in terms of measurement fidelity, but not in terms of measurement time. While the fluorescence analysis counts photons within at least $30\,\mathrm{ms}$, the measurement result of the CEM analysis is available after about $1\,\mu\mathrm{s}$.

2.6. Atom-atom entanglement

To generate atom-atom entanglement we use the entanglement swapping protocol [24, 59] which is a useful tool to generate entanglement over a long distance without the need for a direct interaction between the two particles. In this protocol, the entanglement of two independent atom-photon pairs is transfered onto the atoms by a joint measurement of the photons. The basics of entanglement swapping, the measurement of the photons which projects them onto a Bell-state and the required interference of two photons are discussed in this section.

2.6.1. Entanglement swapping

The application of the entanglement swapping protocol is initiated by first generating entangled atom-photon pairs in two traps. The four particle state can be written in the atomic basis ($|\uparrow\rangle_{x,1/2}$, $|\downarrow\rangle_{x,1/2}$) and the photonic basis ($|H\rangle_{1/2}$, $|V\rangle_{1/2}$) as the tensor product of the two entangled pairs

$$\begin{aligned} |\Psi\rangle &= |\Psi\rangle_{\mathrm{a1-p1}} \otimes |\Psi\rangle_{\mathrm{a2-p2}} \\ &= \frac{1}{2}\left(|\uparrow\rangle_{x,1}|H\rangle_1 + |\downarrow\rangle_{x,1}|V\rangle_1\right) \otimes \left(|\uparrow\rangle_{x,2}|H\rangle_2 + |\downarrow\rangle_{x,2}|V\rangle_2\right) \\ &= \frac{1}{2}\left(|\uparrow\rangle_{x,1}|H\rangle_1|\uparrow\rangle_{x,2}|H\rangle_2 + |\uparrow\rangle_{x,1}|H\rangle_1|\downarrow\rangle_{x,2}|V\rangle_2\right) \\ &+ \frac{1}{2}\left(|\downarrow\rangle_{x,1}|V\rangle_1|\uparrow\rangle_{x,2}|H\rangle_2 + |\downarrow\rangle_{x,1}|V\rangle_1|\downarrow\rangle_{x,2}|V\rangle_2\right). \end{aligned} \tag{2.7}$$

The projection of the photons onto a Bell-state can have 4 possible results, namely the four maximally entangled Bell-states $|\Phi^{\pm}\rangle_{\mathrm{p1-p2}} = \frac{1}{\sqrt{2}}(|HH\rangle \pm |VV\rangle)$ and $|\Psi^{\pm}\rangle_{\mathrm{p1-p2}} = \frac{1}{\sqrt{2}}(|HV\rangle \pm |VH\rangle)$. Expanding and rearranging equation 2.7 with respect to the possible photonic measurement outcomes gives [43]

$$\begin{aligned} |\Psi\rangle &= \frac{1}{2}\left(|\Phi^+\rangle_{\mathrm{a1-a2}}|\Phi^+\rangle_{\mathrm{p1-p2}}\right) \\ &+ \frac{1}{2}\left(|\Phi^-\rangle_{\mathrm{a1-a2}}|\Phi^-\rangle_{\mathrm{p1-p2}}\right) \\ &+ \frac{1}{2}\left(|\Psi^+\rangle_{\mathrm{a1-a2}}|\Psi^+\rangle_{\mathrm{p1-p2}}\right) \\ &+ \frac{1}{2}\left(|\Psi^+\rangle_{\mathrm{a1-a2}}|\Psi^+\rangle_{\mathrm{p1-p2}}\right), \end{aligned} \tag{2.8}$$

thus the detection of a Bell-state of the photons projects the atoms onto the corresponding atomic Bell-state $|\Phi^{\pm}\rangle_{\mathrm{a1-a2}} = \frac{1}{\sqrt{2}}(|\uparrow\uparrow\rangle_x \pm |\downarrow\downarrow\rangle_x)$ and $|\Psi^{\pm}\rangle_{\mathrm{a1-a2}} = \frac{1}{\sqrt{2}}(|\uparrow\downarrow\rangle_x \pm |\downarrow\uparrow\rangle_x)$. An advantage of entanglement swapping is that the detection of the photons "heralds" the generation of atom-atom entanglement, hence whenever the projection onto a Bell-state succeeded the atoms are known to be in an entangled state. This heralding enables so-called "event-ready" schemes that are especially advantageous for Bell-tests [24].

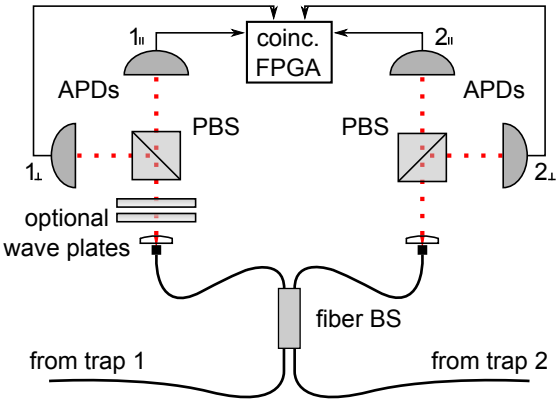

Figure 2.6.: Setup of the Bell-state measurement (BSM) apparatus. Photons from the two traps arrive in optical fibers, are overlapped at a fiber beam splitter (BS) and projected onto a Bell-state. The polarization of photons is analyzed by polarizing beam splitters (PBS) and avalanche photo diodes (APDs). Detection of a photon at APDs $1_{\parallel}$ and $2_{\parallel}$ indicates horizontal polarization of the photon and detection at APDs $1_{\perp}$ and $2_{\perp}$ vertical polarization (without wave plates). An FPGA registers photon detection coincidences (coinc.) in detector combinations that correspond to a Bell-state. Two-photon coincidences at the detectors $1_{\parallel} \wedge 2_{\perp}$ or $1_{\perp} \wedge 2_{\parallel}$ correspond to a $|\Psi^-\rangle$-Bell-state and at the detectors $1_{\parallel} \wedge 1_{\perp}$ or $2_{\parallel} \wedge 2_{\perp}$ to a $|\Psi^+\rangle$-Bell-state.

2.6.2. Photonic Bell-state projection

To perform the Bell-state measurement (BSM), the photons are collected into single-mode fibers and are guided to a Bell-state measurement apparatus shown in figure 2.6. The BSM setup consists of a fiber beam splitter (BS) where the photons are overlapped and polarizing beam splitters (PBS) at each output. Photons are detected with single photon detectors (APDs) behind the PBS. To identify a certain outcome of the photonic measurement we consider the Hong-Ou-Mandel effect [60]. Two photons impinging at the two inputs of a beam splitter have in principle four possibilities to leave the outputs. If the photons are indistinguishable in all degrees of freedom, the amplitudes for different output configurations add which leads to a vanishing amplitude and therefore vanishing probability that the photons are detected in different outputs. In our case the evolution of photons at the beam splitter is calculated individually for the four two-photon Bell-states [43]. The result is that photons will be detected in the same output if they are in one of the three symmetric Bell-states $|\Phi^+\rangle$, $|\Phi^-\rangle$ or $|\Psi^+\rangle$ whereas photons in the antisymmetric $|\Psi^-\rangle$-state will be detected in different outputs. Therefore, a successful BSM is indicated by the detection of photon coincidences in a specific detector combination. Detection clicks of the APDs $1_{\parallel} \wedge 2_{\perp}$ or $1_{\perp} \wedge 2_{\parallel}$ correspond to the detection of photons in the state $|\Psi^-\rangle$ and those of APDs $1_{\parallel} \wedge 1_{\perp}$ or $2_{\parallel} \wedge 2_{\perp}$ to the state $|\Psi^+\rangle$. The interferometric BSM does not allow detecting all four Bell-states which is not possible using only linear optics [61]. Photons in the states $|\Phi^+\rangle$ or $|\Phi^-\rangle$ can not be detected by the setup since they would have the same polarization and appear at the same detector. Even if the detectors could resolve the photon number it is

not possible to distinguish between photons in the states $|\Phi^+\rangle$ and $|\Phi^-\rangle$, because photons in the two states would result in the same detection events. The used setup thus allows to identify two out of four Bell-states, thereby two different entangled atom-atom states can be generated. The detection clicks of the APDs are analyzed by an FPGA that registers coincidences and initiates the measurement of the atomic states.

2.6.3. Two-photon interference

The achievable "quality" of the generated atom-atom state, e.g. its fidelity, strongly depends on the degree of interference of photons. To achieve high fidelities the overlap of the photonic wave functions at the BS has to be maximized in all degrees of freedom, especially the spatial mode overlap, the spectral overlap and the temporal overlap:

- A perfect spatial mode overlap is guaranteed by the use of a single-mode fiber BS. It is very stable and no adjustment is required as it would be the case with free space optics.
- A high degree of spectral overlap of the photons is guaranteed by their common origin from the same decay channel in Rb. As long as the respective levels are not shifted (due to the Zeeman or AC-Stark shift by magnetic or optical fields) their central frequency is the same. The largest remaining impact on a frequency mismatch is caused by the Doppler shift due to the motion of the atoms in the trap. However, the resulting influence on the overlap of the spectral wave functions was found to be small [62].
- To achieve a high temporal overlap the excitation pulses on both sides have to be matched both in their pulse shape and intensity at the position of the atom. Then the temporal wave functions have the same shape that is mainly determined by the excitation pulse and the spontaneous decay with a lifetime of $\tau = 26.2\,\mathrm{ns}$. Temporal overlap is then achieved by synchronizing the excitation pulses and matching the arrival times of photons from both sides.

While these criteria are well fulfilled the remaining limitations of the two-photon interference are detector dark counts and two-photon emission processes of either of the two atoms. They reduce the two-photon interference contrast to values of about 90.5% [43].

The presented scheme enabled our group to entangle two atoms over a distance of $20\,\mathrm{m}$ in 2012 [25]. The data was used for a test of Bell's inequality and allowed a violation with an S-parameter according to CHSH [3] of $S = 2.19 \pm 0.09$. In the event-ready scheme the atomic states are measured whenever entanglement of the atoms is heralded. Every measured event thereby provides a binary measurement result. Therefore, the detection efficiency loophole was closed in the performed Bell test. However, the distance of $20\,\mathrm{m}$ and the long measurement time (several ms) means that the measurements were not space-like separated and the locality loophole remained open. Closing this loophole together with the detection efficiency loophole will be part of this thesis.

3. Quantum teleportation of the polarization state of a laser pulse onto an atom

Quantum teleportation provides the possibility to transfer an arbitrary quantum state onto a distant particle without transporting the particle itself. It thus is an important ingredient of quantum networks [38], where the connection between different nodes or between quantum memories is crucial and direct light-matter interaction is inefficient. A first experimental realization was shown in [63] where the polarization state of one photon was transfered to a distant photon. Later, developments in the field of matter qubits and light-matter interaction enabled the teleportation between two atomic qubits over a certain distance [64, 65]. To get a full set of tools required in quantum communications the development of further methods, especially involving different sources and targets is necessary. In this work, the teleportation of the polarization state of an attenuated laser pulse onto the atomic spin state of single Rubidium atoms is realized. Especially the use of a laser pulse is a very different approach compared to previous experiments using single photon sources for quantum teleportation. While such a source does not appear to be well-suited for this purpose, we could show that in the case of strongly attenuated pulses high fidelities beyond the classical limit can be reached as I will show in this chapter.

3.1. Theoretical concept

The concept of quantum teleportation was first formulated by Bennett, Brassard, Crépeau, Josza, Peres, and Wootters [31]. The aim is to transfer an input quantum state $|\psi\rangle_{\mathrm{I}}$ from location A to location B. The input state in our case is defined by the polarization of the attenuated laser pulse and can in general be expressed by $|\psi\rangle_{\mathrm{I}} = (\beta|L\rangle + \gamma|R\rangle)$ with $|L\rangle$ and $|R\rangle$ corresponding to left and right circular polarization and β, γ being complex numbers. The two sides A and B have to share a pair of entangled particles as a resource. Therefore, an entangled atom-photon pair is generated at location B which is in the state $|\Psi\rangle_{\mathrm{AP}} = \frac{1}{\sqrt{2}}\left(|\uparrow\rangle_z|R\rangle + |\downarrow\rangle_z|L\rangle\right)$ according to the generation scheme (section 2.4). The photon is sent to location A where it undergoes a Bell-state measurement (BSM) with photons from the laser pulse.

To perform the BSM we use the setup explained in section 2.6 that is based on a joint measurement of two single photons. To use this method for our purpose, the attenuated laser pulse has to be described as approximate single photon source. Therefore, we write the photon number state as a weak coherent state in the Fock space [66]

$$|\alpha\rangle \approx \sqrt{1-\alpha^2}|0\rangle + \alpha|1\rangle + O(\alpha^2), \tag{3.1}$$

with the approximation being valid for high attenuations ($\alpha \ll 1$). For the derivation of the teleportation scheme we neglect all terms of higher order ($O(\alpha^2)$) and limit the analysis to events where two-photon coincidences are registered at the detectors of the BSM setup (one photon originating from the atom and one from the laser pulse, the influence of the higher order terms on the fidelity of the process will be discussed in section 3.2.2). In this case, the state of the laser pulse is in good approximation a one-photon Fock state with the polarization state $|\psi\rangle_{\mathrm{I}}$ (since all photons of the laser pulse are in the same polarization state).

Before the BSM the overall state is the product of the input state and the entangled state

$$|\Psi\rangle_{\mathrm{I}} \otimes |\Psi\rangle_{\mathrm{AP}} = (\beta|L\rangle + \gamma|R\rangle)_{\mathrm{I}} \otimes \frac{1}{\sqrt{2}} \left(|\uparrow\rangle_z |R\rangle + |\downarrow\rangle_z |L\rangle\right)_{\mathrm{AP}}. \tag{3.2}$$

Since the BSM is performed in the H/V-basis we have to transform the polarizations into this basis. Additional regrouping of the terms gives

$$\begin{aligned} |\Psi\rangle_{\mathrm{I}} \otimes |\Psi\rangle_{\mathrm{AP}} = & \frac{i}{2\sqrt{2}} \left(|H\rangle|V\rangle - |V\rangle|H\rangle\right)_{\mathrm{IP}} \otimes \left(\beta |\uparrow\rangle_z - \gamma |\downarrow\rangle_z\right)_{\mathrm{A}} \\ & + \frac{i}{2\sqrt{2}} \left(|H\rangle|V\rangle + |V\rangle|H\rangle\right)_{\mathrm{IP}} \otimes \left(\gamma |\uparrow\rangle_z - \beta |\downarrow\rangle_z\right)_{\mathrm{A}} \\ & + \frac{1}{2\sqrt{2}} \left(|H\rangle|H\rangle - |V\rangle|V\rangle\right)_{\mathrm{IP}} \otimes \left(\gamma| |\uparrow\rangle_z + \beta |\downarrow\rangle_z\right)_{\mathrm{A}} \\ & + \frac{1}{2\sqrt{2}} \left(|H\rangle|H\rangle + |V\rangle|V\rangle\right)_{\mathrm{IP}} \otimes \left(\beta| |\uparrow\rangle_z + \gamma |\downarrow\rangle_z\right)_{\mathrm{A}}, \end{aligned} \tag{3.3}$$

where the polarization states are on the left and the atomic states on the right side in every line (a detailed calculation can be found in appendix D). The BSM on IP yields one of the four Bell-states of photons with the probability of 0.25 for each state. After such a measurement the atoms are therefore projected onto the respective superposition of $|\uparrow\rangle_z$ and $|\downarrow\rangle_z$ with amplitudes β and γ of the input state. Thus, the atomic state is equivalent to the photonic input state up to a well-defined unitary transformation depending on the detected photonic Bell-state. A classical communication channel can be used to send the photonic measurement result from A to B and at location B the input state can be reconstructed by applying this unitary transformation. The BSM setup used in this experiment (see section 2.6.2) allows to distinguish between photons in the states $|\Psi^-\rangle$ and $|\Psi^+\rangle$, hence the two respective atomic states

$$|\Phi_1\rangle = \beta |\uparrow\rangle_z - \gamma |\downarrow\rangle_z, \tag{3.4}$$

$$|\Phi_2\rangle = \gamma |\uparrow\rangle_z - \beta |\downarrow\rangle_z, \tag{3.5}$$

can be generated by teleportation for an arbitrary input state. In our case the unitary transformation is not applied. Rather we perform a quantum state tomography to show the success of the state transfer.

3.2. Requirements for the Bell-state measurement

The central component in the experiment is the BSM setup. A two-photon coincidence registered at the detectors of the BSM setup signals the teleportation of the input state onto the atom. In the following, I will analyze the requirements for a successful projection of the photons onto a Bell-state.

3.2.1. Overlap of photons from different sources

The quality of the BSM is crucial for the fidelity of the teleported state. As already mentioned in section 2.6 for the entanglement swapping protocol the requirement for high interference contrast is an overlap of the photons in all degrees of freedom (except polarization) being as large as possible. This explicitly includes

- the spatial mode overlap
- the spectral overlap
- and the temporal overlap.

These requirements were fulfilled in the case where both photons originated from (identical) atomic sources in the entanglement swapping protocol. Achieving a sufficient overlap is obviously even more difficult if the photons stem from different sources. While the spatial mode overlap is guaranteed in the single-mode fiber beam splitter, the central frequencies and the temporal shapes of the photonic wave functions of both sources have to be matched. As will be shown, these requirements can be fulfilled by the laser source to a high degree.

3.2.2. Attenuation of the laser pulse

For the derivation of the quantum teleportation scheme, we neglected all terms in equation 3.1 where the laser pulse contains two or more photons. However, this simplification is not necessarily justified and errors due to the Poissonian photon statistics of the laser pulse have to be investigated. Since photons originating from the laser pulse are not correlated, a statistical analysis of the photon number is performed.

For most excitations the photon emitted by the atom will not be collected and therefore not reach the BSM apparatus. The laser pulse on the other hand can contain more than one photon. If two photons originating from the laser pulse are detected in a combination of detectors that corresponds to a Bell-state this will imitate a teleportation event. As the state of the atom in this case is fully independent of the polarization of the laser pulse, these events will contribute to the noise in the experiment (called “laser noise”). To minimize such noise we have to analyze the effect of the Poissonian photon statistics of the pulse on the fidelity of the teleported state to determine the attenuation necessary for an appropriate signal-to-noise ratio.

To calculate the probabilities for signal and noise events, the efficiency η_{A} to detect a photon emitted by the atom after one excitation and the efficiency η_{L} to detect at least one photon in the

attenuated laser pulse are measured separately. This is done by triggering either the excitation of the atom or switching on the laser pulse. Dividing the number of trials after which a photon was detected at the BSM by the total number of trials yields the efficiencies. For photons emerging from the atoms we obtain $\eta_{\mathrm{A}} = 1.054 \times 10^{-3} \pm 0.5 \times 10^{-5}$ limited mainly by the collection efficiency in the microscope and we can select any value for η_{L} by changing the attenuation of the laser. The laser efficiency η_{L} is related to the Poissonian probability distribution to detect k photons in a pulse with a mean photon number μ:

$$P_\mu(k) = \frac{\mu^k}{k!} e^{-\mu} \tag{3.6}$$

Note, that μ here refers to the mean photon number including the detection efficiency and is related to α (equation 3.1) by $\mu = |\alpha|^2 \cdot \eta_D$ (with detection efficiency η_D). The probability to detect at least one photon, which is equal to the measured efficiency η_{L}, is

$$\eta_{\mathrm{L}} = P_\mu(k \geq 1) = 1 - P_\mu(k = 0) = 1 - e^{-\mu} \approx \mu, \tag{3.7}$$

with the approximation being valid for high attenuations and therefore small mean photon numbers (of the order $0.1...1.0 \times 10^{-3}$). In this regime, in most cases no photon will be detected after triggering the laser pulse and the probabilities of detecting one and two photons are

$$P_\mu(k = 1) = \frac{\mu}{1!} e^{-\mu} \approx \mu, \tag{3.8}$$

$$P_\mu(k = 2) = \frac{\mu^2}{2!} e^{-\mu} \approx \frac{\mu^2}{2}. \tag{3.9}$$

The success probability P_{T} of a teleportation attempt (detection of one photon from the atom and one from the laser pulse) is given as

$$P_{\mathrm{T}} = \frac{1}{2} \eta_{\mathrm{A}} P_\mu(k = 1) \approx \frac{1}{2} \eta_{\mathrm{A}} \mu, \tag{3.10}$$

with a factor of $\frac{1}{2}$ accounting for the fact that only two out of four Bell-states can be detected. The probability P_{LN} for a two-photon coincidence by photons originating from the laser ("laser noise") is

$$P_{\mathrm{LN}} \approx f_{\mathrm{LN}} \cdot \frac{\mu^2}{2} + O(\mu^3), \tag{3.11}$$

where we neglect laser pulses with three or more photons. The factor f_{LN} is the probability to register the two photons in a detector combination corresponding to a Bell-state, thus signaling a teleportation event. This depends on the polarization of the laser pulse. A teleportation event is

heralded by either a $|\Psi^+\rangle$- or a $|\Psi^-\rangle$-Bell-state of the photonic measurement. In both cases one photon has to be detected with horizontal and the other with vertical polarization. The probability for this is $f_{\mathrm{LN}} = \frac{1}{2}$ if the laser is circularly or $\pm 45°$ polarized and $f_{\mathrm{LN}} = 0$ for H/V-polarization. The contribution of the laser noise therefore depends on the state to be teleported, however for an arbitrary state we will assume the worst case of $f_{\mathrm{LN}} = \frac{1}{2}$. The criterion to achieve a high fidelity of the teleported state is that the probability for signal events is much larger than the laser noise $P_{\mathrm{T}} \gg P_{\mathrm{LN}}$, and therefore $\eta_{\mathrm{A}} \gg \frac{\mu}{2}$. This is achieved by choosing a strong attenuation of the laser pulse which, however, also reduces the success probability of teleportation events and therefore the event rate.

Two-photon emission of the atoms

Similar to two photons from the laser pulse, two-photon emission events from the atom can cause erroneous coincidences at the BSM detectors. In previous work [43], the probability of multi-photon emissions of atoms within a single excitation pulse is investigated. Due to the length of the excitation pulse, a re-excitation after a first photon emission is possible, either resonantly to the $F' = 0$ level or off-resonantly to the $F' = 1$ level and a second photon is emitted. If both photons are $\sigma^{\pm}$-polarized, they can both be registered at the detectors of the BSM setup. Therefore, the first decay has to result in the final state $|m_F = \pm 1\rangle_z$ of the level $F = 1$. For the re-excitation and the second decay, we consider two possible scenarios (see figure 3.1):

- First, we consider resonant excitation to the level $F' = 0$ (type I). This is possible if the excitation pulse is not perfectly π-polarized. The second decay will then result with a probability of $\frac{2}{3}$ in the states $|m_F = \pm 1\rangle_z$ and a $\sigma^{\pm}$-polarized photon will be emitted.

- Second, we consider off-resonant excitation to the level $F' = 1$ (type II). The following decay (if the emitted photon is $\sigma^{\pm}$-polarized) can result in the final state $|m_F = 0\rangle_z$ of the level $F = 1$ (with probability $p_a = \frac{25}{32}$, case II,a) or in the level $F = 2$ (in the states $|m_F = 0\rangle_z$ (with probability $p_b = \frac{1}{32}$, case II,b) and $|m_F = \pm 2\rangle_z$ (with probability $p_c = \frac{6}{32}$, case II,c)).

The probability for these events for each excitation of the atom was determined previously in a very similar experiment to be $p_{\mathrm{tpe}} = 0.0077 \pm 0.0005$ [43] with relative probabilities of $p_{\mathrm{I}} = 0.19 \pm 0.09$ for type I and $p_{\mathrm{II}} = 0.81 \pm 0.09$ for type II. To obtain the probability that they cause an erroneous teleportation event we have to include the detection efficiency for each photon of $\frac{3}{2}\eta_{\mathrm{A}}$ (η_{A} is the detection efficiency including π-polarized photons, thus for $\sigma^{\pm}$-polarized photons it is larger by a factor of 1.5) and the probability f_{tp} that the photons are detected in a detector combination that corresponds to a Bell-state. While type I events result with equal probability in all detector combinations ($f_{\mathrm{tp\,I}} = \frac{1}{2}$), type II events yield unequal probabilities ($f_{\mathrm{tp\,II}} = p_b + \frac{1}{2}p_c$) [43]. The reason is that for decays to the state $|m_F = \pm 1\rangle_z$ we obtain entanglement between the two photons. Transformed into the photonic basis H/V the two emitted photons are in the state:

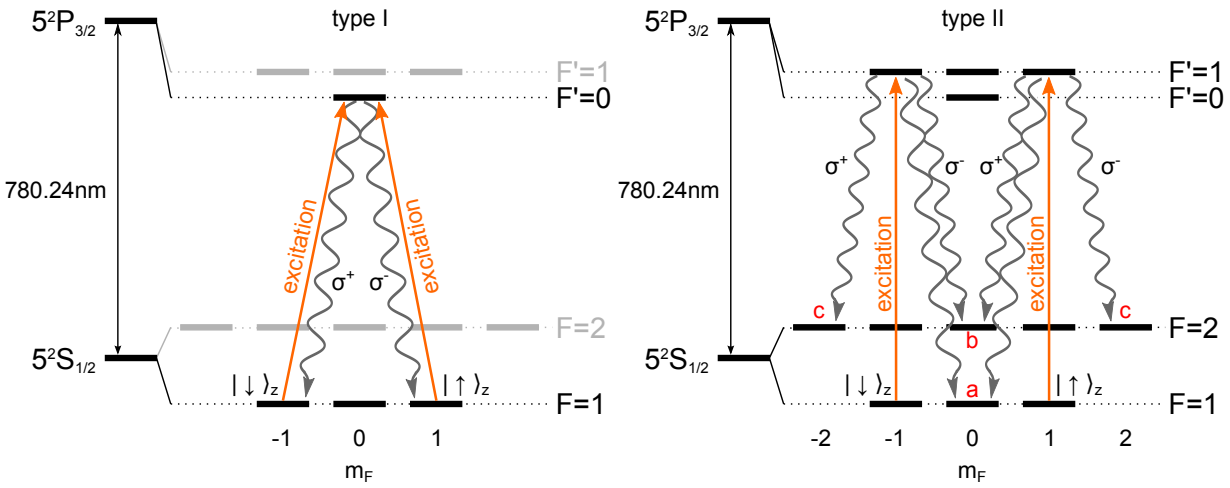

Figure 3.1.: Two-photon emission processes. After emission of a first $\sigma^{\pm}$-polarized photon the atom is in the states $|m_F = \pm 1\rangle_z$. Due to the length of the excitation pulse, a re-excitation and emission of a second photon is possible (Shown are decays where the emitted photon is $\sigma^{\pm}$-polarized). We distinguish between type I and type II events. For type II, the final atomic states are (a) $|m_F = 0\rangle_z$ of $F = 1$, (b) $|m_F = 0\rangle_z$ of $F = 2$, and (c) $|m_F = \pm 2\rangle_z$.

$$|\Psi\rangle_{\mathrm{II,a}} = \frac{1}{\sqrt{2}}\left(|RL\rangle + |LR\rangle\right) = \frac{1}{\sqrt{2}}\left(|HH\rangle + |VV\rangle\right), \tag{3.12}$$

$$|\Psi\rangle_{\mathrm{II,b}} = \frac{1}{\sqrt{2}}\left(|RL\rangle - |LR\rangle\right) = \frac{1}{\sqrt{2}}\left(|HV\rangle - |VH\rangle\right) \tag{3.13}$$

Therefore, photons originating from a type II,a process will never be detected in a detector combination corresponding to a Bell-state, whereas the detection of both photons originating from a type II,b process will always result in an erroneous coincidence. The probability P_{tp} for noise due to two-photon emission events is then given as

$$P_{\mathrm{tp}} = \frac{9}{4}\eta_{\mathrm{A}}^2 \left(f_{\mathrm{tp\,I}}\, p_{\mathrm{I}} + f_{\mathrm{tp\,II}}\, p_{\mathrm{II}}\right) p_{\mathrm{tpe}} = 3.78 \times 10^{-9} \pm 0.69 \times 10^{-9}. \tag{3.14}$$

This probability is, of course, independent of the mean photon number of the laser pulses. With increasing attenuation of the laser pulses, the event rate will decrease and noise due to two-photon emissions of the atom will become the significant contribution. Hence, an additional criterion for a high signal-to-noise ratio is $P_{\mathrm{T}} \gg P_{\mathrm{tp}}$ which limits the maximal attenuation.

Noise due to dark counts

As a third source of noise, we have to include dark counts of the APDs into this consideration. A two-photon coincidence triggered by one photon detection of the atom or the laser, together with

a dark count also contributes to the noise and reduces the teleportation fidelity. The probability $P_{\mathrm{DC,A}}$ for a coincidence of a dark count together with a photon of the atom, the probability $P_{\mathrm{DC,L}}$ for a coincidence of a dark count together with a photon of the laser pulse and the combined probability $P_{\mathrm{DC,A\vee L}}$ for such events can be calculated as

$$\begin{aligned} P_{\mathrm{DC,A}} &= \frac{1}{2}\eta_{\mathrm{A}} d\Delta T, \\ P_{\mathrm{DC,L}} &\approx \frac{1}{2}\mu d\Delta T, \\ P_{\mathrm{DC,A\vee L}} &\approx \frac{1}{2}\left(\eta_{\mathrm{A}} + \mu\right) d\Delta T, \end{aligned} \tag{3.15}$$

where $d = 44\,\mathrm{s}^{-1}$ is the rate of dark counts at any of the detectors and $\Delta T = 120\,\mathrm{ns}$ the length of the time window in which coincidence clicks are registered. To avoid the dark counts becoming a dominant contribution, there is thus another requirement arising, $P_{\mathrm{T}} \gg P_{\mathrm{DC,A\vee L}}$ which limits the maximal attenuation and therefore the minimal laser efficiency.

Final criterion

Summarizing all the criteria obtained above, we conclude with the final criterion

$$2.108 \times 10^{-3} \;=\; 2\eta_{\mathrm{A}} \;\gg \mu \gg\; \frac{\eta_{\mathrm{A}} d\Delta T}{\eta_{\mathrm{A}} - d\Delta T} + \frac{2P_{\mathrm{tp}}}{\eta_{\mathrm{A}}} \;=\; 1.25 \times 10^{-5} \tag{3.16}$$

for the attenuation of the laser beam input.

3.2.3. Achievable event rate

A last crucial aspect about the choice of attenuation is the achievable event rate that is an important benchmark for all quantum communication experiments. It is the product of the success probability of a teleportation attempt P_{T} and the repetition rate R_{T}. As long as an atom is present in the trap, R_{T} is determined by the length of optical pumping and cooling sequences necessary for the excitation of the atom. In the current experiment this rate is

$$R_{\mathrm{T}} \;=\; 50.9 \times 10^{3}\,\frac{\mathrm{attempts}}{s}. \tag{3.17}$$

Depending on the fluctuating loading rate of atoms into the trap it typically amounts to $R_{\mathrm{T,eff}} \approx 0.9 \cdot R_{\mathrm{T}}$. Altogether, the reachable event rate $P_{\mathrm{T}} \cdot R_{\mathrm{T,eff}}$ is rather low (less than 1 event per minute), due to the low success probability that depends linearly on μ. Hence, the choice of attenuation requires a trade-off between the achievable fidelity and the event rate.

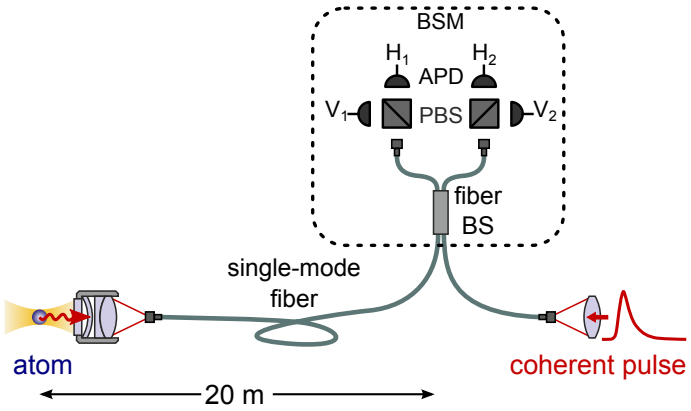

Figure 3.2.: Schematic of the quantum teleportation experiment consisting of an atom trap, the preparation of the attenuated laser pulse and the Bell-state measurement setup (BSM). The atom trap is located in a separate laboratory at a distance of $20\,\mathrm{m}$ from the BSM.

3.3. Setup and experimental procedure

The schematic of the experimental setup is shown in figure 3.2. The preparation of the coherent laser pulse and the Bell-state measurement are performed on the same optical table in one laboratory. The atom trap is located in a second laboratory at a distance of $20\,\mathrm{m}$ and is equipped with its independent control electronics. The overall setup is a modification of the previous one used to generate atom-atom entanglement [25] with the main difference, that one atom trap is replaced with the source of the coherent pulse. This highlights the similarity between the entanglement swapping and the quantum teleportation protocols. In the following, I will explain the components of the setup, their functioning and important characterization measurements.

3.3.1. Atom-photon entanglement

A crucial component of the teleportation protocol is an entangled atom-photon pair that is generated in the atom trap in the distant laboratory. The basics of the atom trap are already described in chapter 2. According to these methods, an atom is loaded into the optical dipole trap, atom-photon entanglement is generated and the emitted photon is coupled into a single-mode fiber and sent to the BSM setup. Once a BSM event occurred, indicated by a two-photon coincidence detection in a proper detector combination the atomic state is analyzed.

Atomic state analysis

The atomic states are analyzed by applying the ionization-based state measurement scheme (see section 2.5). All measurements in this chapter are evaluated with the fluorescence detection method without using the CEMs. A motorized half-wave plate (HWP) and quarter-wave plate

(QWP) are placed in the path of the readout beam which allow to measure the atomic state in all bases and a full state tomography of the qubit can be performed. The required measurements are projections of the atomic state onto the eigenstates of the three Pauli-operators $\hat{\sigma}_x$, $\hat{\sigma}_y$ and $\hat{\sigma}_z$. To convert the polarization of the readout beam to the measurement basis we follow the convention (relations between the different polarization states and the spin states are summarized in appendix C):

readout polarization	analyzed dark state	Pauli-operator	eigenvalue
$\|H\rangle$	$\|\uparrow\rangle_x$	$\hat{\sigma}_x$	$+1$
$\|V\rangle$	$\|\downarrow\rangle_x$	$\hat{\sigma}_x$	-1
$\|-45°\rangle$	$\|\uparrow\rangle_y$	$\hat{\sigma}_y$	$+1$
$\|+45°\rangle$	$\|\downarrow\rangle_y$	$\hat{\sigma}_y$	-1
$\|L\rangle$	$\|\uparrow\rangle_z$	$\hat{\sigma}_z$	$+1$
$\|R\rangle$	$\|\downarrow\rangle_z$	$\hat{\sigma}_z$	-1

Atom-photon correlations

Before starting the teleportation attempts, the quality of the prepared entangled atom-photon state and the atomic state analysis are evaluated. Therefore, correlations between the polarization of the emitted photon and the atomic state are measured. The photonic polarization is analyzed in the BSM setup, where the PBS and a combination of a half-wave plate and a quarter-wave plate in one of the outputs of the fiber BS (see figure 2.6) allow for selection of an arbitrary measurement basis. After the detection of a photon, the atomic state is measured in a certain measurement basis chosen by the polarization of the readout beam. To obtain the correlation curves shown in figure 3.3 the measurement basis of one particle is kept constant while the other one is rotated. The measurement bases are chosen in the following way:

- In a), the atomic measurement basis is rotated by 2π in the spin space and the states $|\uparrow\rangle_x$, $|\downarrow\rangle_x$, $|\uparrow\rangle_y$ and $|\downarrow\rangle_y$ are analyzed. The photons are analyzed in the basis H/V (red/blue data points).

- In b), the atomic measurement basis is rotated by 2π in the spin space and the states $|\uparrow\rangle_x$, $|\downarrow\rangle_x$, $|\uparrow\rangle_y$ and $|\downarrow\rangle_y$ are analyzed. The photons are analyzed in the basis $+/-$ (green/black data points).

- In c), the situation is different. The analyzed atomic state is $|\downarrow\rangle_z$ and the photonic measurement basis is changed with the integrated quarter-wave plate. Therefore, the curves (cyan, magenta) do not correspond to constant polarizations of the photons as in a) and b), but to the probability to prepare the atomic states $|\uparrow\rangle_z$ and $|\downarrow\rangle_z$ for the detection of a certain photon polarization.

The measurement result is the conditional probability to detect the atoms in the dark state if the photon was measured with a certain polarization. This corresponds to the population of the dark state up to the infidelity of the state readout. Each data point in figure 3.3 thus shows the

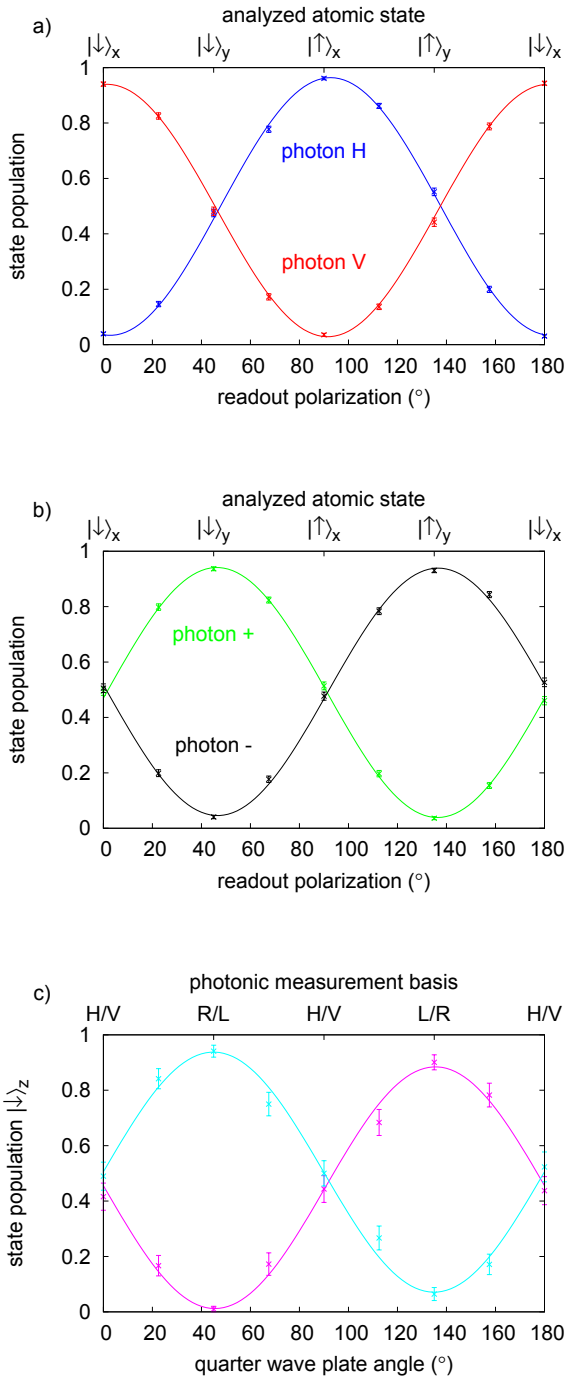

Figure 3.3.: Atom-photon correlations. In a) and b) the linear polarization of the readout laser is rotated, hence the atomic measurement basis is rotated by 2π in the spin space. The basis of the photons is H/V in a) and $+/-$ in b). In c) the atomic states are projected onto $|\downarrow\rangle_z$ and the photonic basis is rotated.

state population $p^{DS|pol}$ of the analyzed (dark) state DS for the detection of a certain photon polarization pol which is measured according to

$$p^{DS|pol} = \frac{N^{DS|pol}}{N^{pol}}. \tag{3.18}$$

Here, N^{pol} is the number of events where the photon was detected in the polarization state pol and $N^{DS|pol}$ is the subset of N^{pol} where the atom was found to be in the respective state DS. By fitting sinusoidal functions to the data, we obtain the peak-to-peak amplitude A (e.g. $A = p^{|\downarrow\rangle_x||V\rangle} - p^{|\uparrow\rangle_x||V\rangle}$ for the red curve in figure 3.3 a)). This amplitude is associated with the visibility $V = A$ of the measurement.

Visibility and fidelity of the entangled atom-photon state

The measurement allows us to estimate the fidelity of the entangled atom-photon state. We assume that the density matrix of the entangled state can be written as [67]

$$\hat{\rho} = V\ |\Psi_{\mathrm{AP}}\rangle\langle\Psi_{\mathrm{AP}}| + \frac{1}{4}(1-V)\ \hat{1}, \tag{3.19}$$

with the visibility V obtained from correlation curves, the maximally entangled atom-photon state $|\Psi_{\mathrm{AP}}\rangle$ and the matrix $\frac{1}{4}\hat{1}$ of the completely mixed state. Since the atomic state analysis is not perfectly symmetric (i.e. the probability to correctly detect atoms in the dark state is different from atoms in the bright state) and due to residual population of the third ground state $|m_F = 0\rangle_z$ this is just a simplified model for the actual atom-photon state. However, the deviation from this model is assumed to be low. The fidelity, which is the probability to find the atom-photon pair in the pure state $|\Psi_{\mathrm{AP}}\rangle$, is then given as

$$F = \langle\Psi_{\mathrm{AP}}|\,\hat{\rho}\,|\Psi_{\mathrm{AP}}\rangle = 0.25 + 0.75 \cdot V. \tag{3.20}$$

We assume that the visibilities in all measurement bases are identical and the peak-to-peak amplitudes can be averaged. The mean peak-to-peak amplitude of all sinusoidal fit functions is $A = 0.909 \pm 0.007$. The fidelity of the entangled atom-photon state corresponding to this visibility is then estimated as $F_{\mathrm{AP}} = 0.932$. The fidelity of the entangled atom-photon state will later be used to estimate a fidelity of the teleported states.

3.3.2. Preparation of the laser pulses

I will now introduce the techniques to generate laser pulses that fulfill the required high overlap with the atomic emission. The setup shown in figure 3.4 consists of a laser source, frequency stabilization and frequency setting, shaping of the pulse, polarization setting and attenuation.

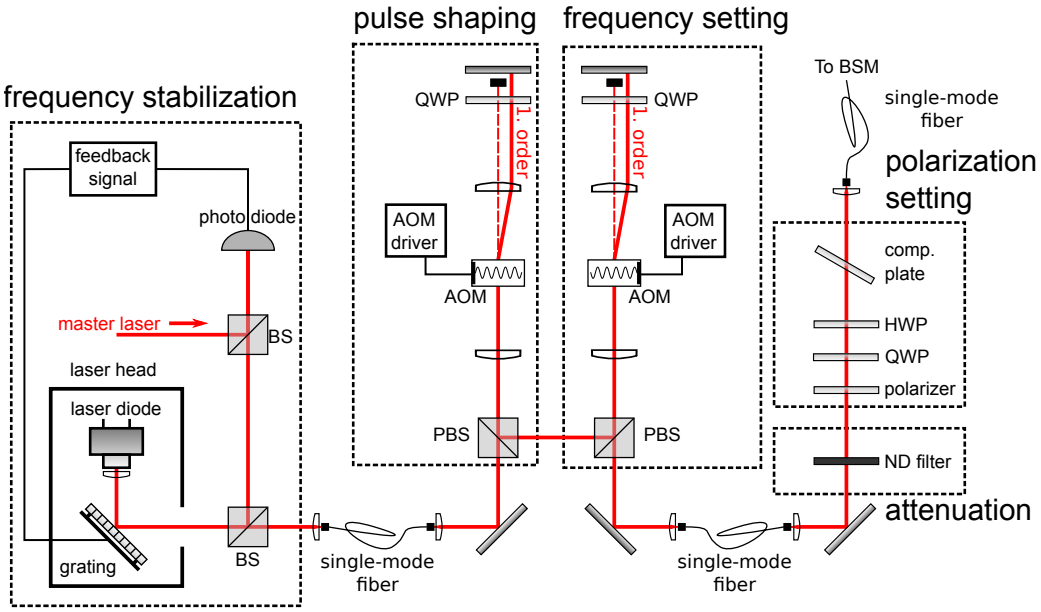

Figure 3.4.: Setup of the laser source. It consists of different parts that are used for frequency stabilization and frequency setting, shaping of the laser pulse, polarization setting, and attenuation.

Frequency setting and stabilization

As laser source we use a laser diode at a central wavelength of $785\,\mathrm{nm}$ with a typical output power of several $10\,\mathrm{mW}$. A diffraction grating in a Littrow configuration forms an extended cavity and tilting of the grating enables to select and shift the emitted wavelength [47]. To stabilize the wavelength over the course of the experiment we use a two step scheme. First, a second laser, the master laser, is stabilized to the transition $5^2S_{1/2},\ F = 1 \rightarrow 5^2P_{3/2},\ F' = 1$ of Rubidium using Doppler-free saturation spectroscopy. Then, the frequency of the primary laser is stabilized relative to this frequency ($-316\,\mathrm{MHz}$ to the transition) in a feedback loop of the beat signal between the two lasers and the piezo-driven diffraction grating [68].

To shift the frequency of the laser to the transition frequency of the levels $5^2S_{1/2},\ F = 1 \rightarrow 5^2P_{3/2},\ F' = 0$ of Rubidium we use acousto-optical modulators. There are two successive AOMs in the setup, one for setting the frequency and another one to shape the laser pulse temporally. While the pulse shaping AOM is set to a constant frequency of the acoustic wave of about $350\,\mathrm{MHz}$, the frequency of the other AOM can be varied around its central frequency of $200\,\mathrm{MHz}$ in order to change the light frequency. Note that both AOMs are operated in a double-pass configuration thus each frequency shift is doubled. Furthermore, the two AOMs shift the frequency in different directions giving together the desired frequency matching the transition.

The AOM frequency has to be calibrated to match the central frequency of the laser pulses to that of the photons emitted by the atoms. For that purpose, we perform measurements in which the laser pulse is used to excite the $5^2S_{1/2},\ F = 1 \rightarrow 5^2P_{3/2},\ F' = 0$ transition of a trapped

Rubidium atom (in the trap setup in lab 1). The probability to detect a fluorescence photon following an excitation is measured in dependence of the AOM frequency. This probability is maximal at resonance and can be fitted by a Lorentzian to determine the actual position of the maximum (figure 3.5 a)). The AOM frequency is then set to this value.

Repeated measurements showed that the stability of the laser frequency is mainly limited by the stabilization of the master laser. However, possible drifts were found to be smaller than $300\,\mathrm{kHz}$. We use this number to estimate the possible reduction of the overlap of the wave functions of the interfering photons due to frequency mismatch. For simplicity, we assume that the temporal wave function is described by an exponential decay

$$\Psi(t) \;=\; \frac{1}{\sqrt{\tau}} \exp\left(-\frac{t}{2\tau}\right) \exp\left(-i\omega_0 t\right), \tag{3.21}$$

(for $t \geq 0$) with the lifetime $\tau = 26.2\,\mathrm{ns}$ (as a model for the atomic emission). The overlap for identical wave functions that differ only in the central frequency $\Delta\omega = \omega_0 - \omega_0'$ is then [62]:

$$\int dt\, \Psi_1^*(t)\Psi_2(t) \;=\; \frac{1}{1+\tau^2\Delta\omega^2} \tag{3.22}$$

Thus, in the worst case, the overlap reduced due to frequency mismatch is still 0.9976 (for $\Delta\omega = 300\,\mathrm{kHz}$).

Shaping of the laser pulse

The temporal overlap is maximized by shaping the laser pulse to have the same temporal distribution as the photon emitted by the atom. This distribution is determined by measuring arrival times of photons emitted by the atom at the APDs in the BSM setup. The detection times relative to the excitation are registered yielding the arrival time histogram shown in figure 3.5 b) (red line). The rising edge of the resulting shape is mainly depending on the shape and intensity of the excitation laser pulse while the falling edge depends on the life time of the excited state.

To obtain the same shape for the laser pulses, the beam is modulated by an AOM (AA Opto-Electronic AA.MT350). The envelope of the RF-signal applied to the AOM is set by an arbitrary waveform generator (LeCroy ArbStudio 1104D) at a sampling frequency of $250\,\mathrm{MHz}$. As the amplitude response of the AOM to the RF-amplitude is highly nonlinear, finding the right parameters is a non-trivial task. To find the optimal envelope defined by a set of interpolation points $\vec{p}$ of the arbitrary waveform generator we use an automatized method that is explained in detail in [69]. A simplified scheme of this procedure is shown in figure 3.6. The modulated laser pulse is registered by a fast photo diode (Thorlabs PDA10A) and its temporal shape is displayed on an oscilloscope. The pulse shape is read into a computer where the overlap

$$S \;=\; \sum_{i=1}^{n} \sqrt{r(t_i)m(t_i)} \tag{3.23}$$

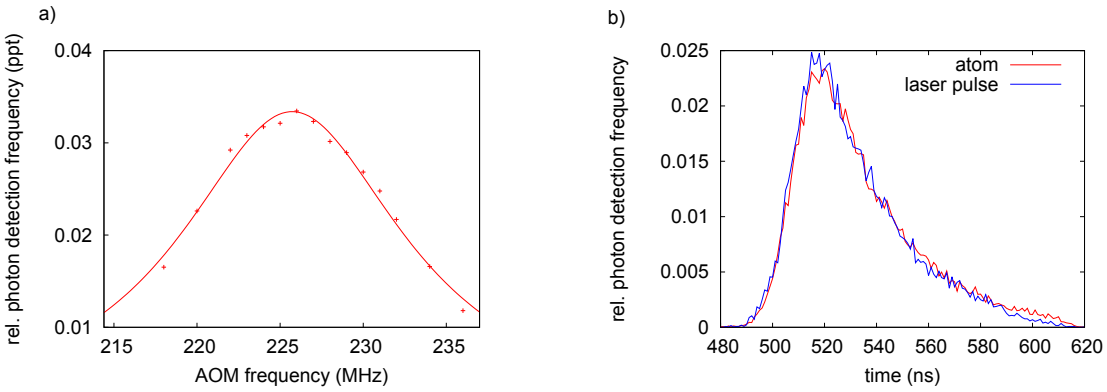

Figure 3.5.: a) Adjustment of the central frequency of the laser pulse to the frequency of the atomic transition $5^2S_{1/2},\ F = 1 \rightarrow 5^2P_{3/2},\ F' = 0$. The laser frequency is varied with an AOM and the relative photon detection frequency at the APDs is measured. The data is fitted by a Lorentzian to determine the maximum. b) Measured arrival time histograms of photons originating from the atom (red) and laser pulse (blue) at the APDs. The calculated overlap is 0.994.

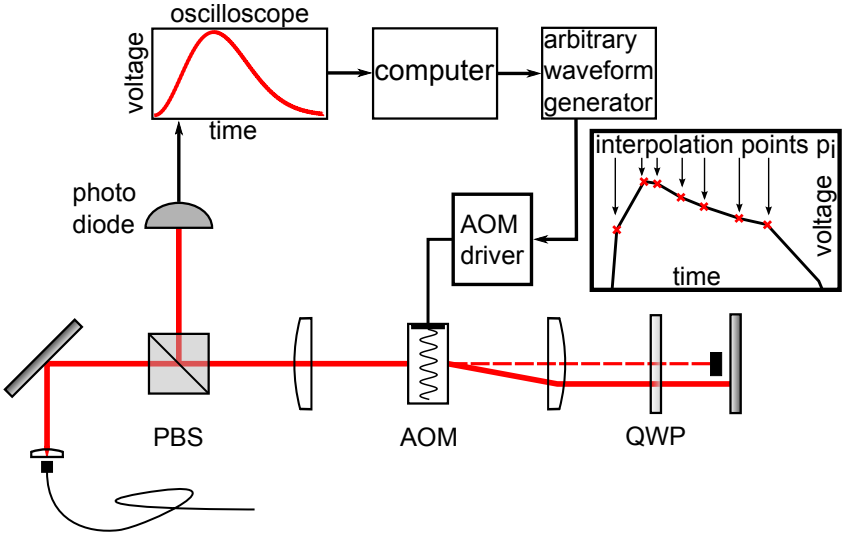

Figure 3.6.: Setup to match the temporal shape of the laser pulses to that of the atomic emission. The pulse is shaped by an AOM with input voltages set by an arbitrary waveform generator (AWG) and measured with a fast photo diode. A computer calculates the error function which is the deviation from the desired shape. By varying all parameters of the AWG the calculation of the gradient of the error function can be performed and the parameters of the AWG are optimized in the direction of negative gradient which reduces the error function. This scheme is repeated until the overlap of photons of the laser pulse and photons of the atom is maximized.

of this pulse with the reference shape of the atomic emission is calculated. Here, $r(t_i)$ are the normalized entries of the reference histogram and $m(t_i)$ are the normalized voltages measured at the photo diode (corresponding to the intensity of the laser pulse). The square root of these entries is associated with the (temporal) wave function of photons. The overlap is then maximized using a gradient-descent method. For the current set of interpolation points the error function

$$F(\vec{p}) \quad = \quad \sum_{i=1}^{n} \left(m(t_i) - r(t_i)\right)^2 \tag{3.24}$$

is calculated and the gradient $\nabla F(\vec{p})$ is evaluated by varying the parameters $\vec{p}$. The error function is then minimized in an iterative way by finding new parameters that are changed in the direction of negative gradient

$$\vec{p}^{(i+1)} \quad = \quad \vec{p}^{(i)} - \alpha \nabla F(\vec{p}^{(i)}), \tag{3.25}$$

with a factor α optimized to reduce the number of required repetitions. After several iterations the overlap of the histograms is maximized. The number of used interpolation points is 7 which already allows us to obtain pulse shapes that match well to the reference. The resulting laser pulse is then strongly attenuated (optical density 11) and measured in the few photon regime using the APDs in the BSM. After adjustment of the delay of the pulse the photon arrival time histograms of both sources, shown in figure 3.5 b), reach an overlap of $S = 0.994$. Together with the matched central frequency the two wave packets have an overlap close to unity thus the reduction in the teleportation fidelity is negligible.

Polarization setting and attenuation

The polarization of the laser pulse is set by a combination of a polarizer to define a stable polarization and a quarter-wave plate (QWP) and a half-wave plate (HWP) to set the desired polarization (see figure 3.4). Additionally, a compensation plate (comp.) compensates changes of the polarization caused by optical components. The attenuation of the laser pulse is achieved by a neutral density (ND) filter with an optical density of $OD = 11$. To fine-tune the laser efficiency η_{L} (or the mean photon number μ) the AOM that also fine-tunes the frequency of the laser pulses can be used. The laser efficiency can fluctuate over the course of an experiment. Thus, it has to be checked daily to ensure stable parameters of the laser pulse.

3.3.3. Connection and communication links

For performing the teleportation experiment, the atom trap and the laser source have to be connected with the BSM setup and communication has to be established between the two laboratories. Photons emitted by the atom and photons of the laser pulse are coupled into single-mode optical fibers leading to the BSM setup. To avoid changes of the polarization of photons in the fiber we compensate the birefringence of the glass fiber with polarization controllers on both

input state $\|\Psi\rangle_{\mathrm{I}}$	β	γ	BSM result $\|\Psi^-\rangle$	BSM result $\|\Psi^+\rangle$
			atom state $\|\Phi_1\rangle$	atom state $\|\Phi_2\rangle$
$\|H\rangle = \frac{1}{\sqrt{2}}(\|L\rangle + \|R\rangle)$	$\frac{1}{\sqrt{2}}$	$\frac{1}{\sqrt{2}}$	$\frac{1}{\sqrt{2}}\|\uparrow\rangle_z - \frac{1}{\sqrt{2}}\|\downarrow\rangle_z$	$\frac{1}{\sqrt{2}}\|\uparrow\rangle_z - \frac{1}{\sqrt{2}}\|\downarrow\rangle_z$
$\|+\rangle = \frac{1}{\sqrt{2}}(\|L\rangle - i\|R\rangle)$	$\frac{1}{\sqrt{2}}$	$\frac{-i}{\sqrt{2}}$	$\frac{1}{\sqrt{2}}\|\uparrow\rangle_z + \frac{i}{\sqrt{2}}\|\downarrow\rangle_z$	$\frac{-i}{\sqrt{2}}\|\uparrow\rangle_z - \frac{1}{\sqrt{2}}\|\downarrow\rangle_z$
$\|R\rangle$	0	1	$-\|\downarrow\rangle_z$	$\|\uparrow\rangle_z$

Table 3.1.: Expected atomic states $|\Phi_{1,2}\rangle$ for the teleportation of a given input state $|\Psi\rangle_{\mathrm{I}}$ of the laser pulses. The coefficients β and γ are defined in equation 3.3.

inputs and one output of the fiber beam splitter. Especially the $\sim 30\,\mathrm{m}$ long fiber from the atom trap to the BSM setup is sensitive to drifts of the birefringence and is stabilized automatically every 5 minutes during the experiment. The two sides are synchronized by different signals which are distributed over coaxial electric cables. This includes a common $100\,\mathrm{MHz}$ clock for the local control units and start signals that initiate certain experimental steps.

3.4. Experimental quantum teleportation

After fulfilling all requirements, we applied the described scheme to transfer polarization states of laser pulses onto the atom. To prove that the scheme works for an arbitrary input state, we used the polarization states $|H\rangle$,$|+\rangle$ and $|R\rangle$ as input states.

3.4.1. Fidelity estimation

Before I will go on with the experimental results I will focus on the estimation of the achievable fidelity of the generated atomic state. The expected atomic states $|\Phi_{1,2}\rangle$ according to equation 3.3 for the different input states are shown in table 3.1. Both the $|+\rangle$ and $|R\rangle$ input states transform to different teleported states depending on the detected Bell coincidence whereas for an input state $|H\rangle$ these states do not differ.

Fidelity of the atomic state

For estimating the expected fidelity of the teleported state, we first consider the input states $|+\rangle$ and $|R\rangle$. Although we assume an overlap integral of the wave functions close to unity and therefore a high interference contrast, the fidelity of the teleported state is still limited by erroneous two-photon coincidences caused by the laser pulse (laser noise) and the atom. To estimate the reachable fidelity we also include noise due to dark counts and get

$$F = \frac{P_{\mathrm{T}}F_{\mathrm{AP}} + P_{\mathrm{LN}}F_{\mathrm{LN}} + P_{\mathrm{tp}}F_{\mathrm{tp}} + P_{\mathrm{DC,A\vee L}}F_{\mathrm{DC,A\vee L}}}{P_{\mathrm{T}} + P_{\mathrm{LN}} + P_{\mathrm{tp}} + P_{\mathrm{DC,A\vee L}}}, \tag{3.26}$$

with the fidelity of the entangled atom-photon state F_{AP}, the fidelities for the noise events F_{LN}, F_{tp}, $F_{\mathrm{DC,A\vee L}}$, and the probabilities P_{T}, P_{LN}, P_{tp}, and $P_{\mathrm{DC,A\vee L}}$ calculated in section 3.2.2.

The fidelities for events caused by noise are obtained from the probabilities to find the system in the correct state by chance after a detection of such coincidences. For a spin $\frac{1}{2}$ system with a binary measurement result this probability is 0.5. However, in our case the situation is different because we use state measurements with binary results on a quantum system that has spin 1. When no photon is detected after an excitation, the atom is with equal probability in one of the three ground states (if we assume perfect pumping and excitation beforehand). Therefore, the fidelity for those final states is $\frac{1}{3}$ and applies for laser noise and for dark count noise when a dark count together with a photon of the laser is detected. When a dark count together with a photon of the atom is detected, however, the atomic decay to the states $|m_F = \pm 1\rangle_z$ has occurred and the probability to obtain the desired state is $\frac{1}{2}$. Therefore, we can compose the probability to find the atom in the desired state by chance in the case of noise events due to dark counts with the two contributions weighted with the efficiencies η_L and η_A: $F_{\mathrm{DC,A\vee L}} = \frac{1}{\eta_\mathrm{L}+\eta_\mathrm{A}} (\frac{1}{3}\eta_\mathrm{L} + \frac{1}{2}\eta_\mathrm{A})$. In the case of two photon emission events of the atom, we have to distinguish between type I and type II (see figure 3.1). For type I, the probability to find the atom in the correct state by chance is $\frac{1}{2}$, whereas for type II, the atom is not in the qubit subspace and the probability to obtain the correct atomic state is 0. Both types combined result in a fidelity of $F_\mathrm{tp} = \frac{1}{2}p_\mathrm{I}$ (see section 3.2.2).

The teleportation of a horizontally polarized laser pulse is quite different to the other states because the BSM is performed in the H/V-basis. This means that every two-photon coincidence in a Bell channel (either $|\Psi^+\rangle$ or $|\Psi^-\rangle$) directly projects the polarization of the photon emitted by the atom onto the vertical polarization. Therefore, this process doesn't depend on the quality of two-photon interference and there are also no erroneous events due to two photon detection from laser pulses as pointed out in section 3.2.2. Thus, the teleportation of the horizontal polarization state becomes equal to the observation of atom-photon entanglement and for his case the fidelity is expected to be equal to the respective fidelity $F_\mathrm{AP} = 0.932$ (see section 3.3.1). The only contributions that reduce the fidelity in this case are two-photon emission events of the atom and noise due to dark counts.

Population of the qubit subspace after teleportation

Since the ground state of Rb is effectively a spin 1 system, the noise events result with a certain probability in a final atomic state that is not in the qubit subspace, but in the state $|m_F = 0\rangle_z$ (or in the level $F = 2$). The probability $P^{(0)}$ that the atom is not in the qubit subspace can be estimated from the probabilities of erroneous events. Such events are (see section 3.3.1)

- two-photon coincidences where both detected photons originate from the laser pulse. The atom is then with a probability $\frac{1}{3}$ (assuming ideal pumping and excitation) in the state $|m_F = 0\rangle_z$. The probability thus is given as $P^{(0)}_\mathrm{LN} = \frac{1}{3}\,\frac{P_\mathrm{LN}}{P_\mathrm{T}+P_\mathrm{LN}+P_\mathrm{tp}+P_\mathrm{DC,A\vee L}}$.
- two-photon coincidences where both detected photons originate from the atom and are emitted in a type II process (see figure 3.1). The probability is $P^{(0)}_\mathrm{tp} = \frac{p_\mathrm{II}\,P_\mathrm{tp}}{P_\mathrm{T}+P_\mathrm{LN}+P_\mathrm{tp}+P_\mathrm{DC,A\vee L}}$.
- coincidences of an APD dark count and a detection of a photon originating from the laser pulse with $P^{(0)}_\mathrm{DC,L} = \frac{1}{3}\,\frac{P_\mathrm{DC,L}}{P_\mathrm{T}+P_\mathrm{LN}+P_\mathrm{tp}+P_\mathrm{DC,A\vee L}}$.

$\|\Psi\rangle_{\mathrm{I}}$	η_{L}	F	$P^{(0)}$
$\|H\rangle$	$1.156 \times 10^{-3} \pm 2.1 \times 10^{-5}$	0.922 ± 0.007	0.005
$\|+\rangle$	$0.217 \times 10^{-3} \pm 0.9 \times 10^{-5}$	0.844 ± 0.007	0.046
$\|R\rangle$	$0.235 \times 10^{-3} \pm 0.8 \times 10^{-5}$	0.842 ± 0.007	0.048

Table 3.2.: Laser efficiencies, expected fidelities, and probability $P^{(0)}$ that the atomic state is not in the qubit subspace for the three experimental runs.

The overall probability that the atom is not in the qubit subspace is thus given as $P^{(0)} = P^{(0)}_{\mathrm{tp}} + P^{(0)}_{\mathrm{LN}} + P^{(0)}_{\mathrm{DC,L}}$ (for the input states $|+\rangle$ and $|R\rangle$) and $P^{(0)} = P^{(0)}_{\mathrm{tp}} + P^{(0)}_{\mathrm{DC,L}}$ (for the input state $|H\rangle$).

Selected parameters and expected fidelities

Using these considerations, we choose specific attenuations and, thereby, efficiencies η_{L} for the laser pulse. To increase the event rate and to reduce the overall time of the run for the state $|H\rangle$, the laser efficiency is chosen to be comparable to $\eta_{\mathrm{A}} = 1.054 \times 10^{-3} \pm 0.5 \times 10^{-5}$. For the states $|+\rangle$ and $|R\rangle$ on the other hand where a lower efficiency is required, it is set to $\eta_{\mathrm{L}} \approx \frac{1}{5}\eta_{\mathrm{A}}$. The measured laser efficiencies, the theoretically reachable fidelities of the teleported state F, and the probability that the atomic state will be outside the qubit subspace $P^{(0)}$ are summarized in table 3.2.

3.4.2. Results and analysis

We have performed an experimental run for each of the three input polarization states. The success of the teleportation is proven by measuring the density matrix of the atomic qubit [70] for both possible outcomes of the BSM, $|\Psi^+\rangle$ and $|\Psi^-\rangle$. Due to the population of the state $|m_F = 0\rangle_z$ the spin 1 system has to be described by a 3×3 density matrix. However, the state analysis scheme (see section 2.5) only allows to project atoms onto a dark state in the $\{|\uparrow\rangle_z, |\downarrow\rangle_z\}$ subspace. Therefore, it is not possible to determine a full density matrix. Yet, a partial reconstruction of the qubit subspace and an estimation of missing entries is possible. By assuming that the population transfer to the state $|m_F = 0\rangle_z$ is completely incoherent, the density matrix (in the basis ($|\uparrow\rangle_z$, $|\downarrow\rangle_z$, $|m_F = 0\rangle_z$)) is given as [41]

$$\hat{\rho} = \begin{pmatrix} & \hat{\rho}_s & & 0 \\ & & & 0 \\ 0 & 0 & & \rho_{00} \end{pmatrix}, \tag{3.27}$$

with the matrix of the qubit subspace $\hat{\rho}_s$ and the population $\rho_{00} = 1 - \mathrm{tr}(\hat{\rho}_s)$ of the state with $m_F = 0$.

To measure $\hat{\rho}_s$, the atomic state is projected onto the eigenstates of the Pauli matrices $\hat{\sigma}_x$, $\hat{\sigma}_y$ and $\hat{\sigma}_z$ which are the spin states $|\uparrow\rangle_x$, $|\downarrow\rangle_x$, $|\uparrow\rangle_y$, $|\downarrow\rangle_y$, $|\uparrow\rangle_z$ and $|\downarrow\rangle_z$ (6 independently measured settings). In principle, one measurement per basis $|\uparrow\rangle_i$ / $|\downarrow\rangle_i$ ($i \in \{x, y, z\}$) should be sufficient

for a qubit. But since our quantum system has spin 1 and the detection of an atom in the bright state can always include the state $|m_F = 0\rangle_z$ or the level $F = 2$, we only use the probabilities of the atom being in the dark state for the evaluation of $\hat{\rho}_s$, as these are well defined. The density matrix $\hat{\rho}_s$ is then evaluated according to [41]

$$\hat{\rho}_s = \left(\frac{1}{2}\langle\hat{\sigma}_x\rangle\hat{\sigma}_x + \frac{1}{2}\langle\hat{\sigma}_y\rangle\hat{\sigma}_y + p^{\uparrow_z}\,|\uparrow_z\rangle\,\langle\uparrow_z| + p^{\downarrow_z}\,|\downarrow_z\rangle\,\langle\downarrow_z|\right), \tag{3.28}$$

$$p^{DS} = \frac{N^{DS}}{N^{DS}_{tot}}, \tag{3.29}$$

$$\langle\hat{\sigma}_i\rangle = \frac{N^{\uparrow_i}}{N^{\uparrow_i}_{tot}} - \frac{N^{\downarrow_i}}{N^{\downarrow_i}_{tot}}, \tag{3.30}$$

with the probability p^{DS} ($DS \in \{\uparrow_z, \downarrow_z\}$) to find the atom in the state $|\uparrow\rangle_z$ ($|\downarrow\rangle_z$) and $N^{\uparrow_i}$ ($N^{\downarrow_i}$) being the number of events with the corresponding dark state $|\uparrow\rangle_i$ ($|\downarrow\rangle_i$) as the outcome in a total number of $N^{\uparrow_i}_{tot}$ ($N^{\downarrow_i}_{tot}$) measurements. Note, that the resulting density matrix is not necessarily physical due to measurement statistics. The expected error of each entry of the density matrix is calculated according to the Bernoulli distribution suitable for the binary measurement outcomes of each event. The relative error of the measurement result of events where the atom was found in the dark state is

$$\triangle\frac{N^{DS}}{N^{DS}_{tot}} = \sqrt{\frac{N^{DS}(N^{DS}_{tot} - N^{DS})}{(N^{DS}_{tot})^3}}, \tag{3.31}$$

with $DS \in \{\uparrow_i, \downarrow_i\}$ and the error $\triangle\langle\hat{\sigma}_i\rangle$ of each measurement basis is then calculated under the assumption that the statistical fluctuations of the measurements in different bases are independent:

$$\triangle\langle\hat{\sigma}_i\rangle = \sqrt{\frac{N^{\uparrow_i}(N^{\uparrow_i}_{tot} - N^{\uparrow_i})}{\left(N^{\uparrow_i}_{tot}\right)^3} + \frac{N^{\downarrow_i}(N^{\downarrow_i}_{tot} - N^{\downarrow_i})}{\left(N^{\downarrow_i}_{tot}\right)^3}} \tag{3.32}$$

To compare the measurement results with the expected states $|\Phi_{1,2}\rangle$ we can calculate the fidelity F of the teleported state separately for the two cases of obtaining either the state $|\Psi^-\rangle$ (expected state $|\Phi_1\rangle$) or the state $|\Psi^+\rangle$ (expected state $|\Phi_2\rangle$), respectively (see table 3.1) as

$$F = \langle\Phi_{1,2}|\hat{\rho}_s|\Phi_{1,2}\rangle \tag{3.33}$$

and compare it with the fidelities estimated for the chosen experimental parameters (see table 3.2).

$45°$-polarized input pulse

In the first run we prepared the input polarization state $|\Psi\rangle_{\mathrm{I}} = |+\rangle$. Over the course of $77\,\mathrm{h}$ a total of 1296 events have been registered with 658 coincidences in a $|\Psi^-\rangle$ BSM detector combination and 638 coincidences corresponding to the state $|\Psi^+\rangle$. The evaluated density matrices are

$$\hat{\rho}_s^- = \begin{pmatrix} 0.554\,(\pm 0.049) & -0.091\,(\pm 0.033) - 0.311\,(\pm 0.026)\,i \\ -0.091\,(\pm 0.033) + 0.311\,(\pm 0.026) i & 0.500\,(\pm 0.049) \end{pmatrix}$$
$$\hat{\rho}_s^+ = \begin{pmatrix} 0.372\,(\pm 0.050) & 0.071\,(\pm 0.032) + 0.365\,(\pm 0.024)\,i \\ 0.071\,(\pm 0.032) - 0.365\,(\pm 0.024)\,i & 0.490\,(\pm 0.050) \end{pmatrix}$$

illustrated also as bar charts in figure 3.7. The corresponding fidelities of the teleported states are $F^- = 0.839 \pm 0.039$ and $F^+ = 0.796 \pm 0.039$.

Circularly polarized input pulse

Next, the polarization state $|\Psi\rangle_{\mathrm{I}} = |R\rangle$ was teleported. Within $59\,\mathrm{h}$, 981 events have been measured thereof 501 events corresponding to a $|\Psi^-\rangle$ Bell-state of the photons and 480 events corresponding to the state $|\Psi^+\rangle$. The density matrices for this experimental run are

$$\hat{\rho}_s^- = \begin{pmatrix} 0.145\,(\pm 0.042) & 0.077\,(\pm 0.036) - 0.071\,(\pm 0.037)\,i \\ 0.077\,(\pm 0.036) + 0.071\,(\pm 0.037)\,i & 0.760\,(\pm 0.049) \end{pmatrix}$$
$$\hat{\rho}_s^+ = \begin{pmatrix} 0.772\,(\pm 0.047) & -0.073\,(\pm 0.037) + 0.011\,(\pm 0.041)\,i \\ -0.073\,(\pm 0.037) - 0.011\,(\pm 0.041)\,i & 0.132\,(\pm 0.039) \end{pmatrix}$$

and are again plotted in figure 3.7. The corresponding fidelities of the teleported states are $F^- = 0.760 \pm 0.049$ and $F^+ = 0.772 \pm 0.042$, respectively.

Horizontally polarized input pulse

In the final measurement, the pulse was prepared with the polarization state $|\Psi\rangle_{\mathrm{I}} = |H\rangle$. In this run the overall time was $40\,\mathrm{h}$ where a total of 2678 events could be registered because of the increased efficiency of the laser pulse η_{L}. The events divide into the two heralded states with 1288 events for the $|\Psi^-\rangle$ coincidence and 1390 events for the $|\Psi^+\rangle$ coincidence. The obtained density matrices for this third case are

$$\hat{\rho}_s^- = \begin{pmatrix} 0.463\,(\pm 0.035) & -0.441\,(\pm 0.011) + 0.143\,(\pm 0.023)\,i \\ -0.441\,(\pm 0.011) - 0.143\,(\pm 0.023)\,i & 0.531\,(\pm 0.035) \end{pmatrix}$$
$$\hat{\rho}_s^+ = \begin{pmatrix} 0.491\,(\pm 0.034) & -0.419\,(\pm 0.013) + 0.041\,(\pm 0.023)\,i \\ -0.419\,(\pm 0.013) - 0.041\,(\pm 0.023)\,i & 0.521\,(\pm 0.031) \end{pmatrix}$$

also shown in figure 3.7. The corresponding fidelities of the teleported states are $F^- = 0.938 \pm 0.026$ and $F^+ = 0.925 \pm 0.025$.

teleportation results for the state $|+\rangle$

teleportation results for the state $|R\rangle$

teleportation results for the state $|H\rangle$

Figure 3.7.: Measured density matrices $\hat{\rho}_s$ for the teleported polarization states $|+\rangle$, $|R\rangle$ and $|H\rangle$, separately evaluated for the detection of a $|\Psi^-\rangle$- and a $|\Psi^+\rangle$ detection at the BSM. The obtained matrices match to the prediction of the quantum teleportation scheme with fidelities close to a theoretical model.

Analysis of the results

The measured atomic states and the observed fidelities match well with the ones predicted by the quantum teleportation scheme. The teleportation of the state $|H\rangle$ reaches, as previously explained, the highest fidelity limited mainly by the fidelity of the original entangled atom-photon state and is in good agreement with this value. The measured fidelities for the states $|+\rangle$ and $|R\rangle$ are slightly smaller than predicted by the theoretical model. There are a few reasons that can explain the further reduction of the fidelity. Foremost, it can be instabilities in the setup (e.g. of the efficiency of the laser pulse, the power of the readout beam, or magnetic fields (see chapter 5)) over the relatively long times of the experimental run. In addition to these experimental issues, there is one last, more fundamental effect of two-photon emission from the atom to take into account. As described in previous work [43], there is a third type (III), where the atom decays back into the state $|m_F = 0\rangle_z$ by emitting a π-polarized photon which cannot be detected. If the atom then is re-excited, the second photon can be detected at the BSM detectors and provide a teleportation event. However, the overlap of this photon with photons of the laser pulse is reduced due to the timing information in principle obtainable from the first emission. For the very similar parameters of [43] decoherence occurs according to a reduced overlap of $O^2 = 0.79$. Yet, the probability for such events is only $p_O = 0.033 \pm 0.003$. Thus, the fidelity of the teleported states $|+\rangle$ and $|R\rangle$ is reduced due to these processes by about $p_O \cdot (1 - (O^2 + 0.5 \cdot (1 - O^2))) = 0.003$ (even if the photons do not interfere the atom will be with a probability of 0.5 in the correct state). The resulting reduction is however very small and this effect can be neglected.

Improving the fidelity of the teleported state

The population of the state $|m_F = 0\rangle_z$ (and the level $F = 2$) of up to $P^{(0)} \approx 5\%$ after the teleportation is a main contribution to the reduction of the fidelity. It can however be avoided if a suitable way to remove atoms in this state is found. This approach requires a state selective excitation of the state $|m_F = 0\rangle_z$ that does not affect the qubit subspace. Then, using an ionization scheme for the excited atoms, an analysis of the ionization fragments by channel-electron-multipliers (CEMs) provides a fast method to decide if the atom is in the qubit subspace. If the CEMs detect the ionization of the atom, the event can be discarded. Otherwise, the teleported state can be used for further applications. This method would on the one hand increase the fidelity of the teleported state by $P^{(0)}$, but on the other hand also reduce the event rate.

In our setup the excitation laser (see e.g. appendix B) could be used for exciting atoms in the state $|m_F = 0\rangle_z$ to the level $5^2P_{3/2}$, $F' = 0$. However, the selectivity of this transition still is limited by off-resonant excitation of the qubit states to the level $5^2P_{3/2}$, $F' = 1$ that is separated by only $72.2\,\mathrm{MHz}$ to the resonant transition. Thus, a scheme providing a better selectivity would be desirable for this approach.

3.5. Summary

In summary, this chapter presented quantum teleportation employing a laser source for the preparation of the input states. The polarization states of a laser pulse were transferred onto an atom

at a distance of $20\,\mathrm{m}$. For that purpose, the laser pulse had to be matched to photons emitted by the atom which, in particular, included the temporal shape and the central frequency of the laser pulse. To achieve high fidelities of the teleported state, the laser pulse had to be attenuated to avoid erroneous events caused by two-photon coincidences where both detected photons originate from the laser pulse. An analysis to estimate the required attenuation was presented, based on probabilities for signal and noise events of the teleportation scheme. To verify the teleportation protocol we teleported three input states ($|H\rangle$, $|+\rangle$, and $|R\rangle$) of the laser pulse onto the atom and measured for each of them the resulting density matrix of the atomic state. The fidelities of the teleported states reached values of $F \geq 0.76$ for each state, consistent with a detailed noise model.

4. Towards long-distance atom-atom entanglement

In the following chapters, I will discuss the generation of entanglement between two Rubidium atoms over a long distance. In reference [25, 43], we achieved atom-atom entanglement over a distance of $20\,\mathrm{m}$. This distance was, in 2012, the record distance for quantum communication with matter particles. However, it is still too short to achieve one of the main aims of this project, which is a violation of Bell's inequality with both the detection and the locality loophole closed. While the detection loophole was closed by employing the event-ready scheme in the atom-atom entanglement experiment over $20\,\mathrm{m}$, described in chapter 2.6, the locality loophole was still open. A violation of Bell's inequality that makes no assumptions on the possible communication between the two sides has the crucial requirement of space-like separated measurements on the particles. That means that the distance between the two traps has to be large and the state measurements have to be fast enough to ensure that a signal propagating at the speed of light can not reach the other side within the measurement time. Therefore, the distance between the atom traps was further increased in order to actually fulfill this requirement. While entanglement swapping itself is scalable, there are stronger requirements for larger distances. This includes the lower achievable event rate, the more complicated synchronization of the trap setups and the required coherence times of atomic states. This chapter describes the experimental sequence and the implemented modifications and optimizations needed to successfully entangle two atoms over a larger distance.

4.1. Location and control of the experiment

4.1.1. Map of the trap locations

The minimal measurement time of about $1\,\mu\mathrm{s}$ [45] of the readout scheme defines a minimal distance of at least $300\,\mathrm{m}$ between the two atom traps for space-like separated measurements. Therefore, we moved one atom trap (trap 2) to a different building of the university giving a distance of $398\,\mathrm{m}$, which provides us with sufficient time margins. A map of the two laboratories is shown in figure 4.1. The map, provided by the Bayrisches Landesamt für Digitalisierung, Breitband und Vermessung, includes coordinates of distinctive parts of the buildings with a high precision. Together with additional measurements of the position of specific components inside the laboratories relative to these coordinates and an evaluation of the relative angles of the buildings, this enables us to exactly determine the distances of all relevant components in both laboratories. Besides the position of the atom traps, it is also essential to know the exact position

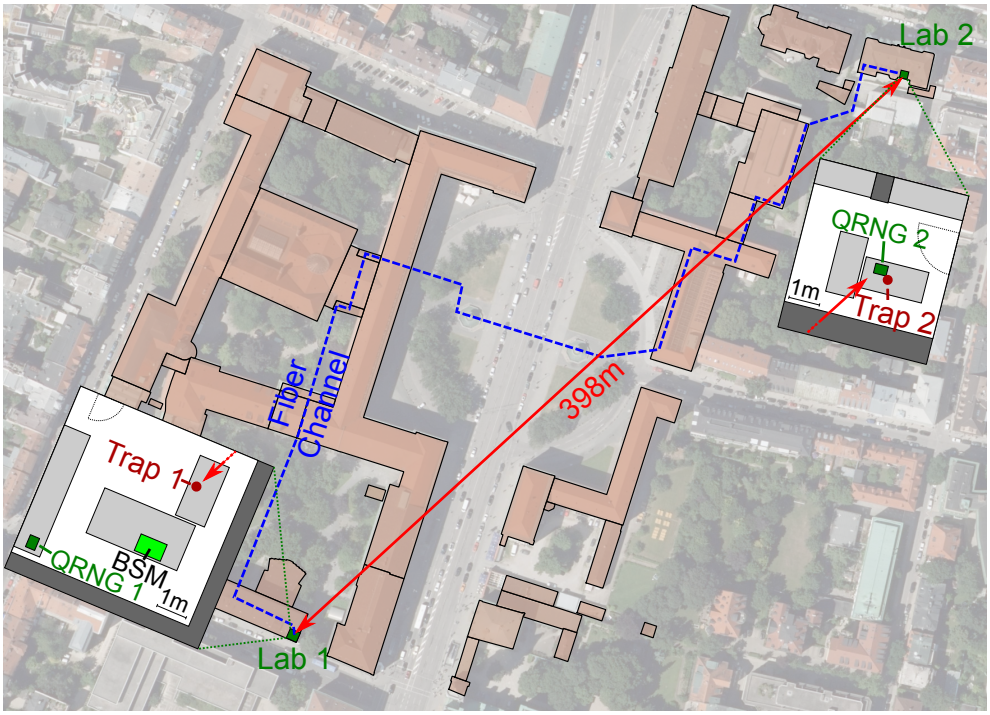

Figure 4.1.: Map of the experiment. The two traps are located in different laboratories (lab 1 and lab 2) in different buildings of the university of Munich. The distance between the trap setups is 398 m. The two labs are connected with a fiber cable that consists of several optical fibers for photon transmission and communication. Map data is provided by Bayrisches Landesamt für Digitalisierung, Breitband und Vermessung.

of the quantum random number generators (QRNG, explained in chapter 6) determining the measurement settings to exclude any causal interconnection. Table 4.1 shows the distances between the different positions. The accuracy of the measurements in the laboratories is better than 10 cm for each direction, thus we assume that the error of the measured distances is definitely smaller than 1 m. The two laboratories are connected by a 700 m long fiber cable that is placed in cable ducts of the university and contains several optical fibers. Their purpose is on the one hand to guide the 780 nm photons emitted by atoms in trap 2 to the BSM setup located in lab 1 and on the other hand to establish a communication link between the two sides.

trap 1 - trap 2	trap 1 - QRNG 2	QRNG 1 - trap 2	QRNG 1 - QRNG 2
398.1 m	398.0 m	402.7 m	402.5 m

Table 4.1.: Distances between the atom traps and quantum random number generators (QRNG) of the two laboratories. The values are obtained by combining measurements in each laboratory with the coordinates provided by the map data.

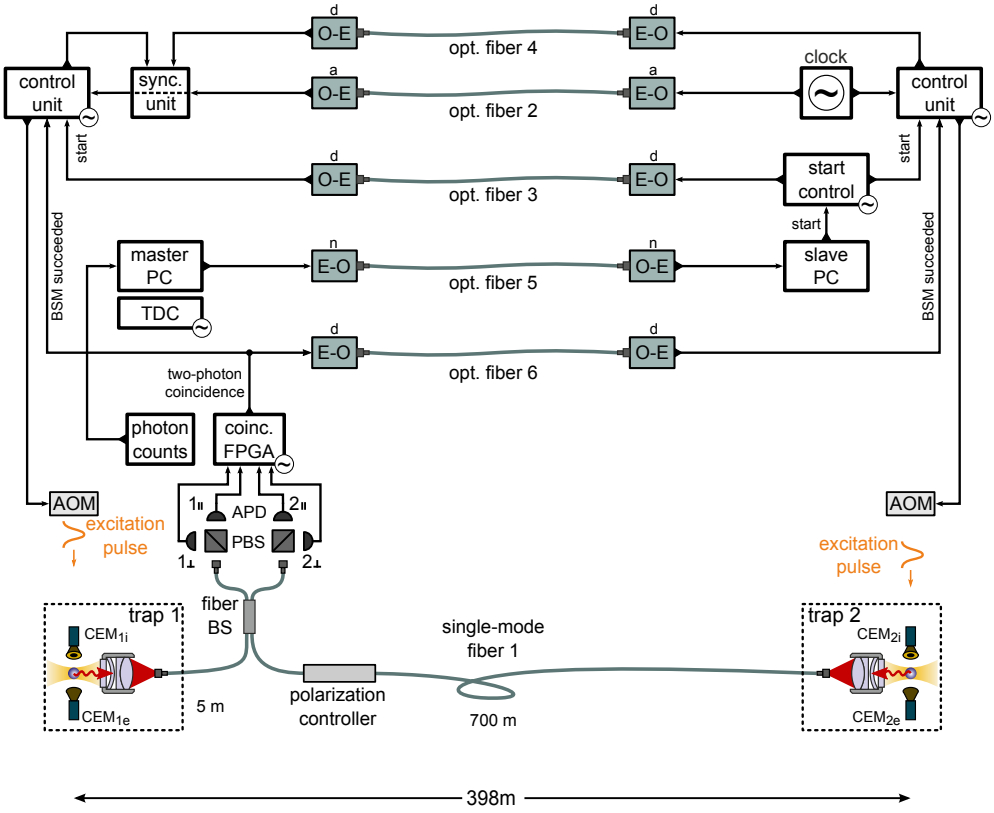

Figure 4.2.: Overview of the experimental setup. The atom traps are connected with the BSM apparatus (with polarizing beam splitters (PBS) and avalanche photo diodes (APD)) by optical fibers. Details about the control of the experiment and the communication between the laboratories are explained in the text.

4.1.2. Control and synchronization

A schematic of the experimental setup is shown in figure 4.2 with the focus on the experimental control. The two atom traps are separated by a distance of $398\,\mathrm{m}$ and photons emitted by the atoms are led to a BSM setup located inside lab 1. Thus, the fiber lengths from the atom traps to the BSM setup differ strongly. While the fiber from trap 1 is about $5\,\mathrm{m}$ long, the fiber from trap 2 has a length of $700\,\mathrm{m}$ (figure 4.2, fiber 1 of the fiber cable).

To control both atom traps and to synchronize them, communication has to be established between the laboratories. Different to earlier experiments over a shorter distance, all communication is done optically. Electrical control signals on the two sides are therefore converted into optical signals which are then transmitted to the other laboratory. Depending on the kind of the signal this is done by analog (a), digital (d) or network (n) electrical-optical converters (E-O, O-E) (figure 4.2, fibers 2-6).

The experiments are controlled by local PCs and programmable control units (CU) in each laboratory. The CUs are custom-built pattern generators that switch all control signals during the experiment. This includes the switching of all lasers (mainly by AOMs), setting acceptance time

windows for time critical events and providing patterns to a time-to-digital converter (TDC) that allow the identification of experimental steps in the evaluation. The CUs are programmed with appropriate patterns and react to external signals that initiate different steps of the experimental sequence. They are operated at a resolution of $20\,\mathrm{ns}$.

The two sides are synchronized with a common $100\,\mathrm{MHz}$ clock. The sinusoidal signal is transmitted from lab 2 to lab 1 via fiber 2 and is distributed to both CUs as well as other time critical components (indicated by the clock symbol $\sim$). Pulses of both CUs are permanently monitored by an additional synchronization unit and the CUs are resynchronized if necessary [43]. Altogether this provides a low timing jitter of $150\,\mathrm{ps}$ rms between both CUs.

The PCs set parameters of the experiment (e.g. laser powers, etc.), perform automatic calibrations (e.g. of the magnetic field sensors, described in the next chapter) and save log files of events (e.g. from the APDs, CEMs and synchronization signals) that are registered by the TDC. The PC in lab 1 acts as master. It continuously analyzes the photon counts at the APDs within $40\,\mathrm{ms}$ time bins and controls the loading operations of trap 1. Via the optical network link (fiber 5) it sends corresponding commands to the slave PC in lab 2.

4.2. Experimental sequence

The two CUs independently control the timing of all steps of the experimental sequence in both laboratories. This sequence is shown in figure 4.3 and consists of the loading of atoms, the generation of atom-photon entanglement, coincidence detection of photons in the BSM setup and the atomic state measurements. In this chapter I will focus on the generation of atom-atom entanglement and analyze the requirements set by the higher distance of the atom traps. A crucial point is the duration of different processes in the experimental sequence which influences the reachable event rate.

4.2.1. Loading of two atom traps

The experimental sequence starts with loading of atoms in both traps. Therefore, the dipole trap and the magneto-optical trap (MOT) are switched on. When an atom is loaded in one of the traps, its fluorescence light increases the count rate of the APDs. In our setup, both traps are observed simultaneously by the APDs of the BSM arrangement and it is necessary to distinguish between the status of both traps. This is achieved by switching the cooling light independently on both sides. The expected increase of the count rate is different for the two traps, on the one hand because of different trap parameters (intensity and detuning of the cooling laser) and on the other hand because of the higher photon loss probability in the longer fiber. Therefore, the expected count rate from trap 2 is smaller than from trap 1 by a factor of about 2. Once an atom is loaded, the atom is stored until the other trap is loaded as well. This is indicated by a rise of the fluorescence counts over a certain threshold (60 counts per $40\,\mathrm{ms}$) that is larger than the background level (about 10 counts per $40\,\mathrm{ms}$) and the fluorescence for each single atom. The fluorescence is constantly monitored and the system automatically detects the loss of one atom when the fluorescence drops below a second threshold of 42 counts per $40\,\mathrm{ms}$.

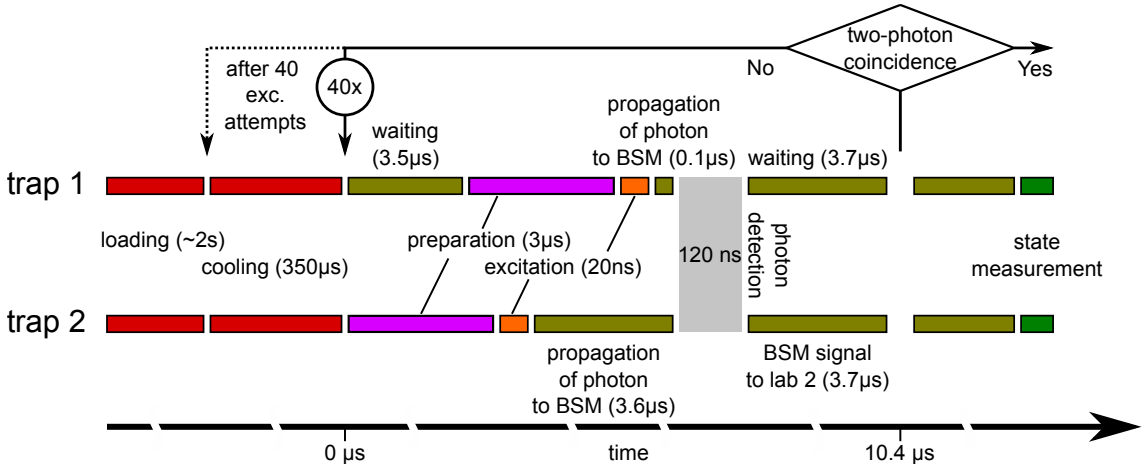

Figure 4.3.: Experimental sequence to entangle two Rubidium atoms. When atoms are loaded in both dipole traps, they are repeatedly prepared and excited to generate atom-photon entanglement. After 40 repetitions of the preparation-excitation cycle recooling of the atoms is necessary. When a two-photon coincidence is registered at the BSM detectors (within a certain photon detection time window) the setup switches to the state analysis.

Then, reloading of the respective trap is initiated. The fluorescence of each trap and also the background level fluctuate over longer time periods. Additionally, different experimental steps have a different fluorescence level which mainly depends on how much light is scattered in the respective procedure. Therefore, finding the optimal thresholds requires a certain optimization of the trapping parameters.

The loading of both atoms typically takes $1 - 3\,\mathrm{s}$ if the MOTs are adjusted optimally. The atoms then stay trapped for several seconds (up to about $10\,\mathrm{s}$) before reloading is necessary. An important criterion for the performance of the atom traps is a high duty cycle, which is the fraction of time where both atoms are present in the trap. The highest duty cycle that we observed is 0.9. However, in most cases it is much smaller (down to 0.33) due to fluctuating loading rates and trapping times.

After loading both atoms, the trap operation is changed to get ready for the experiment: The current of the MOT coils is switched off and the magnetic field stabilization (see chapter 5) is switched on. After $100\,\mathrm{ms}$ the control PC in lab 2 initiates a start signal to both CUs (transmitted to lab 1 via fiber 3, figure 4.2) that switches them to the excitation sequence.

4.2.2. Excitation sequence

The excitation sequence consists of repeated bursts of preparation and excitation cycles to generate entangled atom-photon pairs. Before each excitation pulse, the atoms are prepared in the state $|m_F = 0\rangle_z$ of the $5^2\mathrm{S}_{1/2},\ F = 1$ level by optical pumping. This process takes $3\,\mu\mathrm{s}$ including $1\,\mu\mathrm{s}$ latency of the AOMs. Details and necessary modifications of this pumping scheme compared to

earlier experiments with this system are discussed in section 4.3.1. The excitation pulse with a FWHM of about $20\,\mathrm{ns}$ transfers the state population with high probability to the state $|m_{F'}=0\rangle_z$ of the $5^2\mathrm{P}_{3/2},\ F'=0$ level and the following spontaneous decay provides a photon whose polarization state is entangled with the atomic Zeeman state $|m_F=\pm1\rangle_z$ of the ground level $F=1$ (see section 2.4). The excitation pulses in the two trap setups are synchronized such that the emitted photons have a temporal overlap close to unity at the BSM setup which is, as already mentioned earlier, a mandatory requirement. This is guaranteed by the exactly timed start signal and the synchronization of the clocks of the CUs.

During the preparation-excitation cycle the atom scatters many photons of the pumping and excitation beams. Thus, the atom is heated and the atomic temperature increases. This causes a reduced life time of the atom in the trap and, due to the long times needed to reload one atom, the event rate would drop strongly. Moreover, a low atomic temperature is important for achieving long coherence times as will be shown in chapter 5. To counteract heating, the preparation-excitation cycle is interrupted after every 40 rounds in order to cool the atoms. The cooling is applied for $350\,\mu\mathrm{s}$ before the preparation-excitation cycle resumes.

4.2.3. Photon detection and switching to state measurement

After each excitation attempt the system waits for a possible two-photon coincidence by the detectors of the BSM setup that would herald an entangled atom-atom state. An FPGA analyzes the photon detection events at the APDs within a $120\,\mathrm{ns}$ long time window (figure 4.3) in which the emitted photons are expected. If there is a coincidence of two photons in a detector combination corresponding to a photonic Bell state this heralds an entangled atom-atom state. A joint detection of photons in the detector combinations $1_\parallel \wedge 2_\perp$ or $1_\perp \wedge 2_\parallel$ corresponds to the projection on a $|\Psi^-\rangle$-Bell-state and the detector combinations $1_\parallel \wedge 1_\perp$ or $2_\parallel \wedge 2_\perp$ correspond to the projection on a $|\Psi^+\rangle$-Bell-state (see figure 4.2). If a two-photon coincidence in a Bell-state detector combination is registered, the digital output of the FPGA signals the control units in both laboratories to switch to the state measurement. Otherwise the preparation-excitation cycle will be repeated automatically if no heralding signal arrives at the control units. The probabilities to detect a photon after an excitation attempt are $\eta_1 = 1.65\times10^{-3}$ and $\eta_2 = 0.85\times10^{-3}$ for photons from trap 1 and trap 2, respectively. It is mainly determined by the collection efficiency of the emitted photons with a microscope objective (used NA 0.27 [45]) into a single-mode fiber and by the transmission loss of $50\,\%$ in the long fiber. Therefore the overall probability of a successful BSM event is $\eta = \frac{1}{2}\eta_1\cdot\eta_2 = 0.7\times10^{-6}$, where the factor $\frac{1}{2}$ is due to the fact that only two out of the four Bell-states can be registered with an interferometric BSM setup. To keep the event rate high enough and to collect enough statistics in atom-atom entanglement experiments, a high repetition rate of the excitation is mandatory.

4.2.4. Signal transmission times

Apart from the time needed by preparation-excitation procedures, also the time required for transmitting photons from lab 2 to the BSM as well as for communicating the success of the BSM to lab 2 limit the achievable repetition rate. The first limitation of the repetition rate is the

propagation time of photons to the BSM setup in lab 1 (see figure 4.3). Photons emitted from atoms in trap 2 are transmitted via the $700\,\mathrm{m}$ long fiber. This takes about $\frac{700\mathrm{m}}{2/3\,c} = 3.5\,\mu\mathrm{s}$ plus $0.1\,\mu\mathrm{s}$ in additional fibers inside the laboratories and is an enormous increase in time compared to earlier experiments over $20\,\mathrm{m}$. Photons arriving from atoms in trap 1 only pass a $\sim 5\,\mathrm{m}$ long fiber and arrive at the BSM setup after $74\,\mathrm{ns}$.

An additional time has to be waited for to transmit the success signal of a BSM event to the control units in each laboratory (see figure 4.3). The delay between the APDs detecting the photons and the FPGA switching to the state measurement is $59\,\mathrm{ns}$. The local control unit is connected to the FPGA by a $50\,\mathrm{cm}$ coaxial electrical cable corresponding to an additional delay of only $2.5\,\mathrm{ns}$ while the signal transmission time to the remote laboratory is much longer. The signal is converted into an optical signal by an asynchronous digital electro-optical converter and sent to the other laboratory via the $700\,\mathrm{m}$ cable (fiber 6 in figure 4.2) which takes, including electrical paths inside the laboratories, $3.7\,\mu\mathrm{s}$. Both sides need to wait for the potential success signal to arrive at the remote control unit. If no signal arrives at the CU, the BSM did not succeed and a new preparation-excitation cycle is initiated.

Due to the long signal transmission times, the atomic state analysis of atoms in trap 2 has to be performed at least $7.3\,\mu\mathrm{s}$ after the excitation of the atom. For simultaneous measurements (as indicated in figure 4.3), the state analysis in trap 1 then requires a time delay of at least $3.8\,\mu\mathrm{s}$. Consequences of the time delays for the fidelity of the atomic state analysis will be discussed in chapter 5.

4.3. Optimization of the event rate

For maximizing the achievable event rate, the timing of the experimental sequence has to be optimized. In the following, I will show how the time needed for the state preparation could be reduced.

4.3.1. State preparation by optical pumping

The efficient preparation of the state $|m_F = 0\rangle_z$ of the ground level before each excitation attempt is crucial for obtaining a high repetition rate. It is done by optical pumping with two lasers, the first one addressing the transition $5^2\mathrm{S}_{1/2},\ F = 2 \rightarrow 5^2\mathrm{P}_{3/2},\ F' = 1$ (short: $2 \rightarrow 1$) and the second $5^2\mathrm{S}_{1/2},\ F = 1,\ m_F = \pm 1 \rightarrow 5^2P_{3/2},\ F' = 1,\ m_F = \pm 1$ (short: $1 \rightarrow 1$) (see figure 4.4). The aim is to continuously excite all states to the $F' = 1$ level except for the state to be prepared which is thus a dark state for this excitation light. From the various states of the $F' = 1$ level the atom decays back to all possible states, but also with a certain probability to the dark state $|m_F = 0\rangle_z$. After several cycles, all other states will get depopulated.

For that purpose, the pump laser for $1 \rightarrow 1$ is chosen to be π-polarized, such that only the states $|m_F = \pm 1\rangle_z$ can be excited. The state selection gets more complicated for the pump laser for $2 \rightarrow 1$. For a single light field with a specific polarization resonant to the transition $F = 2 \rightarrow F' = 1$, two out of five states of $F = 2$ are dark states (shown in figure 4.4 for the case of σ^+ polarization). Therefore, after the pumping procedure the population of the

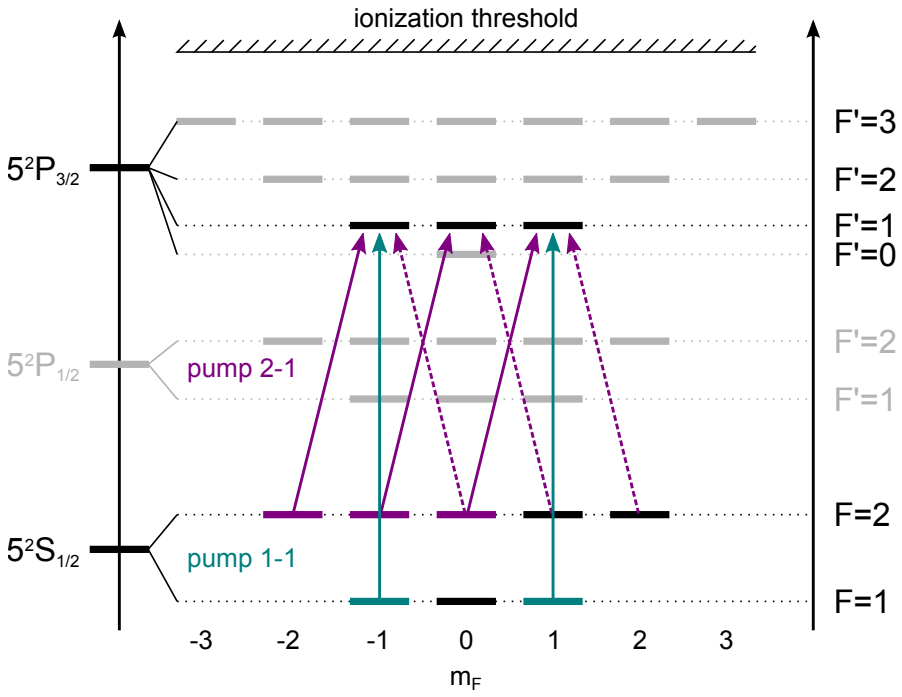

Figure 4.4.: Atomic transitions and light polarizations used to prepare the atom in the state $|F = 1, m_F = 0\rangle_z$. The pump laser for $1 \rightarrow 1$ excites atoms in the states $|F = 1, m_F = \pm 1\rangle_z$ and the pump laser for $2 \rightarrow 1$ excites atoms in the $F = 2$ level. Within a few μs, the atoms are transfered to the final state $|F = 1, m_F = 0\rangle_z$ with high probability. To avoid dark states in the $F = 2$ level, the polarization of the pump laser for $2 \rightarrow 1$ has to be changed during the state preparation.

$F = 2$ level can be as high as $40\,\%$. In previous experiments [40] this was avoided by mixing the Zeeman states of the hyperfine level $F = 2$ by additionally switching on the cooling laser and thereby exciting the atoms to $F' = 3$. The following decay transfers the atom back to the $F = 2$ level of the ground state but (with a certain probability) to another Zeeman state. While this method actually works well and the remaining population of the $F = 2$ level is close to 0 after the pumping procedure, it takes additional time because more excitations are necessary until the pumping is finished. Additionally, more excitations will heat the atom stronger and therefore increase the atomic temperature which has the consequence that less repetitions of the preparation-excitation cycle can be performed before cooling is necessary. We thus modified the pumping scheme to obtain a high efficiency without the mixing of states.

4.3.2. Improving the pumping scheme

A solution to avoid the use of the cooling laser, and to avoid the dark states, is using two beams of the pump laser for $2 \rightarrow 1$ with different polarizations. Then, as indicated in figure 4.4 for σ^+ and σ^- polarization, all states will be addressed. However, splitting a single laser beam in two parts and setting different polarizations does not work, since the two beams remain coherent. At the position of the atom the electric field vectors add and result in a well-defined polarization that again gives two dark states for the transition. To avoid this, we temporally separate the two beams by alternately switching the beams on and off with a period of $150\,\mathrm{ns}$. Thus, pumping is done for $75\,\mathrm{ns}$ with one polarization, then the same time with the second polarization. This is repeated for the entire pumping sequence of $2\,\mu\mathrm{s}$.

Technically, this is realized by using one laser beam that is chopped on and off by an AOM at a frequency of $6.6\,\mathrm{MHz}$. The chopped laser pulse is then split into two beams and coupled into two fibers. The fibers leading to the atom trap have different length. The additional propagation time of the beam in the longer fiber is half the period of the chopping signal, i.e. $75\,\mathrm{ns}$. Therefore, the pulses are deferred relative to each other such that only one of the beams is on at any time. The required length difference of the fibers is $15\,\mathrm{m}$ to achieve this shift. Before the trap, the polarizations are set (right-circular) and the beams are directed onto the atom from opposing directions.

Due to its different geometry, trap 2 has a different implementation of this pumping scheme. Here, the chopped laser pulse has a period of $150\,\mathrm{ns}$ of which it is on for $100\,\mathrm{ns}$. The beam is overlapped with the cooling light that is split into three parts and arrives at the atom from three different directions. The fiber lengths for the three arms differ by $10\,\mathrm{m}$. Thus, the delay of the second path is $50\,\mathrm{ns}$ and of the third path $100\,\mathrm{ns}$. As a result, two beams are switched on simultaneously while the third beam is switched off and the combinations of pairs changes over time. This is more complex then the approach for trap 1 and it is hard to prove that the resulting polarizations do not have any dark states. However, measurements revealed that this layout also works and it was easier to modify the setup that way because of a restricted accessibility from other directions. A disadvantage is that as the cooling beams have a large waist, this approach requires much more power for each pumping beam.

4.3.3. Measuring the pumping efficiency

To verify that the new pumping scheme works well we measure the probability to find the atom in the level $F = 2$ after applying the pumping sequence. This is done by exciting atoms in the level $F = 2$ by the cycling laser (see appendix B) to the level $F' = 3$ and ionizing them, whereas atoms in the level $F = 1$ are not ionized. The ionization probability then directly corresponds to the residual probability that the atom is in the level $F = 2$. The result is shown in figure 4.5 a) where the ionization probability is shown as a function of the number of repetitions of the preparation-excitation cycle. The resulting efficiency of the pumping from $F = 2$ to $F = 1$ is 0.945 ± 0.003.

Additionally, we measure the probability that the atom is in the desired Zeeman state $|m_F = 0\rangle_z$ after the pumping sequence. Therefore, we use our state readout scheme (see section 2.5). In the first setting the readout beam is vertically polarized and excites the Zeeman states $\frac{1}{\sqrt{2}}(|m_F = +1\rangle_z + |m_F = -1\rangle_z)$ and $|m_F = 0\rangle_z$ which then get ionized. The probability $1 - P_{\text{ion}\,1}$ that the atom is not ionized then corresponds to the probability that the atom is in the state $\frac{i}{\sqrt{2}}(|m_F = +1\rangle_z - |m_F = -1\rangle_z)$ after the pumping. In the second setting the readout beam is horizontally polarized and excites and ionizes the Zeeman states $\frac{i}{\sqrt{2}}(|m_F = +1\rangle_z - |m_F = -1\rangle_z)$ and $|m_F = 0\rangle_z$. Here, $1 - P_{\text{ion}\,2}$ is the probability that the atom was not ionized and therefore is in the state $\frac{1}{\sqrt{2}}(|m_F = +1\rangle_z + |m_F = -1\rangle_z)$. Thus, we can obtain the probability $P(F = 1,\, m_F = 0)$ that the atom is in the desired target state after applying the pumping scheme from these measurements. With the ionization probabilities $P_{\text{ion}\,1/2}$ for setting 1 and 2 and the probability $P(F = 2)$ that the atom is in the level $F = 2$ after the pumping we get

$$P(F = 1,\, m_F = 0) = 1 - (1 - P_{\text{ion}\,1} + 1 - P_{\text{ion}\,2} + P(F = 2)) \tag{4.1}$$

(which is not corrected for errors of the ionization scheme). Figure 4.5 b) shows the measured state populations of the desired state $|m_F = 0\rangle_z$ (red), of the state $\frac{1}{\sqrt{2}}(|m_F = +1\rangle_z + |m_F = -1\rangle_z)$ (blue), and of the state $\frac{i}{\sqrt{2}}(|m_F = +1\rangle_z - |m_F = -1\rangle_z)$ (green) as a function of the number of repetitions of the preparation-excitation cycle. As result, we obtain a probability to pump the atom to the desired state before each excitation of $P(F = 1,\, m_F = 0) = 0.774 \pm 0.018$.

While the pumping efficiency is the same with the new pumping scheme, it allowed us to reduce the duration of the state preparation from $5\,\mu$s to $3\,\mu$s. In addition, due to less heating, the number of repetitions of the preparation-excitation cycle could be increased from 20 to 40 before cooling is necessary.

4.4. Repetition rate and expected event rate

All durations in the experimental sequence together allow us to calculate the effective repetition rate of the excitation pulses. The time between two consecutive excitations in the CU pattern is $10.36\,\mu$s. This sequence is repeated 40 times before the atoms are recooled for $350\,\mu$s. Every first state preparation directly after the intermediate cooling is $2\,\mu$s longer ($5\,\mu$s instead of $3\,\mu$s), since the atom is then in the $F = 2$ level. The total time for 40 excitations therefore is $40 \cdot 10.36\,\mu\text{s} +$

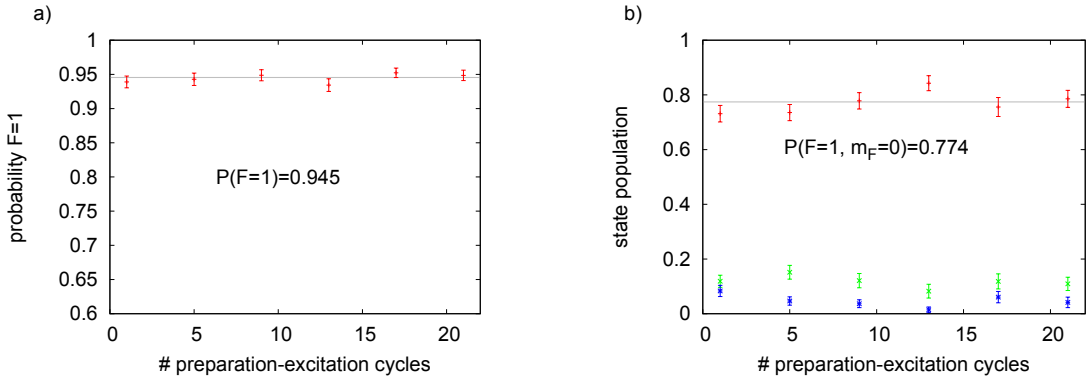

Figure 4.5.: Measurements to determine the probability to pump into the desired state. Both measurements are shown for a different number of repetitions of the preparation-excitation cycle. After the last state preparation, the resulting state is measured. a) Efficiency of depopulating $F = 2$. Only atoms in the hyperfine level $F = 2$ are ionized. b) Efficiency of pumping into $F = 1$, $m_F = 0$. Measured state populations of $\frac{1}{\sqrt{2}}(|m_F = +1\rangle_z + |m_F = -1\rangle_z)$ (blue), $\frac{i}{\sqrt{2}}(|m_F = +1\rangle_z - |m_F = -1\rangle_z)$ (green) and the calculated population of $|m_F = 0\rangle_z$ (red, according to equation 4.1).

$2\,\mu\text{s} + 350\,\mu\text{s} = 766.4\,\mu\text{s}$. Consequentially, the effective repetition rate is

$$R_{\text{exc}} = \frac{\text{excitation attempts}}{\text{time}} = \frac{40}{766.4\,\mu\text{s}} = 52.2 \times 10^3\,\frac{1}{\text{s}}. \tag{4.2}$$

The maximal rate of atom-atom entanglement events with the probability of a two photon coincidence $\eta = 0.7 \times 10^{-6}$ (section 4.2.3) is therefore 2.2 events per minute. Depending on the lifetime of the atoms in the traps and on the loading rates, the expected event rate is lower. The percentage of time both atoms are present in the trap is typically between $33\,\%$ and $90\,\%$ giving effective event rates of up to 2 events per minute. Compared to earlier experiments (e.g. the teleportation experiment with a repetition rate of $50.9 \times 10^3\,\frac{1}{\text{s}}$ (equation 3.17)) we find that despite the increased waiting times for photon and signal transmission, we could maintain the repetition rate. The event rate is actually slightly higher than in earlier experiments due to an improvement in the lifetime of atoms in the trap.

4.5. Summary

This chapter described the setup and the experimental sequence to entangle two atoms over a distance of $398\,\text{m}$. The basics of the experimental scheme are similar to earlier implementations where the atoms were separated by $20\,\text{m}$ [25, 43]. The larger distance especially causes increased propagation times of photons and control signals between the laboratories and an increased photon loss probability in longer optical fibers. To increase the reachable event rate we optimized the

experimental sequence, in particular the scheme for the pumping. Altogether these optimizations allowed us to achieve an even higher repetition rate of $R_{\mathrm{exc}} = 52.2 \times 10^3 \, \frac{1}{\mathrm{s}}$ and thereby a higher rate of atom-atom entanglement events than in earlier experiments.

While the generation of atom-atom entanglement could be scaled with these modifications to a longer distance, there is a large impact on the measurement of atomic states. The challenges and improvements regarding the analysis of atomic states will be discussed in the next chapter.

5. Coherence properties of the atomic qubit

The most challenging requirement to increase the distance of the two atom traps from initially $20\,\mathrm{m}$ to $398\,\mathrm{m}$ is achieving a correspondingly long coherence time of the atomic states. The delay between the generation of atom-photon entanglement and the state measurement is increased due to the additional (signal) propagation times discussed in section 4.2.4 to at least $3.8\,\mu s$ and $7.3\,\mu s$ for the two traps during which the atomic states have to be preserved with as high fidelity as possible. This is a huge difference compared to the few hundred ns in experiments over $20\,\mathrm{m}$ [25] and requires a better control of the quantum system. In this chapter I will explain the influence of magnetic fields (Zeeman effect) and the light of the dipole trap (AC-Stark effect) on the coherence of the atomic states and present the solutions necessary for a long-distance experiment.

To determine the factors influencing the coherence times, we generate atom-photon entanglement and measure the polarization of the photon which should be strictly correlated with the measurement results of the atomic state. These correlations are then measured for different time delays of the atomic state analysis. We distinguish between "time-delay-independent" and "time-delay-dependent" effects that reduce the measured correlations of the atom-photon state. For time-delay-independent effects (e.g. due to limitations of the readout scheme) the measurement results do not depend on the delay of the state analysis. In contrast, both the Zeeman and the AC-Stark effect cause a time evolution of the atomic states that is negligible for short delays, but clearly visible in our case.

5.1. Atomic state evolution in magnetic and optical fields

5.1.1. Zeeman effect in a spin-1 system

The energies of atomic states in an external magnetic field are shifted due to the Zeeman effect. To calculate this shift and the resulting time evolution of states, called Larmor precession, I follow earlier descriptions presented in [41]. Our atomic qubit is encoded in a superposition of the Zeeman states of the ground level $|F = 1, m_F = \pm 1\rangle_z$ (short: $|1, \pm 1\rangle_z$). However, the ground level has spin 1 and we also have to consider the state $|1, 0\rangle_z$ with $m_F = 0$. The Zeeman shift of these states in an external magnetic field $\vec{B} = B_0(b_x\vec{e}_x + b_y\vec{e}_y + b_z\vec{e}_z)$ with $b_x^2 + b_y^2 + b_z^2 = 1$ is described by the Hamiltonian (in the basis ($|1, +1\rangle_z$, $|1, 0\rangle_z$, $|1, -1\rangle_z$))

$$\begin{aligned}\hat{H} &= \frac{\mu_B g_F}{\hbar}\vec{B}\hat{\vec{F}} \\ &= g_F\mu_B B_0 \begin{pmatrix} b_z & \frac{1}{\sqrt{2}}(b_x - ib_y) & 0 \\ \frac{1}{\sqrt{2}}(b_x + ib_y) & 0 & \frac{1}{\sqrt{2}}(b_x - ib_y) \\ 0 & \frac{1}{\sqrt{2}}(b_x + ib_y) & -b_z \end{pmatrix}, \end{aligned} \tag{5.1}$$

with the Bohr magneton μ_B, the Landé factor g_F and the angular momentum operators $\hat{\vec{F}} = \begin{pmatrix} \hat{F}_x \\ \hat{F}_y \\ \hat{F}_z \end{pmatrix}$ defined for a spin-1 system as

$$\begin{aligned}\hat{F}_x &= \frac{1}{\sqrt{2}} \begin{pmatrix} 0 & 1 & 0 \\ 1 & 0 & 1 \\ 0 & 1 & 0 \end{pmatrix}, \\ \hat{F}_y &= \frac{i}{\sqrt{2}} \begin{pmatrix} 0 & -1 & 0 \\ 1 & 0 & -1 \\ 0 & 1 & 0 \end{pmatrix}, \\ \hat{F}_z &= \frac{1}{\sqrt{2}} \begin{pmatrix} 1 & 0 & 0 \\ 0 & 0 & 0 \\ 0 & 0 & -1 \end{pmatrix}. \end{aligned}$$

With the Larmor frequency $\omega_L := \frac{1}{\hbar} g_F \mu_B B_0$ and the relations $b_x = \sqrt{1 - b_z^2}\sin(\phi)$ and $b_y = \sqrt{1 - b_z^2}\cos(\phi)$ (that differ from reference [41] due to the different coordinate system (see figure 2.2)), one gets

$$\hat{H} = \hbar\omega_L \begin{pmatrix} b_z & \frac{-i}{\sqrt{2}}\sqrt{1 - b_z^2}e^{i\phi} & 0 \\ \frac{i}{\sqrt{2}}\sqrt{1 - b_z^2}e^{-i\phi} & 0 & \frac{-i}{\sqrt{2}}\sqrt{1 - b_z^2}e^{i\phi} \\ 0 & \frac{i}{\sqrt{2}}\sqrt{1 - b_z^2}e^{-i\phi} & -b_z \end{pmatrix}. \tag{5.2}$$

The eigenstates of this Hamiltonian to the eigenvalues $\lambda = -\hbar\omega_L,\ 0,\ +\hbar\omega_L$ are

$$\begin{aligned}|\Phi_{-1}\rangle &= \begin{pmatrix} \frac{1}{2}(-1 + b_z)e^{i\phi} \\ \frac{i}{\sqrt{2}}\sqrt{1 - b_z^2} \\ \frac{1}{2}(1 + b_z)e^{-i\phi} \end{pmatrix}, \\ |\Phi_0\rangle &= \begin{pmatrix} \frac{1}{\sqrt{2}}\sqrt{1 - b_z^2}e^{i\phi} \\ -ib_z \\ \frac{1}{\sqrt{2}}\sqrt{1 - b_z^2}e^{-i\phi} \end{pmatrix}, \\ |\Phi_{+1}\rangle &= \begin{pmatrix} \frac{1}{2}(1 + b_z)e^{i\phi} \\ \frac{i}{\sqrt{2}}\sqrt{1 - b_z^2} \\ \frac{1}{2}(-1 + b_z)e^{-i\phi} \end{pmatrix}, \end{aligned}$$

and the time evolution of an arbitrary state $|\Psi_0\rangle = c_{-1}|\Phi_{-1}\rangle + c_0|\Phi_0\rangle + c_{+1}|\Phi_{+1}\rangle$ in a constant magnetic field is given by

$$|\Psi_0(t)\rangle \quad = \quad c_{-1}|\Phi_{-1}\rangle e^{i\omega_L t} + c_0|\Phi_0\rangle + c_{+1}|\Phi_{+1}\rangle e^{-i\omega_L t}. \tag{5.3}$$

To illustrate the impact of the time evolution on our experiments and how the influence of magnetic fields on the atomic states is measured, I will use specific examples.

Measuring the time evolution of states

To measure the time evolution, the atomic state is prepared by generating atom-photon entanglement according to section 2.4 and measuring the photon polarization. In most characterization measurements the photon is analyzed in the basis H/V, projecting the atom on either $|\Psi_H\rangle = \frac{1}{\sqrt{2}}(|1,+1\rangle_z + |1,-1\rangle_z)$ or $|\Psi_V\rangle = \frac{i}{\sqrt{2}}(|1,+1\rangle_z - |1,-1\rangle_z)$. A measurement of the atomic state is a projection on the bright and dark state defined in equation 2.6. The measurement result is obtained by the state selective ionization scheme, where atoms in the bright state $|\Psi_B\rangle$ get ionized contrary to atoms in the dark state $|\Psi_D\rangle$. To be able to distinguish between the two generated states we set the polarization of the readout beam to be such that $|\Psi_D\rangle = |\Psi_V\rangle$ and $|\Psi_B\rangle = |\Psi_H\rangle$. Atoms in the state $|m_F = 0\rangle_z$ are also ionized. This means that the measurement determines the dark state correctly whereas the detection of an atom in the bright state can also originate from the state $|m_F = 0\rangle_z$.

The time evolution is determined by time resolved measurements. After the projection of the atomic state on $|\Psi_H\rangle$ or $|\Psi_V\rangle$ the setup waits for a variable time t before the atomic state is projected onto the dark state and the state population of the dark state is evaluated (after averaging over a sufficient number of events). At the time $t = 0$, the polarization measurement of the photon directly determines the result of the atomic state measurement up to the fidelity of the state analysis. For times $t > 0$ the state population can change due to the state evolution in magnetic fields.

Field in z-direction

Let us first assume a magnetic field in the z-direction with $b_z = 1$ and $b_x = b_y = 0$. Then, the eigenstates of the Hamiltonian are

$$|\Phi_{-1}\rangle = \begin{pmatrix} 0 \\ 0 \\ 1 \end{pmatrix}, \; |\Phi_0\rangle = \begin{pmatrix} 0 \\ -i \\ 0 \end{pmatrix}, \; |\Phi_{+1}\rangle = \begin{pmatrix} 1 \\ 0 \\ 0 \end{pmatrix},$$

which gives the time evolution of the states $|\Psi_H(t)\rangle = \frac{1}{\sqrt{2}}(|1,+1\rangle_z e^{-i\omega_L t} + |1,-1\rangle_z e^{i\omega_L t})$ and $|\Psi_V(t)\rangle = \frac{i}{\sqrt{2}}(|1,+1\rangle_z e^{-i\omega_L t} - |1,-1\rangle_z e^{i\omega_L t})$. The probability to measure the atom in the dark state after a certain time t is then $P(|\Psi_D\rangle) = \sin^2(\omega_L t)$ for atoms prepared in the state $|\Psi_H\rangle$. Atoms prepared in the state $|\Psi_V\rangle$ on the contrary will be found in the dark state with probability $P(|\Psi_D\rangle) = \cos^2(\omega_L t)$. Therefore, in a magnetic field in z-direction, states $|\Psi_V\rangle$ and $|\Psi_H\rangle$ show

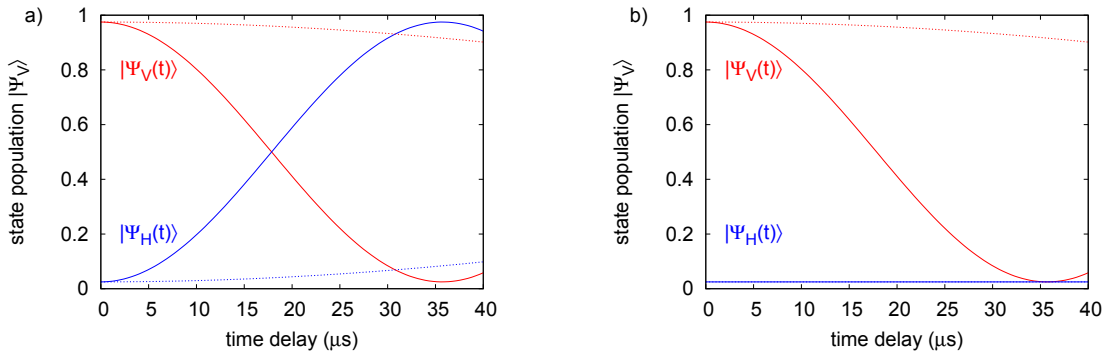

Figure 5.1.: Calculated time evolution of the states $|\Psi_V\rangle$ and $|\Psi_H\rangle$ (projected on $|\Psi_V\rangle$) for magnetic fields in the a) z-direction and b) x-direction of $10\,\mathrm{mG}$ (solid) and $1.6\,\mathrm{mG}$ (dashed). The obtained curves can be compared to the results of time resolved measurements.

Larmor precession with the frequency $2\omega_L$ and the population of the state $|m_F = 0\rangle_z$ remains zero. The expected result of time resolved measurements is shown in figure 5.1 a) for magnetic fields of $10\,\mathrm{mG}$ and $1.6\,\mathrm{mG}$.

Field in x-direction

The behavior is different for magnetic fields in the x and y direction. The eigenstates of the Hamiltonian for a field along x ($b_z = 0$, $\phi = \pi/2$) are:

$$|\Phi_{-1}\rangle = \frac{1}{2}\begin{pmatrix} -1 \\ \sqrt{2}\,i \\ 1 \end{pmatrix},\ |\Phi_0\rangle = \frac{1}{\sqrt{2}}\begin{pmatrix} 1 \\ 0 \\ 1 \end{pmatrix},\ |\Phi_{+1}\rangle = \frac{1}{2}\begin{pmatrix} 1 \\ \sqrt{2}\,i \\ -1 \end{pmatrix}$$

In this basis the prepared states are $|\Psi_V\rangle = \frac{i}{\sqrt{2}}(|\Phi_{+1}\rangle - |\Phi_{-1}\rangle)$ and $|\Psi_H\rangle = |\Phi_0\rangle$ resulting in time evolutions $|\Psi_V(t)\rangle = |\Psi_V\rangle\cos(\omega_L t) + i|1,0\rangle_z \sin(\omega_L t)$ and $|\Psi_H(t)\rangle = |\Psi_H\rangle = const.$ Using the same measurement basis as above, $|\Psi_V(t)\rangle$ is initially the dark state, but rotates into the state $|m_F = 0\rangle_z$ which is a bright state. Therefore, the projection of atoms prepared in this state onto the dark state will show oscillations in time resolved measurements. On the contrary, the time evolution of the population of atoms prepared in the state $|\Psi_H\rangle$ is constant (see figure 5.1 b)).

Field in y-direction

If the direction of the magnetic field is along the y-axis, the state evolution will be similar, but now the state $|\Psi_H\rangle$ will rotate into the state $|m_F = 0\rangle_z$ while the state $|\Psi_V\rangle$ remains constant. In the usual measurement basis, this means there is no observable time dependence because the

only rotation is between two states that are both ionized during the state analysis. To observe the influence of the magnetic field in the y-direction in time resolved measurements, the measurement basis has to be rotated by $180°$ changing the dark and bright state to $|\Psi_D\rangle = |\Psi_H\rangle$ and $|\Psi_B\rangle = |\Psi_V\rangle$.

Required stability of magnetic fields

The Larmor frequency $\omega_L = \frac{1}{\hbar} g_F \mu_B B_0$ depends on the strength of the magnetic field. To estimate the required stability of these fields for experiments over the long distance with estimated time delays of about $10\,\mu$s, we require that the contrast of atom-photon correlations may not be reduced by more than $1.0\,\%$. This sets a limit of the Larmor frequency of $\omega_L < 7.1 \times 10^3 \frac{1}{\mathrm{s}}$ and a maximally allowed ambient magnetic field of $B_a = 1.6\,\mathrm{mG}$.

So far we considered the state evolution in a single experimental repetition (single shot). However, in experiments, many (~ 1000) events are averaged that are recorded in a time interval of several minutes to hours. If the magnetic field strength varies, the time evolution of states and especially the Larmor frequency will be different for every event and the resulting averaged evolution will wash out ("shot-to-shot dephasing") [41]. Magnetic fields therefore have to be stabilized to the required accuracy of $1.6\,\mathrm{mG}$ which was realized in this thesis and is described in the next sections.

5.1.2. Compensation of magnetic fields

The experimental environment consists of many sources of magnetic fields. This includes sources inside the laboratory, e.g. magnetic components and electronic devices, as well as distant sources like a subway line at a distance of about $60\,\mathrm{m}$. To avoid time evolution of the atomic states, ambient magnetic fields $\vec{B}_a$ have to be compensated and in the case of fluctuating fields a stabilization is mandatory. Therefore, we use an active field compensation by applying a so-called compensation field. The setup and the compensation procedure will be explained in the following.

Setup of the relevant components

The setup of the components used for the compensation of magnetic fields is shown in figure 5.2 for both atom trap setups. The atom trap is located inside the vacuum glass cell between the upper and the lower MOT coil. To compensate ambient magnetic fields, a magneto-resistive feedback sensor (Honeywell HMC 1053) is attached to the frame of the MOT coils and placed close to the position of the atom trap [41]. The sensor measures the magnetic fields in all three directions (x, y, z) and gives a feedback signal to the current source driving 3 pairs of compensation coils. The compensation coils are wound on rectangular frames forming approximately a cube with an edge length of about $23\,\mathrm{cm} \pm 1.5\,\mathrm{cm}$ such that they are arranged approximately in a Helmholtz configuration around the atom trap. Each pair of coils generates a magnetic field in one of the three directions such that the generated compensation field is $\vec{B}_{comp} = -\vec{B}_a$.

The feedback sensor provides output voltages $U^{(i)}$ ($i \in \{x, y, z\}$) that depend linearly on the magnetic field components $B^{(i)}$ at this position according to

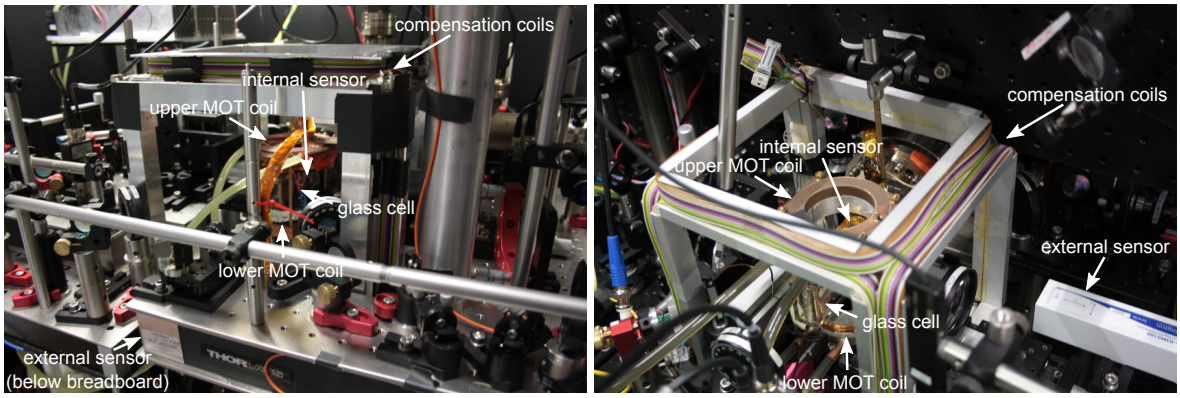

Figure 5.2.: Experimental setup with magneto-resistive sensors, MOT and compensation coils. The atom is located inside the vacuum glass cell between the upper and lower MOT coil. The internal magneto-resistive sensor is placed close to the atomic position inside the MOT coils. The compensation coils are built around the whole setup at a distance that is sufficient to guarantee an almost homogeneous compensation field. External sensors (explained in section 5.1.3) are placed at a certain distance to the setup. The two trap setups (left: trap 1, right: trap 2) have different positions and orientations of sensors.

$$U^{(i)} \quad = \quad s^{(i)} \cdot B^{(i)} + U^{(i)}_{\text{offset}}, \tag{5.4}$$

with a certain sensitivity $s^{(i)}$ that has different values for the three directions (about $1\,\frac{\text{mV}}{\text{mG}}$ including the pre-amplifier). Each output voltage has an offset $U^{(i)}_{\text{offset}}$ of several hundred mV. A PID controller compares the output voltages to preset reference values $U^{(i)}_{ref}$ and controls the current source of the compensation coils. The magnetic field generated by the compensation coils then leads to stable output voltages of the sensor $U^{(i)} = U^{(i)}_{ref}$. This forms a feedback loop of the sensor and the coils which allows stabilizing magnetic fields with fluctuations up to $\sim 200\,\text{Hz}$ [41]. However, the distance between the position of the atom and the position of the sensor is a few cm which means that the measured field can differ from the magnetic field at the position of the atom. Furthermore, the value of the offset voltage of the sensor is not known precisely. Thus, the reference values of the feedback loop that correspond to zero magnetic field at the position of the atom have to be determined.

Compensation procedure

Finding the desired reference values $U^{(i)}_{ref}$ that correspond to zero magnetic field at the position of the atom is done in a step-by-step approach.

Initially, voltages are chosen that are obtained according to measurements of the magnetic field with an additional hand-held sensor close to the atom trap. This method is quite inaccurate and only reduces the magnetic field to the order of $10\,\text{mG}$. To determine the remaining field at the

position of the atom, time resolved measurements, as explained in the last section, are performed in order to directly determine the time evolution of the atomic states.

The measured time evolution of the two observed states $|\Psi_H(t)\rangle$ and $|\Psi_V(t)\rangle$ is in general too complex to directly determine the remaining field because it can point in an arbitrary direction. Therefore, an iterative reduction of the magnetic field is required in which the reference value for one component of the magnetic compensation field is changed with the aim to slow down the temporal changes of the prepared states. This is done sub-sequentially for all three directions until the observed changes of the atomic states are minimized. From there on, the currents of the compensation coils are set according to keep the output voltages of the magnetic field sensor constant.

While this approach was sufficient for previous applications with short delays between the generation of the entangled atom-photon pairs and the state measurement, a long-distance experiment requires longer time delays before the measurement. The stability provided by this compensation scheme turned out to be insufficient, due to drifts of the magnetic field sensor.

5.1.3. Drifts of the feedback sensor

Time resolved state measurements show long coherence times right after an optimization of the magnetic field compensation as illustrated in figure 5.3 a). The fidelity of the state remains almost unaffected at a time delay of $10\,\mu\mathrm{s}$ which corresponds to a typical measurement delay for the $398\,\mathrm{m}$ experiment. However, measurements averaged over longer time periods revealed a reduction of the fidelity. This reduction occurs at different timescales from several minutes to hours. The reason for this instability are drifts of the output voltage of the feedback sensor when the sensor is exposed to strong magnetic fields as it is the case during the loading of atoms, when the magnetic field of the MOT is switched on. We attribute these drifts to a change of the offset voltage of the sensor $U^{(i)}_{\mathrm{offset}} \rightarrow U^{(i)}_{\mathrm{offset}} + \Delta U^{(i)}_{\mathrm{offset}}(t)$, defined in equation 5.4 (the sensitivity of the sensor seems to be very stable). The offset drift effectively changes the zero-point of the magnetic field compensation. Thus, the feedback loop will stabilize the magnetic field to a value that corresponds to the change of the offset divided by the sensitivity $\Delta U^{(i)}_{\mathrm{offset}}/s^{(i)}$. The impact of these drifts on the state fidelity are shown in figure 5.3 b) for a measurement with a constant time delay of $21\,\mu\mathrm{s}$. Over 20 hours, the state fidelity decreases (red data points) due to a magnetic field change that is mainly along the x-direction for the trap 2 setup (for trap 1 the position of the sensor is different and the z-axis is influenced stronger). The change of the magnetic field after $20\,\mathrm{h}$ is about $4\,\mathrm{mG}$ in this measurement.

The sensor drifts are correlated to the magnetic field generated by the MOT coils. Changing the direction of the MOT current also reverses the direction of the drifts and both the timescale and the maximal change depend on the current and therefore the applied magnetic field strength. Thus, we assume that the drift is caused by a magnetization of the sensor in the MOT field that happens on a long timescale. Hence, a closer look at the magnetic field at the position of the sensor is desirable. A numerical calculation of the MOT field is evaluated with Mathematica using the Biot-Savart law (see appendix E). The resulting magnetic field for the sensor is $26.25\,\mathrm{G}$ and $40.92\,\mathrm{G}$ for the two trap setups, respectively, with the dominant field component pointing in

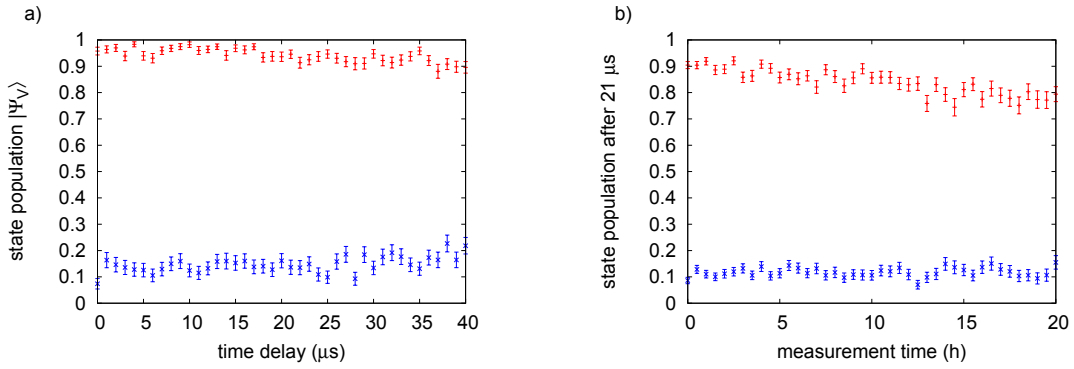

Figure 5.3.: Measured population of $|\Psi_V\rangle$ for atoms prepared in the states $|\Psi_H\rangle$ (blue) and $|\Psi_V\rangle$ (red). a) The atomic states show almost no time evolution up to a time delay of $40\,\mu$s directly after a compensation of the magnetic field. b) Drift of the sensor within $20\,$h (after an optimization) causes a significant change in the state fidelity, measured at a constant time delay of $21\,\mu$s. This drift implies a varying magnetic field along the x-direction caused by offset drifts of the magneto-resistive sensor.

the y-direction. However, the strongest drifts of the sensor are along z (x for trap 2) and there is no clear dependency of the sensor drifts on the direction of the magnetic field vector.

Further information about the drifts is obtained by comparing the internal feedback sensor to a long-term stable external sensor (fluxgate, Bartington Mag-03MS100, see figure 5.2) that is placed outside the MOT and compensation coils. To compare the output voltages of both sensors, the current of the MOT coils is switched off and the current of the compensation coils is set to a constant value (without the feedback stabilization). The output voltages of both sensors $U_i^{(i)}$ (internal sensor) and $U_e^{(i)}$ (external sensor) are registered for all three directions once a minute. The remaining time between these measurements the current of the MOT coils is switched on. A direct comparison of the measured magnetic field is difficult because of many sources of fluctuating fields. Especially the noise of the subway generates field fluctuations of about $30\,$mG along the y-direction which exceeds the expected effect of the sensor drift. However, the fields of distant sources are identical for both sensors and the voltage difference $\Delta U^{(i)}(t)$ between the two sensors

$$\Delta U^{(i)}(t) = (U_i^{(i)}(t) - U_{0,i}^{(i)}) - \frac{s_i^{(i)}}{s_e^{(i)}}(U_e^{(i)}(t) - U_{0,e}^{(i)}) \tag{5.5}$$

(with voltages $U_{0,i}^{(i)}$ and $U_{0,e}^{(i)}$ at time $t = 0$ and scaled with individual sensitivities $s_i^{(i)}$ (internal sensor) and $s_e^{(i)}$ (external sensor)) should be constant except for the sensor drifts. Thus, the measured difference of the sensor voltages is equal to the sensor drift of the internal sensor. The result for lab 1 is shown in figure 5.4 and clearly shows deviations for the three directions with the drift along the z-direction being the most dominant one.

The observed behavior of the drift is very reproducible. After the MOT field is switched off

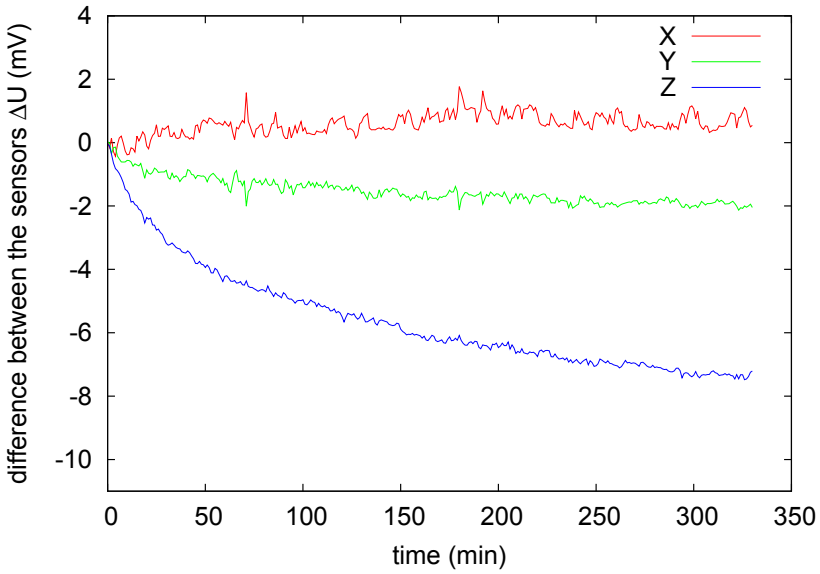

Figure 5.4.: Drifts of the magneto-resistive sensor when the MOT fields are switched on. The plotted data is the difference between the output voltages of the internal and external sensor according to equation 5.5. Before the measurement, the MOT field was kept off for a long time. Drifts are visible for all axes x (red), y (green) and z (blue). All traces are set to 0 at $t = 0$.

for a sufficient amount of time (typical many hours up to one day) the sensor difference has a constant value (which is set to zero). When the field is then switched on the magnetization of the sensor increases and the sensor difference changes by up to several mV (corresponding to magnetic fields of several mG) within the first hour. This drift continues many hours ($> 5\,\mathrm{h}$) until saturation is reached. When the MOT is switched off again, we can observe the inverse procedure, starting with a fast change of the voltage difference followed by a very slow convergence to the initial value. In measurements, the loading rate of the atoms and therefore the ratio of the on and off times of the MOT is not constant. Thus, the magnetization never reaches a saturation but is fluctuating and the feedback stabilization loop sets different magnetic fields varying by a few mG. Moreover, the loading rate in experiments with two atoms strongly differs from that in experiments with one atom (which are used to set the reference voltage of the feedback stabilization). This causes different changes of the output voltage of the internal sensor for the two types of measurements and different reference values would be required to achieve a compensation of the magnetic field. Therefore, it is mandatory to minimize the sensor drifts.

A reduction of this effect turned out to be hard to achieve. The most efficient way found to obtain stable magnetic fields for long times that are required in the experiments, is a regularly performed sensor recalibration based on the comparison of the feedback sensor with the more stable external sensor.

5.1.4. Calibration of the feedback sensor

General procedure

The calibration of the feedback sensor is performed automatically after a certain time in the experimental run, e.g. every 5 minutes. To start the recalibration, the measurements are interrupted and the MOT coils are switched off. The currents in the compensation coils are then switched to defined values which need to be constant over long times such that the calibration is performed always for the same field configuration. This enables us to use the difference signal $\Delta U^{(i)}$ (according to equation 5.5) between both sensors to directly measure drifts of the feedback sensor. Then, the reference voltage of the feedback loop is changed by $U_{ref}^{(i)} \rightarrow U_{ref}^{(i)} + \Delta U^{(i)}$ and the experimental run continues. With the new reference value, the feedback loop will compensate magnetic fields correctly.

Calibration of the sensitivity ratio

This approach requires the determination of the sensitivities of both sensors. While the fluxgate sensor has a certified calibrated sensitivity of $s_e = 10\frac{\mathrm{mV}}{\mathrm{mG}}$ for all axes, this parameter is not known precisely for the feedback sensor. However, we can evaluate the ratio $\frac{s_i}{s_e}$ by comparing the response of both sensors to changes of the magnetic field. Therefore, traces of the output voltages of the sensors are recorded without switching on the MOT coils. Figure 5.5 shows a measured trace of the voltages corresponding to the magnetic field detected by both sensors recorded every 5 seconds for an overall time of about one hour. The differences between two consecutive data points are analyzed and if the change of the output voltage of one channel of the

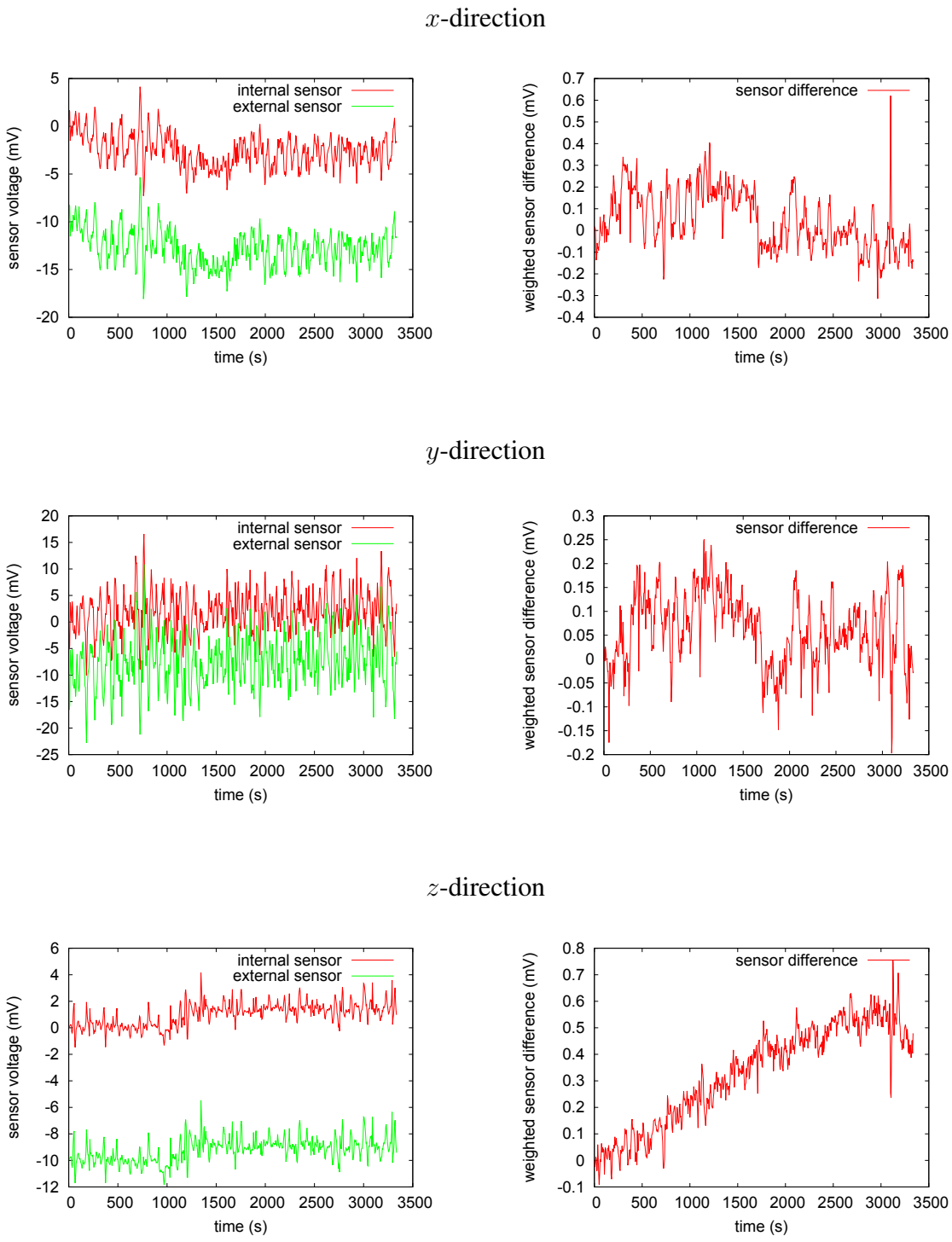

Figure 5.5.: Left: Output voltages of the internal and external (scaled with a factor of 0.1) sensor along three directions (set to 0 and -10 at $t = 0$). Fluctuations of more than $0.5\,\mathrm{mV}$ are associated with a change of the magnetic field. Right: The difference between the sensor voltages weighted with sensitivities $s_i^{(i)}$ and $s_e^{(i)}$ shows only small fluctuations (set to 0 at $t = 0$).

lab 1	$s_i^{(i)}(\frac{\mathrm{mV}}{\mathrm{mG}})$	$\Delta s_i^{(i)}(\frac{\mathrm{mV}}{\mathrm{mG}})$	$s_e^{(i)}(\frac{\mathrm{mV}}{\mathrm{mG}})$	$\frac{s_i^{(i)}}{s_e^{(i)}}$
x	0.937	3.18×10^{-3}	10.0	0.0937
y	0.790	8.64×10^{-5}	-10.0	-0.0790
z	-0.862	6.72×10^{-4}	-10.0	0.0862
lab 2	$s_i^{(i)}(\frac{\mathrm{mV}}{\mathrm{mG}})$	$\Delta s_i^{(i)}(\frac{\mathrm{mV}}{\mathrm{mG}})$	$s_e^{(i)}(\frac{\mathrm{mV}}{\mathrm{mG}})$	$\frac{s_i^{(i)}}{s_e^{(i)}}$
x	-1.162	2.85×10^{-3}	-10.0	0.1162
y	-0.788	3.88×10^{-5}	-10.0	0.0788
z	-0.779	1.98×10^{-4}	10.0	-0.0779

Table 5.1.: Sensitivities of the magnetic field sensors in the two trap setups. The values are obtained by comparing field fluctuations measured by the internal and external sensor shown in figure 5.5.

internal sensor exceeds $0.5\,\mathrm{mV}$ this change is associated with a fluctuation of the magnetic field (smaller variations could also originate from electronic noise). For every occurrence exceeding this threshold we calculate the ratio of the change of the output voltages between both sensors and their averaged ratio provides the final sensitivity ratio. The difference signal $\Delta U^{(i)}$ for all directions is also shown in figure 5.5 where the evaluated sensitivities of table 5.1 are used. The (magnetic) fluctuations of the single traces are almost completely suppressed.

Temperature correction

While fluctuating magnetic fields generated by distant sources can be suppressed by the comparison of the sensors with constant sensitivity ratios, sources close to the setup generate a different magnetic field at the two sensors and fluctuations of these fields will lead to different changes in the sensor output. The strongest magnetic component in the environment of the trap is the magnet of the ion-getter pump. The magnetic field generated by this magnet changes with its temperature. Figure 5.6 shows the correlation between the difference signal of the sensors and the temperature (magenta curve) that is measured with a thermistor on top of the magnet. To vary the temperature, we switched on and off the air conditioning in the laboratory. Because of the gradient of the magnetic field between the positions of the sensors, their difference signal changes. In the automatically performed recalibration, such changes due to the temperature change would be misinterpreted as a drift of the feedback sensor. To avoid this, the calculation of the sensor drift in equation 5.5 is extended with a temperature dependent correction. Figure 5.6 a) reveals a change of the difference signal by $s_T^{(x)} = 0.8\,\frac{\mathrm{mV}}{\mathrm{K}}$, $s_T^{(y)} = -4.0\,\frac{\mathrm{mV}}{\mathrm{K}}$ and $s_T^{(z)} = -4.0\,\frac{\mathrm{mV}}{\mathrm{K}}$ for the directions x (red), y (green) and z (blue), respectively. The recalibration is then executed according to the calculated sensor drift

$$\Delta U^{(i)}(t) = (U_i^{(i)}(t) - U_{0,i}^{(i)}) - \frac{s_i^{(i)}}{s_e^{(i)}}(U_e^{(i)}(t) - U_{0,e}^{(i)}) - s_T^{(i)}(T(t) - T_0), \tag{5.6}$$

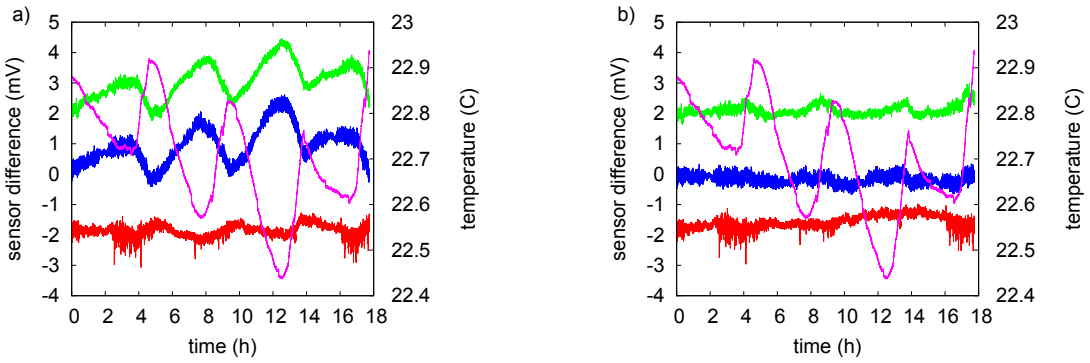

Figure 5.6.: Temperature correction for the sensor recalibration. Shown are the differences between the sensor voltages ΔU (for the directions x (red), y (green) and z (blue)) for fluctuating temperatures of the magnet of the ion getter pump. The temperature varies (magenta) by about $0.5\,\mathrm{K}$. a) Sensor differences according to equation 5.5 show fluctuations depending on the temperature. b) Fluctuations can be suppressed with additional temperature correction (equation 5.6).

with the temperature of the ion-getter pump $T(t)$ and its initial value T_0. The corrected data, shown in figure 5.6 b), has a stability of $0.5\,\mathrm{mV}$ for temperature variations of $0.5\,\mathrm{K}$. We measured the temperature at different positions in the setup and the temperature of the ion-getter pump has the highest correlations to the observed changes. However, the corrected data is not perfectly flat. The remaining smaller fluctuations can be caused by further components in the setup and additional temperature corrections would be needed to suppress them. The reached stability of the difference signal is sufficient for our purpose, especially because the setup is temperature stabilized with an accuracy of $0.1\,\mathrm{K}$ [45] and expected temperature fluctuations during an experimental run are expected to be much smaller than the ones in figure 5.6.

5.1.5. Preventing errors in the calibration program

The calibration of the feedback sensor, i.e. the comparison of the two magnetic field sensors and the correction of the reference voltage of the feedback loop according to equation 5.6, is done automatically in experiments (usually every 5 minutes). However, there is a variety of possible errors during the calibration that are taken into account in the automatic control program.

- The comparison of the sensors is done by registering their output voltages within $20\,\mathrm{ms}$. If there is strong electronic noise or the magnetic field is fluctuating during this time the result will be slightly influenced. To increase the accuracy of the calibration, the program averages 20 subsequently measured difference signals and only uses the result if the standard deviation is below $0.1\,\mathrm{mV}$. Otherwise the recalibration is repeated.

- Before every calibration the feedback sensor is reset by applying a current that saturates

the sensor [41]. In most cases, this leads to a stable output voltage of the sensor, but in rare cases after the reset, the output voltage of the sensor is still saturated. This would result in a strong deviation of the sensor difference. To avoid any influence of this behavior on the calibration of the sensor, we only allow changes of the sensor difference of a few mV between two calibrations. This is useful, because the sensor drift only changes slightly in a couple of minutes and larger deviations are most likely caused by such electronic features.

- The output voltages of the magnetic field sensors and the resistance (converted into a voltage) of the thermistor are registered by a voltmeter and imported by the control PC. In some cases the imported string has errors leading to wrong calculations of the sensor drift. Thus, the string is checked for regular expressions and the read-in procedure can be repeated if necessary.

- If the mechanical setup around the trap changes, e.g (slightly) magnetic components are moved or added, this can change the magnetic field configuration. In this case, a new initialization of the reference voltages might be necessary. The new values are obtained by time resolved measurements and a minimization of Larmor precession (see section 5.1.2).

5.1.6. AC-Stark effect in the dipole trap

The light of the optical dipole trap (ODT) causes (like magnetic fields) a state-dependent shift of the Zeeman states that leads to a time evolution of the states. The reason for this is the AC-Stark effect for atoms in intense electric fields. The intensity profile $I(\vec{x})$ of the dipole trap beam in the focal region is approximately a Gaussian beam providing a maximal intensity of $I_0 = \frac{2P}{\pi w_0^2}$ (with P being the optical power of the beam and w_0 is the Gaussian waist at the focus). The shift of the Zeeman states for the ground level $F = 1$ corresponds to the trapping potential of the dipole trap $\Delta E_{m_F}(\vec{x}) = U_{\mathrm{dip}}(\vec{x})$ and is calculated [54, 71] as

$$\Delta E_{m_F}(\vec{x}) \;=\; -\frac{\pi c^2}{2}\frac{\Gamma}{\omega_0^3}\left(\frac{1-\mathfrak{P}g_F m_F}{\Delta_{1,F}}+\frac{2+\mathfrak{P}g_F m_F}{\Delta_{2,F}}\right) I(\vec{x}), \tag{5.7}$$

with the decay rate Γ and the frequency ω_0 of the atomic transition, the detuning $\Delta_{1,F}$ and $\Delta_{2,F}$ of the light frequency to the atomic transition frequencies of the D_1 and D_2 line and $\mathfrak{P} \in [-1, 1]$ which characterizes the light polarization. For linear polarization of the dipole trap beam, $\mathfrak{P}$ has a value of 0, whereas for circular polarization it has a value of ± 1 (for $\sigma^{\pm}$). In the general case of an elliptical polarization, $\mathfrak{P}$ depends on the ellipticity ϵ according to $\mathfrak{P} = \pm\sqrt{1-\epsilon^2}$ where the "$+$" corresponds to right and the "$-$" to left handed elliptical polarization. For an electric field where the main axis of the elliptical polarization is along the x-axis, the ellipticity is determined by the light polarization vector [71] (Jones vector)

$$\vec{E} = \begin{pmatrix} E_x \\ E_y \\ 0 \end{pmatrix} = \frac{E_0}{\sqrt{2}}\left(\sqrt{1+\epsilon}\,\hat{x} + i\sqrt{1-\epsilon}\,\hat{y}\right), \tag{5.8}$$

and has a value of

$$\epsilon = \frac{|E_x|^2 - |E_y|^2}{|E_x|^2 + |E_y|^2}. \tag{5.9}$$

For linearly polarized light all Zeeman states are shifted by the same energy

$$\Delta E_{lin}(\vec{x}) = -\frac{\pi c^2}{2}\frac{\Gamma}{\omega_0^3}\left(\frac{1}{\Delta_{1,F}} + \frac{2}{\Delta_{2,F}}\right) I(\vec{x}). \tag{5.10}$$

In this case, no time evolution of the states occurs. We define $U_m(\vec{x}) := \Delta E_{lin}(\vec{x})$ as the mean trapping potential for the three Zeeman states of the $F = 1$ ground level. The trap depth is then defined as $U_{m,0} := U_m(\vec{0})$.

In the case of elliptical polarization, the states have different shifts $\Delta E_{m_F}(\vec{x})$. Since only the state dependent shift leads to a time evolution, we subtract the constant terms in equation 5.7 and get an expression for the relative shift $\Delta E_{rel}(\vec{x})$ between different Zeeman states of

$$\Delta E_{rel}(\vec{x}) = \frac{\pi c^2}{2}\frac{\Gamma}{\omega_0^3}\left(\frac{1}{\Delta_{1,F}} - \frac{1}{\Delta_{2,F}}\right)\mathfrak{P} g_F m_F I(\vec{x}). \tag{5.11}$$

For calculating this relative shift we define the constant R_{circ} as

$$R_{\mathrm{circ}} := -\frac{\frac{1}{\Delta_{1,F}} - \frac{1}{\Delta_{2,F}}}{\frac{1}{\Delta_{1,F}} + \frac{2}{\Delta_{2,F}}}, \tag{5.12}$$

and divide the relative shift by the linear shift

$$\frac{\Delta E_{rel}(\vec{x})}{\Delta E_{lin}(\vec{x})} = R_{\mathrm{circ}} g_F m_F \mathfrak{P}. \tag{5.13}$$

Rearranging the terms leads to

$$\begin{aligned}\Delta E_{rel}(\vec{x}) &= R_{\mathrm{circ}} g_F m_F \mathfrak{P}\, \Delta E_{lin}(\vec{x}) \\ &= R_{\mathrm{circ}} g_F m_F \mathfrak{P}\, U_m(\vec{x}).\end{aligned} \tag{5.14}$$

This shift is similar to a Zeeman shift induced by a magnetic field in the z-direction $\Delta E_{Zeeman} = \mu_B g_F m_F B_z$. Therefore, we can find a combined expression for an atom stored in an optical dipole trap and exposed to ambient magnetic fields by adding the corresponding shifts for the z-direction to ΔE:

$$\begin{aligned}\Delta E &= \Delta E_{Zeeman} + \Delta E_{rel}(\vec{x}) \\ &= \mu_B g_F m_F B_z + R_{\text{circ}} g_F m_F \mathfrak{P}\, U_m(\vec{x}) \\ &= \mu_B g_F m_F \left(B_z + \frac{1}{\mu_B} R_{\text{circ}} \mathfrak{P}\, U_m(\vec{x}) \right) \\ &= \mu_B g_F m_F B_{z,eff}, \end{aligned} \tag{5.15}$$

which allows to introduce an effective magnetic field in z-direction $B_{z,eff}$ including the effect of the dipole trap laser. The overall effective magnetic field can then be written as

$$\vec{B}_{eff}(\vec{x}) = \vec{B} + \frac{1}{\mu_B} R_{\text{circ}} \mathfrak{P}\, U_m(\vec{x})\, \vec{e}_z, \tag{5.16}$$

which is position dependent due to the Gaussian intensity profile of the dipole trap beam.

To avoid time evolution of atomic states, the light of the dipole trap laser thus has to be linearly polarized. In our setup, the polarization is set by a polarizer in the confocal microscope before the dichroic mirror that directs the dipole trap beam to the objective (see figure 2.2). Consequently, the linearly polarized light passes several optical components and, as a result, is affected by their birefringence. The procedure to achieve linear polarization at the position of the atom trap thus is a non-trivial task. However, it is possible to find certain angles of the polarization that are close to the axis of the birefringent components at which the change of the polarization is small. To find these angles, we follow the following procedure.

First, magnetic x- and y-fields are minimized such that the resulting atomic state evolution is dominated either by a magnetic z-field or the elliptical polarization of the dipole trap beam. To distinguish between these reasons we perform 2 time resolved measurements, one with the working depth of the ODT and the second one with a reduced depth (typically by a factor of 2) during the time delay. While the trap depth has no influence on the time evolution due to magnetic fields, the Larmor frequency caused by the ODT is reduced. We then find magnetic z-fields (or reference voltages U_{ref} for the compensation procedure) that minimize the observed Larmor frequency for both cases ($U_{ref,1}$ and $U_{ref,\frac{1}{2}}$ for full or half depth). In both cases the applied magnetic field compensates the optically induced one. This allows us now to minimize the magnetic field in the z-direction by setting the reference voltage to $U_{ref} = U_{ref,1} - 2(U_{ref,1} - U_{ref,\frac{1}{2}})$. When the magnetic field is eliminated, the polarization of the dipole trap beam can be adjusted by changing the angle of the polarizer (to achieve linear polarization) until almost no residual Larmor precession is observed. Even after this adjustment there are small residual circular components in the light polarization that have to be compensated by a magnetic z-field. This compensation works as long as the remaining AC-Stark shift is small (equivalent to a few mG), otherwise the inhomogeneous intensity of the laser beam in which the atom is moving and the homogeneous external magnetic field cannot fully compensate each other.

The high sensitivity obviously requires the polarization of the ODT to be as stable as possible. However, the polarization drifts over time mainly due to a varying birefringence of optical components (dichroic mirror, objective and glass of the vacuum cell), that is especially affected

by temperature changes. Despite an active temperature stabilization of the experimental environment with an accuracy of about $0.1\,\mathrm{K}$ [45], this effect still limits the temporal stability of the experiment. During some experimental runs, drifts of the polarization of the dipole trap beam could be observed that are equivalent to about $1 - 4\,\mathrm{mG}$ (within 1 day). Further improvements of the stability by using temperature stabilized MOT coils (to avoid heating of birefringent components) or a monitoring of the polarization of the ODT that might allow an active stabilization are still in progress.

5.1.7. Long-term stability

There are two major requirements on the stabilization of the Zeeman and AC-Stark shift in order to be able to perform long-distance atom-atom entanglement experiments. First, the atomic state on each side has to be preserved with a high fidelity until the state measurement is performed. The total effective magnetic field therefore needs to be stabilized to less than $1.6\,\mathrm{mG}$ which is fulfilled with the feedback stabilization scheme. Second, we aim at a long-term stability of this field compensation, because the manual adjustment of the magnetic field feedback loop (as explained in section 5.1.2) by time resolved measurements is time consuming (usually it takes a few hours) and should not be repeated more often than one time a day. To measure the stability of magnetic fields, changes of the states $|\Psi_H\rangle$ and $|\Psi_V\rangle$ due to the evolution are measured after a certain delay (figure 5.7 a)). This measurement is similar to the one shown in figure 5.3 which allows us to compare the stability of the improved stabilization method (including the calibration of the sensor) with an older measurement. The delay in this measurement is increased to $55\,\mu s$ to get more sensitive to magnetic field effects (the measurement shown in figure 5.3 was performed at a time delay of $21\,\mu\mathrm{s}$).

The measurement shows the probability for detecting the atoms in the state $|\Psi_V\rangle$ and each data point is measured for 15 minutes. Additionally, before a data point is measured the magnetic field sensor is recalibrated and the corresponding difference signal of the magnetic field sensors and the temperature (measured at the ion-getter pump) are plotted in figure 5.7 b). During the first $80\,\mathrm{h}$ of measurement time, the analyzed atomic states are very stable although the feedback sensor drifts by about $10\,\mathrm{mV}$ (z-axis). Some smaller changes of the observed states correspond to a magnetic field of less than $1.6\,\mathrm{mG}$ and are therefore within the required stability. Hence, long-term stabilization of magnetic fields is indeed possible by applying the improved compensation scheme based on the recalibration of the feedback sensor. After about 76 hours the air conditioning was switched off to check the influence of a changing temperature. At this time, a change of the prepared states is visible caused by an effective magnetic field. Since the comparison of the magnetic field sensors shows no distinctive features, we assume that the reduction of the contrast is caused by a change of the polarization of the dipole trap beam (due to a changing birefringence of optical components).

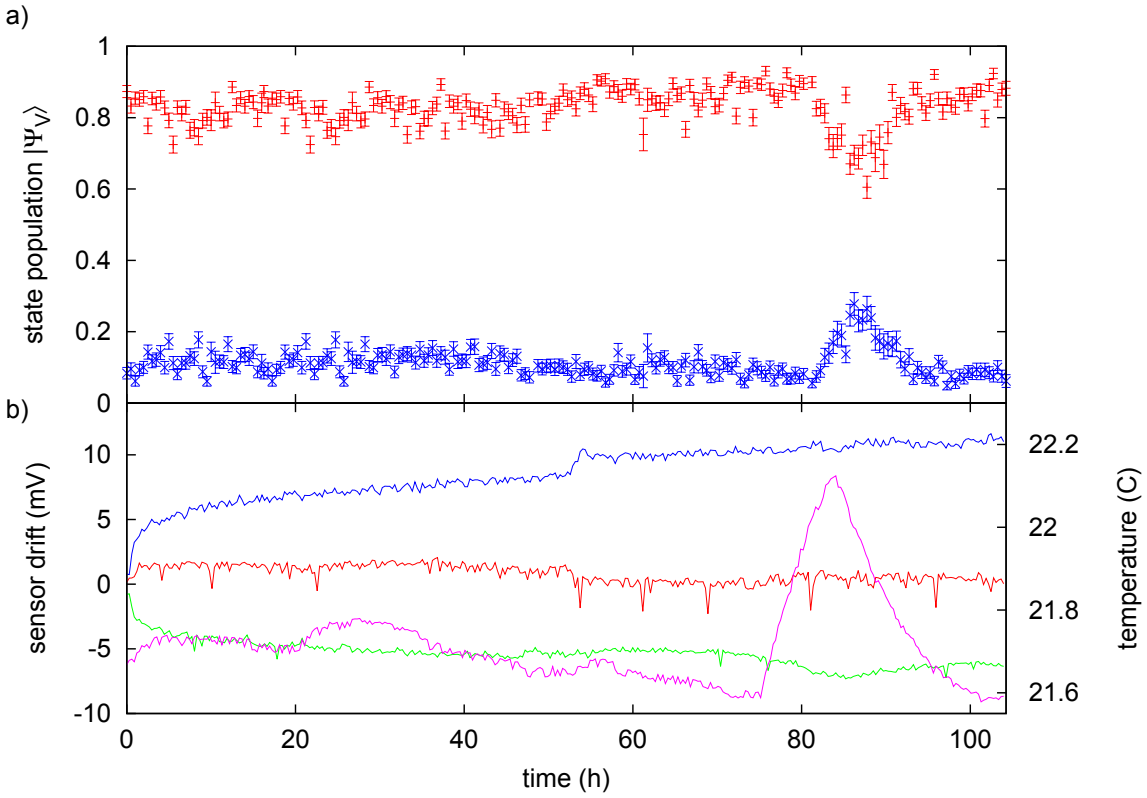

Figure 5.7.: a) Stability of the prepared atomic states $|\Psi_H\rangle$ (blue) and $|\Psi_V\rangle$ (red), measured at a time delay of $55\,\mu$s over 104 hours. After $76\,$h the temperature stabilization of the air condition was switched off. b) Recorded voltage difference between the magnetic field sensors along the x- (red), y- (green), and z-direction (blue) during the calibration procedure. Additionally, the temperature (magenta) measured at the ion-getter pump is shown.

5.2. Effects of strong focusing and oscillation of the atoms in the dipole trap

So far, I analyzed the time evolution of atomic states in the presence of ambient magnetic fields and elliptical polarization in the light of the optical dipole trap. Besides this case, inevitable elliptical polarization also arises due to the focusing of the ODT beam. As will be shown, this results in another effect leading to a time evolution of atomic states and, in combination with the motion of the trapped atoms, to a strong dephasing that was also observed in other experiments [72].

5.2.1. Polarization of the dipole trap beam around the focus

The optical dipole trap is created by a Gaussian laser beam that is tightly focused by an objective. Even if the initial polarization is perfectly linear, the electric field vector in the focal region also has longitudinal components. A mathematical description of this effect is given in [73, 74]. There, an analysis of the electric field in the image region of a lens is done that allows to calculate the polarization at each point. The calculation is not restricted to optical systems with low aperture and therefore allows us to use this analysis for our setup. A modification to calculate the polarization for a focused Gaussian beam that is used here is given in [41]. There it is shown that the polarization in the focal area is elliptical with one component in the plane perpendicular to the optical axis and one component along the propagation direction. The electric field amplitudes (E_x, E_y, E_z) for each point in the focal area in cylindrical coordinates (r, ϕ, z) with the origin at the focus is given by

$$\begin{aligned} E_x(r,\phi,z) &= E_0\left(F_0(r,z) + F_2(r,z)\cos(2\phi)\right), \\ E_y(r,\phi,z) &= E_0 F_2(r,z)\sin(2\phi), \\ E_z(r,\phi,z) &= E_0 2iF_1(r,z)\cos(\phi), \end{aligned} \tag{5.17}$$

with $\phi = 0$ corresponding to the x-axis which is the polarization direction of the incident wave (propagating along z) and the integrals $F_i(r,z)$ being defined as

$$\begin{aligned} F_0(r,z) &= \int_0^\alpha d\theta\, \exp\left(-\frac{f^2\tan(\theta)^2}{w^2}\right)\sqrt{\cos(\theta)}\,(1+\cos(\theta))\,J_0\left(kr\sin(\theta)\right)e^{ikz\cos(\theta)}\sin(\theta), \\ F_1(r,z) &= \int_0^\alpha d\theta\, \exp\left(-\frac{f^2\tan(\theta)^2}{w^2}\right)\sqrt{\cos(\theta)}\sin(\theta)J_1\left(kr\sin(\theta)\right)e^{ikz\cos(\theta)}\sin(\theta), \\ F_2(r,z) &= \int_0^\alpha d\theta\, \exp\left(-\frac{f^2\tan(\theta)^2}{w^2}\right)\sqrt{\cos(\theta)}\,(1-\cos(\theta))\,J_2\left(kr\sin(\theta)\right)e^{ikz\cos(\theta)}\sin(\theta), \end{aligned} \tag{5.18}$$

with the Bessel functions $J_{0,1,2}$, the focal length f of the objective, and the Gaussian radius w of the beam entering the microscope. The integration is done up to the opening angle α given by the numerical aperture of the objective. To simplify calculations, the integrals have approximate solutions [41]

$$\begin{aligned} F_0(r,z) &\backsimeq F_0(0,0)\frac{1}{\sqrt{1+\frac{z^2}{z_R^2}}}\exp\left(-\frac{r^2}{w_0^2\left(1+\frac{z^2}{z_R^2}\right)}\right), \\ F_1(r,z) &\backsimeq F_0(0,0)\frac{1}{2z_R}\frac{1}{1+\frac{z^2}{z_R^2}}\exp\left(-\frac{r^2}{w_0^2\left(1+\frac{z^2}{z_R^2}\right)}\right), \\ F_2(r,z) &\backsimeq F_0(0,0)\frac{1}{4z_R^2}\frac{1}{\left(1+\frac{z^2}{z_R^2}\right)^{\frac{3}{2}}}\exp\left(-\frac{r^2}{w_0^2\left(1+\frac{z^2}{z_R^2}\right)}\right), \end{aligned} \tag{5.19}$$

with the Rayleigh length z_R and the waist w_0. The value of $F_0(0,0)$ is calculated by

$$F_0(0,0) = \int_0^\alpha d\theta\, \exp\left(-\frac{f^2\tan(\theta)^2}{w^2}\right)\sqrt{\cos(\theta)}\,(1+\cos(\theta))\sin(\theta). \tag{5.20}$$

This allows us to calculate the electric field distribution of a tightly focused dipole trap beam that is linearly polarized in the x-direction before the objective. The intensity profile of the transversal $|E_x|^2$ and longitudinal $|E_z|^2$ components in the x-z-plane are evaluated with Mathematica and plotted in figure 5.8. The transversal component has a distribution similar to that expected for a Gaussian beam, whereas the longitudinal component is strongest at a certain distance from the focus along the x-axis. Note that according to equation 5.17 the longitudinal components E_z have a $\frac{\pi}{2}$-phase relative to the transversal polarization and therefore the resulting polarization is elliptical. Furthermore, the sign of E_z changes at $\phi = \frac{\pi}{2}, \frac{3\pi}{2}$ which leads to different directions of the rotation (clockwise and counter-clockwise) at different sides of the y-z-plane. The elliptically polarized light field causes a state-dependent and position-dependent AC-Stark shift and dephasing of the atomic states.

5.2.2. Time evolution of states for an atom in the field of the ODT

For calculating the resulting AC-Stark shift for atoms in this field, we use equation 5.14 with the difference that the states $|m'_F\rangle$ are here eigenstates to the $\hat{F}_y$ angular momentum operator [41]. Therefore, the AC-Stark shift is no longer equivalent to the shift of a magnetic z-field, but to that of a field in the y-direction. The effective magnetic field of this effect (caused by the longitudinal polarization components) is calculated analog to equation 5.16 as

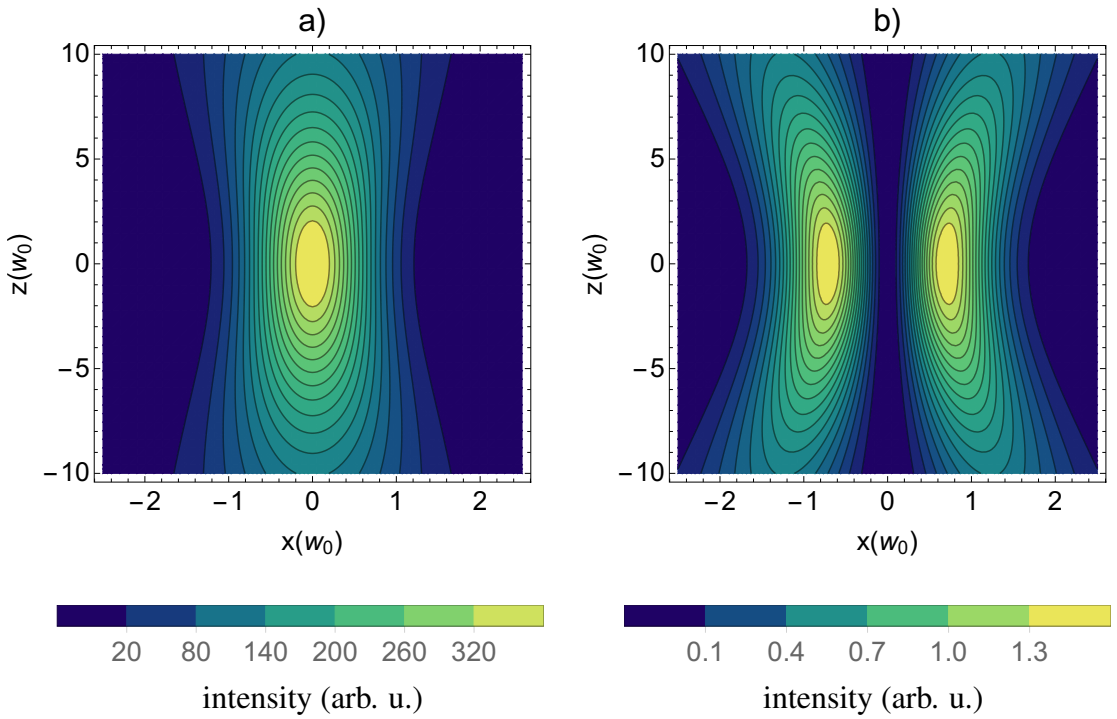

Figure 5.8.: Intensity profile in the focal region of the ODT beam (for $y = 0$). a) Transversal component $|E_x|^2$. b) Longitudinal component $|E_z|^2$.

$$B_{long}(\vec{x}) \;=\; \underbrace{\frac{R_{\text{circ}}}{\mu_B}\,\text{sgn}(x)}_{(=\pm 1)} \sqrt{1 - \underbrace{\left(\frac{|E_x(\vec{x})|^2 - |E_z(\vec{x})|^2}{|E_x(\vec{x})|^2 + |E_z(\vec{x})|^2}\right)^2}_{(=\sqrt{1-\epsilon^2})}}\, U_m(\vec{x}), \tag{5.21}$$

with electric field components $E_x(\vec{x})$ and $E_z(\vec{x})$ (equation 5.17, $E_y(\vec{x})$ is neglected) and $U_m(\vec{x})$ and R_{circ} as defined in section 5.1.6. $B_{long}(\vec{x})$ can thus be added to the y-component of the overall effective magnetic field according to

$$\vec{B}_{eff}(\vec{x}) \;=\; \vec{B} + B_{long}(\vec{x})\,\vec{e}_y. \tag{5.22}$$

The strength of this effective field strongly depends on the position of the atom and is zero in the y-z-plane. The thermal motion of an atom in the trap leads to random trajectories that traverse regions of high field strength. Since every atom has a different position and velocity at the time it emits a photon, the time evolution for every measured atomic state is different. Averaged over many trajectories, the population of atoms prepared in the state $|\Psi_H\rangle = \frac{1}{\sqrt{2}}\left(|1,+1\rangle_z + |1,-1\rangle_z\right)$ will decrease at a short time scale due to dephasing in the effective magnetic field. Atoms prepared in the state $|\Psi_V\rangle = \frac{i}{\sqrt{2}}\left(|1,+1\rangle_z - |1,-1\rangle_z\right)$ are not affected by the effective y-field (see

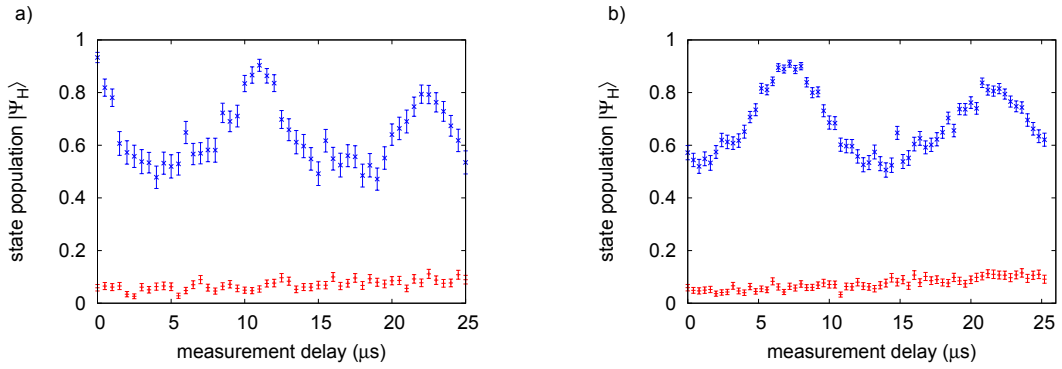

Figure 5.9.: Time evolution of atomic states for a) local measurements of trap 1 and b) remote measurements of trap 2 due to the motion in the effective magnetic field B_{long} of the optical dipole trap laser. The state population of the state $|\Psi_H\rangle$ (blue) changes in the effective magnetic y-field whereas the state $|\Psi_V\rangle$ (red) remains constant. After one oscillation period the initial atomic state is restored due to rephasing. For remote measurements with a minimal time delay of $7.3\,\mu$s an instant state measurement would lead to a low fidelity of this state and measurements are only possible after the first oscillation period.

section 5.1.1). The individual time evolution for each atomic trajectory does not allow a compensation by e.g. magnetic fields and therefore cannot be avoided.

The effective magnetic field is antisymmetric to the z-axis. Considering only motion in the transversal plane (x-y), atoms propagating in the trap have trajectories that are symmetric to the z-axis. The accumulated phase of an atomic state on one side of the y-z-plane is thus equal to the accumulated phase on the other side (but with opposite sign). Therefore, after one full (transversal) oscillation period, the atomic state rephases for every possible trajectory and measurements without loss of fidelity are possible. This behavior is shown in time resolved measurements (figure 5.9 a)). For short time delays of the measurement, the effective magnetic field leads to dephasing of the atomic state and (averaged over many measurements) the state population of atoms prepared in $|\Psi_H\rangle$ decreases to about 0.5. For a time delay of about $11\,\mu$s, which corresponds to one oscillation period, the initial atomic state is restored. The probability to detect the atom in the state $|\Psi_H\rangle$ at this time delay is almost identical to the initial value without delay. For further increased time delays we observe dephasing again and after another oscillation period rephasing of the atomic states, although the probability to detect the atom in the initial state is reduced. The reason is that perfect rephasing only happens as long as we can assume that the atomic motion is only in a transversal plane. This is justified for the time needed for one oscillation, because the transverse trap frequency is much faster than the longitudinal frequency. The waist of the dipole trap is $w_0 = 1.92\,\mu$m corresponding to a Rayleigh length of $z_R = 13.59\,\mu$m. The transverse oscillation period for a trap depth of $U_0/k_B = 3.206\,$mK is then $T_T = \frac{2\pi}{\omega_T} = 2\pi w_0\sqrt{\frac{m}{4U_0}} = 10.9\,\mu$s whereas the longitudinal oscillation period is $T_L = \frac{2\pi}{\omega_L} = 2\pi z_R\sqrt{\frac{m}{2U_0}} = 108.9\,\mu$s. The rephasing

is therefore not perfect and the fidelity decreases with increasing number of oscillation periods. Figure 5.9 b) shows the same measurement for trap 2 that is controlled remotely from lab 1. The photon and signal transmission times needed before the state measurement is performed mean that even for a time delay of 0 the atom has already moved for about $7.3\,\mu$s (see section 4.2) and the atomic state $|\Psi_H\rangle$ is already dephased. The state measurement therefore only gives good results after the first oscillation period. For the trap 2 setup the transverse oscillation period is set to $T_T = 14.5\,\mu$s (which is chosen such that the measurements on both sides are synchronized which will be explained in chapter 6). Thus the measurements have to be performed $14.5\,\mu$s after the excitation or in the context of time resolved measurements, $7.2\,\mu$s after the local CU in lab 2 initiated the state analysis (which corresponds to a time delay of 0 in the measurement).

5.2.3. Simulation of atomic oscillations

The dephasing of atomic states due to this effect sets strict requirements for the atomic state measurements. The properties of this effect are thus investigated in more detail using simulations of the motion of atoms in the effective magnetic field. According to the specific trap configuration, a large number (typical $10,000$) of trajectories of atoms are calculated with random initial conditions according to a thermal distribution of atoms in a harmonic oscillator. In detail, the initial position and initial velocity correspond to the position and velocity of the atom when it emits a photon. The initial position is determined by

$$\begin{aligned} x_0 &= A_x \sin(\varphi_x), \\ y_0 &= A_y \sin(\varphi_y), \\ z_0 &= A_z \sin(\varphi_z), \end{aligned}$$

independently for the three directions, where φ_i is a uniformly distributed random phase in the range of $0..2\pi$ and A_i is a random amplitude according to the energy of a one dimensional Boltzmann distribution

$$p(E) = \frac{1}{k_B T} \exp\left(-\frac{E}{k_B T}\right), \tag{5.23}$$

with the atomic temperature T, where the amplitude A is related to the total energy E of the oscillator by $E = \frac{1}{2} m\omega^2 A^2$ with mass m and frequency ω. We use the inversion method to calculate the distribution of A from uniformly distributed random numbers $rand \in [0, 1]$. The cumulative distribution function of equation 5.23 is

$$\begin{aligned} F(E) &= \frac{1}{k_B T} \int_0^E \exp\left(-\frac{E'}{k_B T}\right) dE' \\ &= 1 - \exp\left(-\frac{E}{k_B T}\right), \end{aligned} \tag{5.24}$$

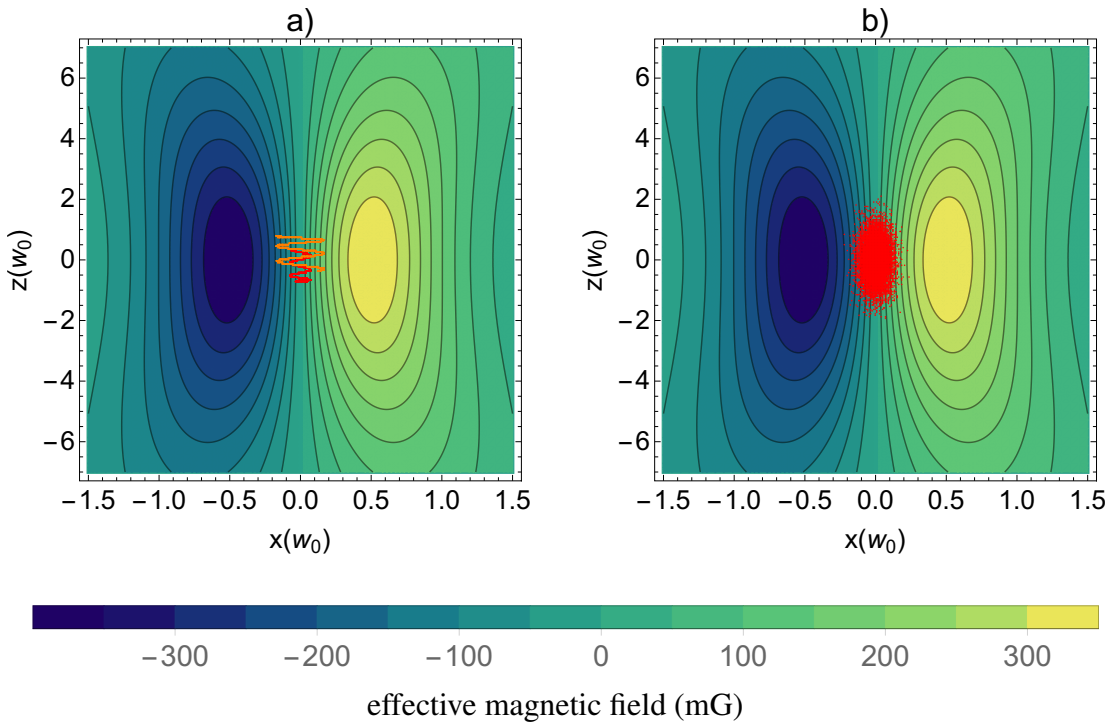

Figure 5.10.: Randomly calculated atomic trajectories (a) and positions (b) according to a thermal distribution, projected on the x-z-plane. The penetration depth into regions with an effective magnetic field $B_{long}(\vec{x})$ is shown. The sign of $B_{long}(\vec{x})$ changes at $x = 0$.

and an inversion results in $E = F^{-1}(rand)$. With $E = \frac{1}{2}m\omega^2 A^2$ we can calculate random amplitudes according to

$$A_i = \sqrt{-\frac{2k_B T}{m\omega_i^2}\ln(1 - rand)} \tag{5.25}$$

for all three directions. Similarly to the initial position, the initial velocities are calculated by

$$\begin{aligned} v_{x0} &= A_x\omega_r \cos(\varphi_x), \\ v_{y0} &= A_y\omega_r \cos(\varphi_y), \\ v_{z0} &= A_z\omega_z \cos(\varphi_z), \end{aligned}$$

with radial oscillation frequency ω_r and longitudinal trap frequency ω_z.

The trajectory of the atom is then calculated for a large number (typical 2000) of time points up to a final time. Two selected trajectories (a) and a large number of random start positions (b) are shown in figure 5.10 (projected onto the x-z-plane) together with the effective magnetic

field $B_{long}(\vec{x})$ of the dipole trap laser. Although the average amplitude does not reach the area of maximal field strength, the effective field is still strong enough to cause a fast state evolution.

For each time step the change of the atomic state is calculated according to the local field of the dipole trap and the magnetic fields. The effective magnetic field caused by elliptical polarization of the initial dipole trap beam is added to the magnetic field in the z-direction and the field caused by the elliptical polarization around the focal spot to the magnetic field in the y-direction. The program finally evaluates an averaged projection for all trajectories onto a selected atomic state. Thus the result of the simulation corresponds to the results obtained in measurements.

With this tool, experiments and time resolved measurements can be compared with the results of the simulation. The simulation for specific parameters takes about $1-2$ minutes which is too long to fit the curves to the measured data and a manual adjustment of the simulation parameters is performed. The simulation takes into account the following parameters:

- the trap geometry, in particular the waist of the dipole trap beam and the Rayleigh-length. These parameters are obtained from knife-edge measurements [45]. The simulation assumes perfect Gaussian shape of the beam, beyond that it can also include asymmetry (e.g. arising from aberrations). To account for this in the simulations we introduced an asymmetry factor a_{sym} that will be discussed in section 5.2.4.

- the trap depth $U_{m,0}$ affects the trap oscillation period. It is therefore used to tune the rephasing time, i.e. the time after which measurements of the atomic states are possible with minimal loss of fidelity. The dependence of the (transversal) oscillation period on the trap depth is $T_T \sim \frac{1}{\sqrt{U_{m,0}}} \sim \frac{1}{\sqrt{P_0}}$, with P_0 being the total power of the laser beam.

- the temperature T of the atoms is used for calculating random initial positions and velocities according to a thermal distribution. Typical temperatures in the experiment are in the range of $10..100\mu\mathrm{K}$. Simulating time evolutions for different temperatures as done in figure 5.14 reveals that the fidelity after one oscillation period depends on the temperature and the loss of fidelity is small only for $T \lesssim 60\mu\mathrm{K}$.

- magnetic fields in all three directions x, y and z.

- initial elliptical polarization of the ODT beam (without focusing).

- the fidelity of the state measurement (measured without time delay) is used to scale the simulated state evolution. However, there is always a minimal time delay of about $450\,\mathrm{ns}$ before the atomic state is measured (due to switching times to the state analysis) and the states can already be slightly dephased. To avoid this the value for the fidelity is obtained from measurements in the basis that is not influenced by dephasing due to trap oscillations.

By adjusting the free parameters, we "fit" the simulation to the experimental data. Figure 5.11 shows a good agreement of the time evolution of the atomic states. Although the curve is fitted to the data "by hand", all parameters have quite specific influences on the result and therefore a good agreement is only achieved for a particular set of parameters. For the measurement in figure 5.11 these are summarized in table 5.2.

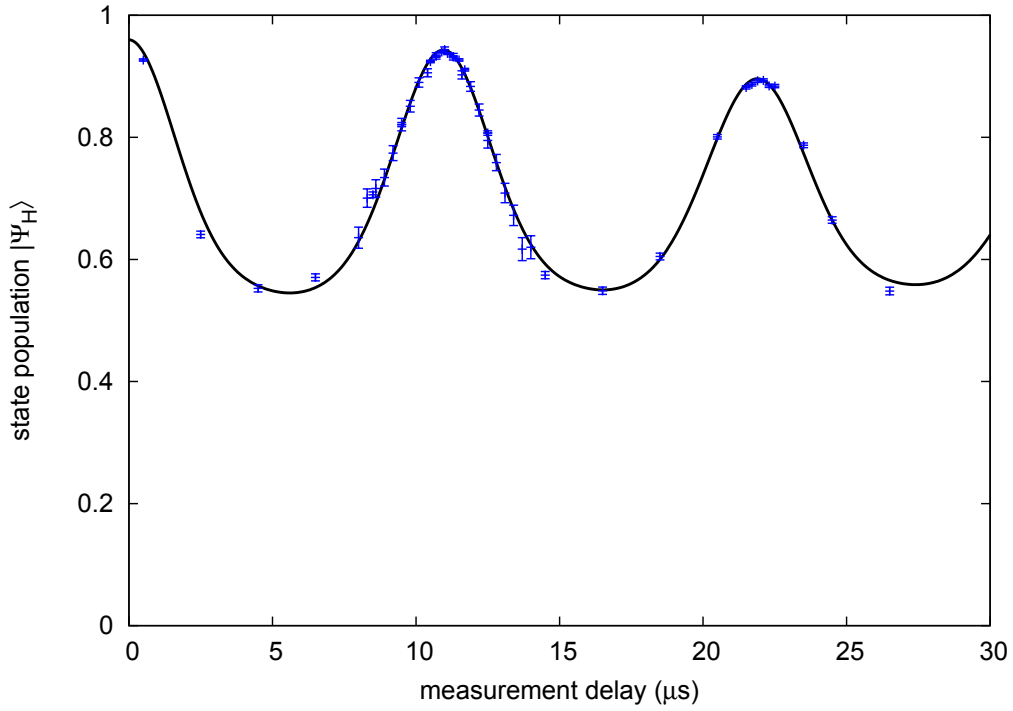

Figure 5.11.: Comparison of the measured (blue) and simulated (black) time evolution of the atomic state $|\Psi_H\rangle$ (projected on $|\Psi_H\rangle$).

$U_{m,0}$	w_0	a_{sym}	T	$\lvert\vec{B}\rvert$
$k_B \cdot 3.206\,\mathrm{mK}$	$1.92\,\mu\mathrm{m}$	0.08	$45\,\mu\mathrm{K}$	$< 0.3\,\mathrm{mG}$

Table 5.2.: Parameters that reproduce best the observed time dependence of the state population of figure 5.11.

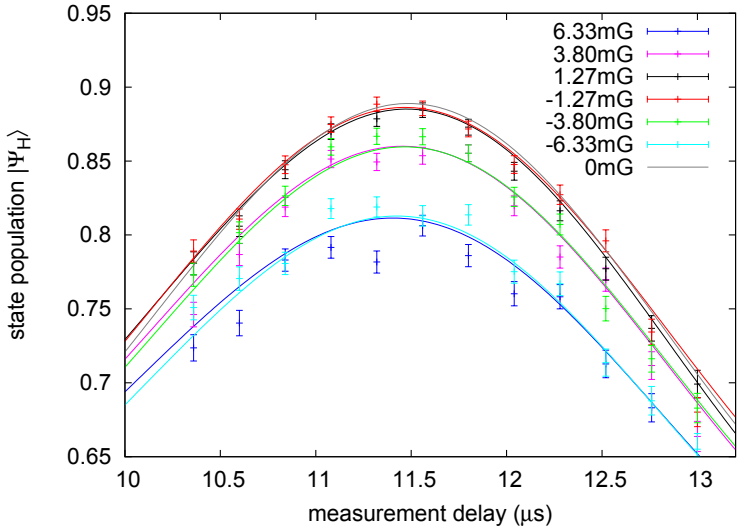

Figure 5.12.: Dependence of the rephasing on magnetic fields in the y-direction.

5.2.4. Analysis of the atomic state evolution

Using the simulation, we can investigate important properties of the temporal dependence of atomic states and increase the fidelity in measurements by optimizing the available parameters.

Compensation of ambient magnetic fields (y-direction)

Due to the presence of an effective magnetic field in y-direction in the vicinity of the focus, the compensation of ambient magnetic fields B_y becomes challenging as their effects are difficult to separate. If there is a magnetic y-field additional to the effective field of the laser beam, the y-component of equation 5.22 gets a position independent offset. For the state evolution of one atom this means that the time at which the influence of fields on the two sides of the y-z-plane compensate is either short before or after a full oscillation period, depending on the sign of the constant field and the initial position of the atom. Averaged over many atomic state measurements, the evolution will wash out and the maximal state population for rephasing will be reduced due to external magnetic y-fields as shown in figure 5.12. This figure includes both measured and simulated time evolutions of the state $|\Psi_H\rangle$ for different field strengths. As expected, the behavior averaged over many atomic projections is identical (up to statistical deviations in the simulation) for positive and negative fields. The reduction of the measured state population agrees with the simulation and a criterion for the required stability of magnetic y-fields can be found to be better than about $1.6\,\mathrm{mG}$. To optimize the y-component of the feedback stabilization we measure the state population at a time delay close to the maximum and adjust the y-field such that the state population reaches the highest level.

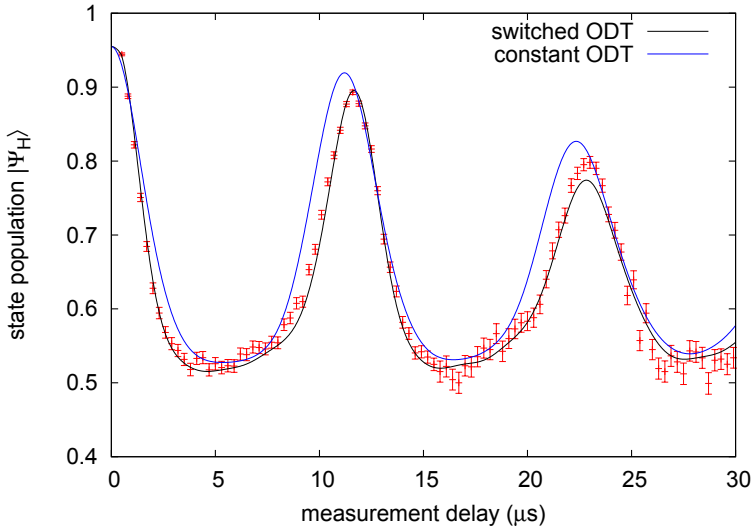

Figure 5.13.: Time evolution of the atomic state $|\Psi_H\rangle$ in an ODT of switched depth (measurement and simulation) and constant depth (simulation (blue curve)). The maximal state fidelity after one oscillation period is larger in the case of a constant depth of the trapping potential.

Matching of trap oscillation periods

Since the state evolution only allows measuring the atomic states (with high fidelity) after one oscillation period, we need a method to adjust this time in the experiments. A necessity especially for Bell experiments that require simultaneous measurements on two sides is that the trap periods are matched. The asymmetry of distances to the BSM for the two traps and the differing photon transmission times to the BSM mean that the trap periods also have to differ. The trap period depends on the power of the dipole trap laser and a wide tuning range is possible. However, the trap frequency should be high to keep the delay until the measurement small and avoid a strong influence of magnetic fields. Therefore, we chose trap oscillation periods of about $11\,\mu$s in lab 1 and about $14.5\,\mu$s in lab 2, respectively. Whereas the $14.5\,\mu$s correspond to a trap depth that was used before to load, store and manipulate atoms, reducing this time to $11.5\,\mu$s requires to increase the laser power by a factor of 1.7.

As changing the trap depth typically requires a recalibration of the experimental procedure (as e.g. transition frequencies depend on the trap depth), a first approach aimed at switching the dipole trap power only during the time delay before a measurement. After the detection of a photon in the BSM, the power of the optical dipole trap was increased within $500\,$ns after the photon emission. After the time delay it was switched off during the ionization pulse sequence and then switched on to the original value. This approach did not turn out to be practicable. Simulations for the case of a switched ODT compared to a constantly deeper ODT revealed

that the achievable fidelity of the rephased state is reduced when the ODT is switched (figure 5.13). This was verified both by measurements and by simulations and can be explained by the difference of the spatial distribution of atoms in a dipole trap. In a shallow trap potential the distribution of atoms is broader. When the trap is instantly switched to the deeper level this position distribution stays the same and the atoms are more likely to be in areas with a high effective magnetic field. Thus, the switching causes heating of the atoms which results in a decreasing measurement fidelity. Therefore, this method is not used and the trap depth is set to constant values throughout the experimental sequence.

Atomic temperature and cooling times

The shape of the observed state evolution curves and in particular the maximal fidelity after one oscillation period depend strongly on the atomic temperature. The spatial distribution of atoms according to the Boltzmann distribution is broader for higher temperatures and therefore the atoms reach areas of a higher effective magnetic field. The compensation of the accumulated phase that leads to a high fidelity of the state only works as long as we can neglect the longitudinal motion in the trap. With increasing temperature, the longitudinal velocities and therefore the mismatch of the fields the atom sees on the two sides of the y-z-plane increases and the accumulated phase does not sum up to zero. This behavior is shown in figure 5.14 a) for simulated state evolutions for atomic temperatures of $40\,\mu$K...$90\,\mu$K with all other parameters being the same as in table 5.2. Variation of the temperature in the experiment is done by using different cooling times before the 40 repetitions of an excitation burst (see e.g. figure 4.3). Measured state evolutions are shown for cooling times of $200\,\mu$s (red) and $350\,\mu$s (blue). The simulation parameters are optimized for the blue data points which are thus in good agreement with the simulated trace corresponding to an atomic temperature of $45\,\mu$K (black). The second measurement (red) does not fully match one of the simulated curves. However, the basic characteristics of an increased temperature which are in particular a reduced maximal fidelity of the state and a reduced width of the state evolution curve can be observed. This allows us to maximize the fidelity of the measured state, because the fidelity of the rephased state is higher for low temperatures. Additionally, it provides a fast way to check the efficiency of the cooling process by measuring the width of the maximum of the state evolution. Regular control of this is necessary, because the cooling efficiency can change, e.g. when the beams of the cooling laser get misaligned.

In figure 5.14 b) the measured state population at a constant time delay of $11\,\mu$s (close to the maximum) is shown in dependence on the length of the cooling period from $50\,\mu$s up to $450\,\mu$s in steps of $50\,\mu$s. This demonstrates again the increase of the state fidelity with increasing cooling times and the reachable fidelity saturates for a cooling time of about $350\,\mu$s. For this temperature the fidelity at the maximum is reduced by less than $1\,\%$ compared to the value without additional time delay.

The analysis of the temperature dependence of the state evolution thus allowed us to find optimal parameters for the cooling procedure and to increase the fidelity of the atomic state. Important properties of the measured state evolution are in agreement with the simulation. The residual difference between the simulation and the experiment is that we assume a constant temperature for all events in simulations, whereas in the experiment each of the 40 excitation attempts might

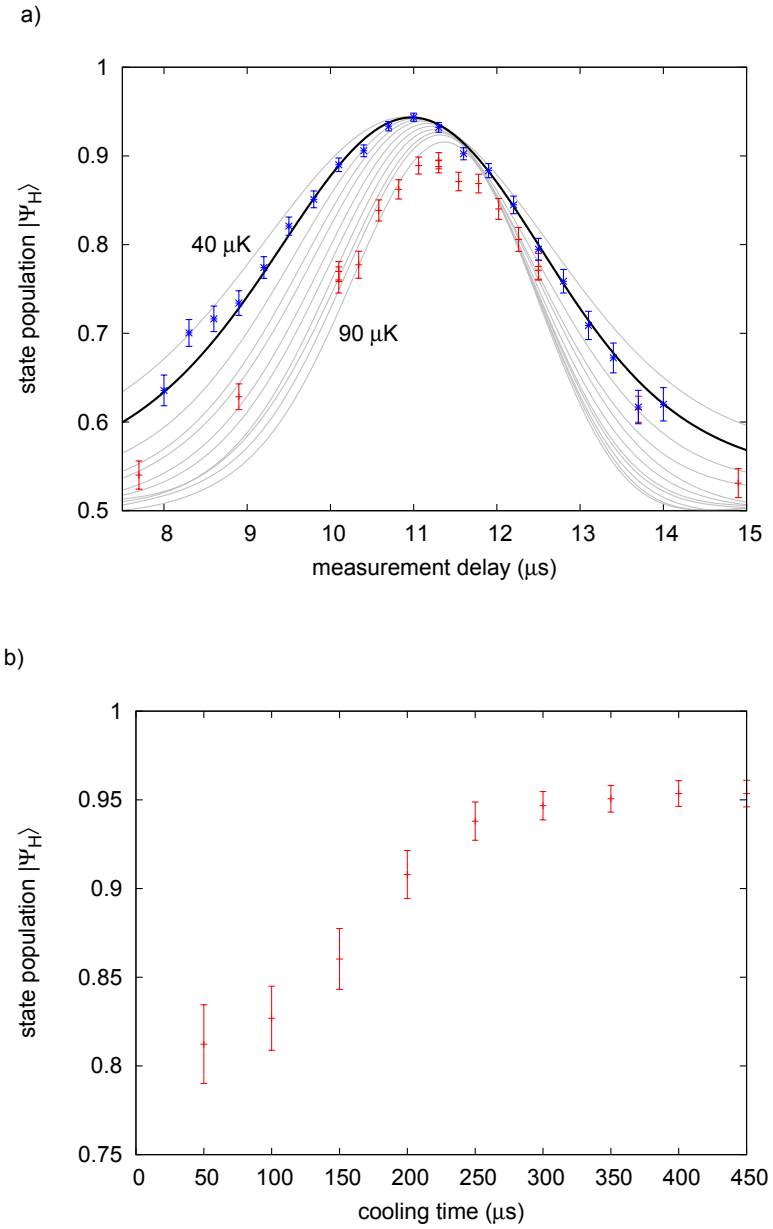

Figure 5.14.: Rephasing of the atomic state for different atomic temperatures. In the experiment, the average temperature is modified by changing the length of the cooling periods before the 40 repetitions of an excitation burst. a) Simulated state population for temperatures in the range of $40\,\mu$K..$90\,\mu$K. The black curve for $45\,\mu$K matches best to the measured data (blue). Decreasing temperatures clearly have two effects. First, the width of the curve gets broader and the maximal state population increases. Measurements for cooling periods of $200\,\mu$s (red) and $350\,\mu$s (blue) agree with the main characteristics of the simulation. b) Maximal state population (at $11\,\mu$s delay) in dependence of the length of the cooling period. Maximal measurement fidelity can be reached for a cooling time larger than $350\,\mu$s.

have a different average temperature due to heating in previous excitation cycles.

Asymmetry of the trap potential

As already mentioned, the geometry of the trap potential and the electric field distribution can deviate from the ideal theoretical model due to e.g. aberrations. The simulation uses equations 5.17, 5.18 and 5.19 to calculate the electric field vector in the focal region assuming a Gaussian input beam that is focused resulting in a field (anti-)symmetric around the quantization axis. Any aberrations can break this symmetry and thereby prevent the compensation of the accumulated phase. We observe this effect by comparing the maximal fidelity after a trap oscillation between measurements and simulations. The reachable fidelity in measurements is lower and the difference increases with the number of trap oscillations the atom performed during the time delay. A first approach to include this in the simulation is a factor a_{sym} affecting the strength of the effective magnetic field for positive and negative x values as

$$B_{long} \;=\; B_{long}\left(1+\frac{1}{2}a_{sym}\cdot\mathrm{sgn}(x)\right). \tag{5.26}$$

Adjusting a_{sym} to fit the measurements best (figure 5.15 a)) results in a value of about 0.10, thus the strength of the field on the two sides of the y-z-plane differs by 10%. However, the simulation still does not describe the data exactly and a more accurate model would be necessary. A starting point for this could be to investigate the aberration caused by the glass cell of the vacuum chamber. It is very likely that the glass plane (see figure 2.2) is not oriented perfectly perpendicular to the quantization axis but has a certain tilting angle of up to a few degrees. The resulting intensity distribution of the dipole trap beam in the focal region then becomes asymmetric (depending on the NA). Simulations of the intensity profile of the focused beam for different tilting angles of the glass cell are obtained with Zemax (figure 5.15 b)), however this does not provide the electric field vector required for calculations of the effective magnetic field. Still, this behavior gives rise to the conjecture that the effective field has a distinct asymmetry and better adjustment of the glass cell with respect to the axis of the objective is desirable.

Guiding fields

A possibility to improve the stability of the atomic states in (effective) magnetic fields might be the use of a magnetic guiding field. Applying a constant, strong magnetic field causes Larmor precession of the atomic states with the frequency $\omega_L = \frac{1}{\hbar} g_F \mu_B B$ and after the period $T = \frac{2\pi}{\omega_L}$ the atomic state is restored. To investigate the influence of instabilities we now consider small changes ΔB of this magnetic field. Adding a small magnetic field $\Delta B_{\parallel}$ along the direction of B results in a magnetic field vector of length $B + \Delta B_{\parallel}$. In the case of an additional field $\Delta B_{\perp}$ perpendicular to the original axis the resulting field vector has a length $\sqrt{B^2 + \Delta B_{\perp}^2}$ while its direction is slightly changed. Therefore, by using a guiding field the change of the Larmor frequency due to fluctuations of the fields perpendicular to the guiding field is reduced. In our case this effect can be used in the following way.

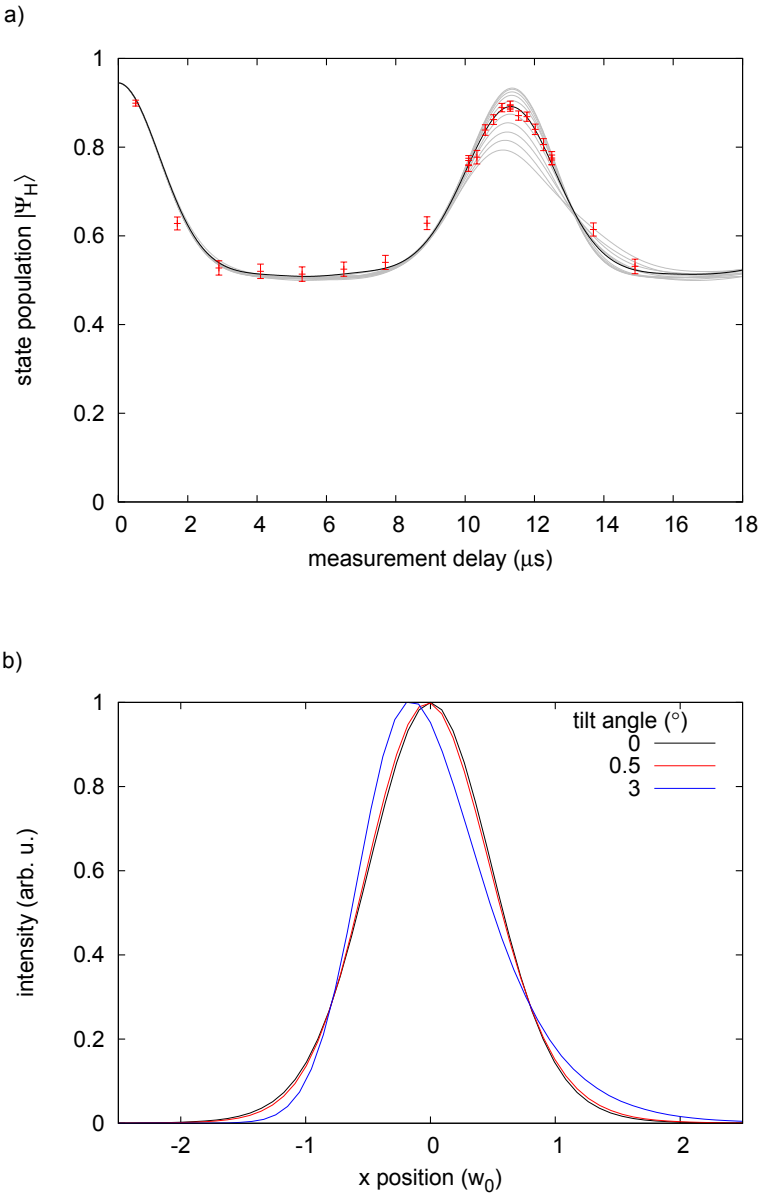

Figure 5.15.: a) Reduction of the state fidelity when the effective magnetic field is not fully anti-symmetric to the y-z-plane. Curves are for asymmetry factors $a_{\mathrm{sym}} = 0...0.2$. Best agreement with the measurement is achieved here for $a_{sym} = 0.1$ (black). b) Asymmetric beam profile at the focus for different tilting angles of the vacuum glass cell according to a beam simulation (Zemax, parameters comparable to our setup).

As explained in section 5.1.6, especially the drifts of the polarization of the dipole trap laser lead to an instability of the z-component of the effective magnetic field. To reduce the change of the larmor frequency due to this instability, a guiding field in the x- or y-direction could be applied. However, the longitudinal polarization in the ODT as described above, always results in an effective magnetic field in y-direction that depends on the position of the atom. It reaches values of several tens of mG for certain atomic trajectories. Thus, it is not possible to use a guiding field in the x-direction, but an additional field along the y-direction can be applied. A mandatory requirement for this guiding field is that the larmor frequency of the guiding field is equal to the (transverse) oscillation frequency of the atoms in the dipole trap. Then, the atomic state is restored after one oscillation period and the effect of the instability of the field in the z-direction on the fidelity of the atomic state can be suppressed. Simulations predict high stabilities in this case, but in a first experimental test the predicted fidelity could not be reached. However, for future applications (with a new setup and reduced aberrations of the ODT beam) this approach could get relevant and provide increased measurement delays.

5.3. Atomic state analysis after the time delay

The improved stabilization of magnetic fields and the control of dephasing effects caused by the AC-Stark shift in the dipole trap enable to preserve the atomic state with a high fidelity for several tens of μs which is an important step to achieve atom-atom entanglement over $398\,\mathrm{m}$. The visibility in atom-atom correlation measurements and the S-parameter in Bell experiments depend (besides the state preparation by the BSM) mainly on the fidelity of the atomic state analysis. In this section I will summarize the different influences (time-delay-independent and time-delay-dependent) on the atomic state analysis that appear in atom-photon correlation measurements. Atom-photon correlation measurements are thereby used as calibration of the atomic state analysis before experiments on atom-atom entanglement are performed.

5.3.1. Atom-photon correlation measurements and error analysis

Correlations between the photonic and atomic state measurement results are obtained by preparing an entangled atom-photon state and measuring both particles in different measurement bases. The photon is analyzed either in H/V or $\pm 45^\circ$ and the atomic measurement basis is varied by changing the polarization orientation of the readout beam. A full measurement is shown in figure 5.16 where the colors indicate the detected photon state and the linear polarization of the readout laser is changed from $\alpha = 0^\circ$-180° in steps of 22.5°. The atomic state is measured both without delay and after a full oscillation period at $11.1\,\mu\mathrm{s}$ for comparison and error analysis. The measurements were evaluated in addition with different atomic state detection schemes, namely fluorescence-based or channel-electron-multiplier (CEM) detection.

The sinusoidal function fitted to each set of data points is defined by

$$f(\alpha) \;=\; A\,\sin^2\left((\alpha-\phi)\right)+c,$$

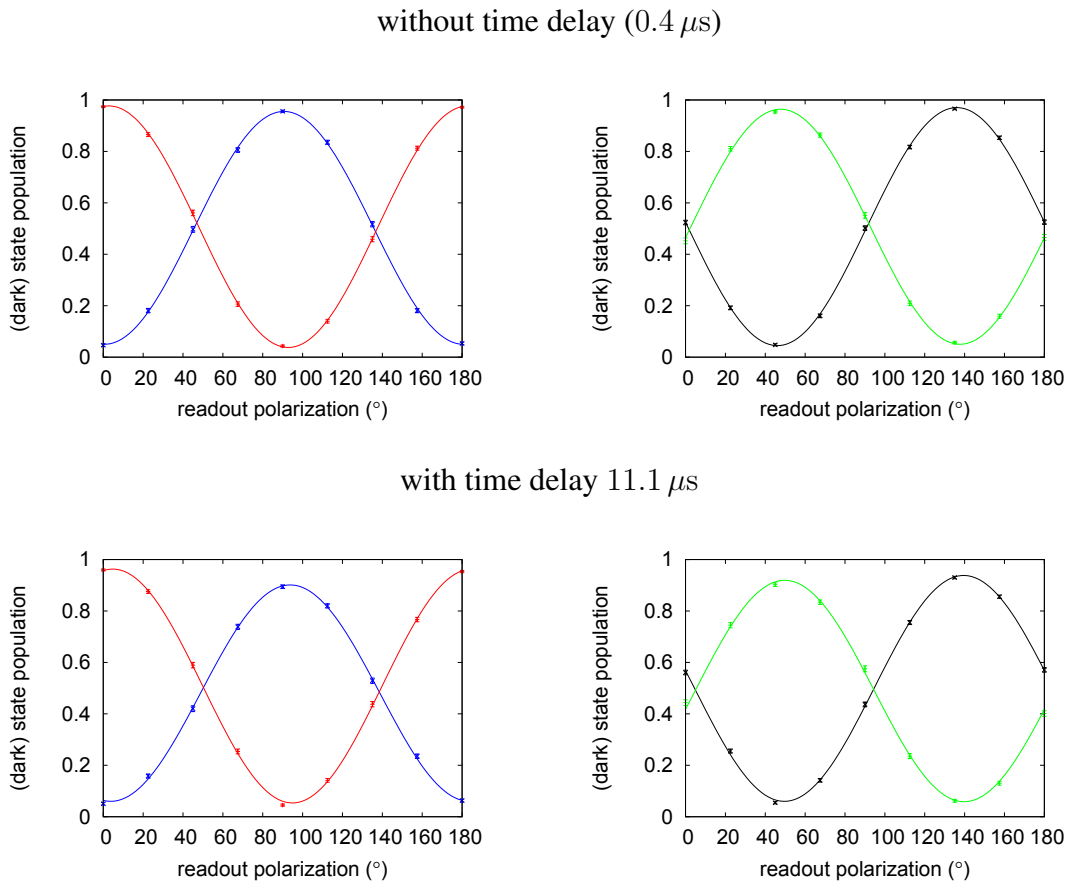

Figure 5.16.: Correlation measurements of atomic and photonic states. The different colors indicate the observed photonic state ($|H\rangle \mathrel{\hat{=}}$ blue, $|V\rangle \mathrel{\hat{=}}$ red, $|+\rangle \mathrel{\hat{=}}$ green, $|-\rangle \mathrel{\hat{=}}$ black). The atomic measurement basis is rotated by changing the (linear) polarization of the readout laser (vertical $\mathrel{\hat{=}} 0°$). Upper row corresponds to measurements without time delay whereas the measurements in the lower row where done after one oscillation period which is $11.1\ \mu$s in this case. The atomic state is analyzed using CEM detection.

	without time delay		
	A	$\Delta\phi(^\circ)$	c
red	0.939 ± 0.0050	2.85 ± 0.170	0.038 ± 0.0034
blue	0.905 ± 0.0064	0.65 ± 0.224	0.050 ± 0.0037
black	0.926 ± 0.0069	1.08 ± 0.193	0.045 ± 0.0042
green	0.914 ± 0.0086	2.69 ± 0.245	0.050 ± 0.0052
	with time delay		
	A	$\Delta\phi(^\circ)$	c
red	0.910 ± 0.0075	4.88 ± 0.261	0.053 ± 0.0050
blue	0.841 ± 0.0085	3.77 ± 0.319	0.060 ± 0.0049
black	0.878 ± 0.0086	4.55 ± 0.255	0.060 ± 0.0052
green	0.861 ± 0.0154	4.77 ± 0.466	0.058 ± 0.0092

Table 5.3.: Fit parameters for the correlation measurements in figure 5.16.

with the peak-to-peak amplitude A, the offset c and the phase ϕ. Like in chapter 3 we associate the amplitude A with the visibility V of the entangled state. The offset c in the ideal case should be 0. It is a parameter characterizing the quality of the state analysis (together with A). In particular, $1 - c$ is the probability to ionize atoms prepared in the bright state. The fit parameters for each curve are summarized in table 5.3. The phase ϕ should be 0, $\pi/2$, $\pi/4$ and $-\pi/4$, depending on the detected photon state. The deviation of the phase from these values is $\Delta\phi$.

The peak-to-peak amplitude characterizes the reachable correlations and is a measure for the probability to correctly detect the atomic state. In measurements without delay, possible reasons for its reduction are (see section 2.5):

- the intensity of the ionization laser is too low (due to low power or misalignment)
- the readout transition is too slow (due to low power, misalignment or frequency mismatch)
- the cycling laser does not transfer all population of the $F = 2$ ground state (low power)
- the CEM detection efficiency is too low (due to low amplification, wrong setting of time windows)
- the readout laser excites the dark state by an off-resonant transition (if the intensity is too high)
- there are CEM dark counts

Any of these errors will reduce the visibility and thereby the amplitude of the correlation curve. If one of the first four points applies the correlation curves will be additionally offset to a higher value for c. Errors concerning the CEMs can be identified by comparison to the fluorescence based method. A phase shift $\Delta\phi$ arises in measurements without time delay due to:

- a misaligned atomic measurement basis (defined by the polarization of the readout beam)

- a misaligned photonic measurement basis (e.g. due to polarization changes of photons in the fibers)

Although misaligned measurement bases can also reduce the visibility, the effect on the phase is easier to identify. Using this analysis thus allows us to correct time-delay-independent errors in the experiment.

For identifying time-delay-dependent errors that arise due to the Zeeman or AC-Stark shift we analyze the measurement with a time delay of $11.1\,\mu$s. The amplitude of the correlation curves is reduced as a result of the atomic state evolution if the dark state rotates into the $|m_F = 0\rangle_z$ state. This happens

- in the presence of a magnetic field along x. The x-field reduces the state population of $|\Psi_V\rangle$, thus the curve corresponding to photons detected with vertical polarization is influenced by this field. In particular, the measured population of the dark state will be reduced which can be observed for a measurement angle $\alpha = 0°$. The curve corresponding to photons detected with horizontal polarization is not affected.

- in the presence of a magnetic field along y. Then, the state population of atoms prepared in $|\Psi_H\rangle$ is reduced which is observable in the correlation curve (for photons with horizontal polarization) for a measurement angle $\alpha = 90°$.

- for imperfect rephasing during the oscillation in the trap potential. This effects the correlation curves similar to a magnetic field in the y-direction (reduced dark state population at $\alpha = 90°$).

Magnetic fields along x or y will also cause a reduction of the amplitude in measurements where the photons are analyzed in $\pm 45°$. But in this case the effects on the observed correlation curves are not distinguishable (if the field is pointing either in x or y-direction). Besides the amplitude of the correlation curves, magnetic fields can also cause a phase shift. The atomic states $|\Psi_V\rangle$ and $|\Psi_H\rangle$ undergo Larmor precession in an (effective) z-field which results in a phase shift in correlation measurements. Thus, a phase shift increasing with the time delay of a measurement indicates an (effective) z-field. Note, that we here assume magnetic fields that are oriented along one of the three axes. For an arbitrary field, the analysis of the effects on the correlation curves gets more complex.

Analyzing atom-photon correlation measurements is thus helpful to find error sources and a mandatory part of the calibration of the system before every two-atom experiment.

5.3.2. Calibration for two-atom experiments

To avoid time-consuming calibrations before and during an experimental run we limit these measurements to a reduced number of settings. The measured points shall efficiently indicate misalignment of the experimental setup and provide a quick identification of error sources. The most important data points are for readout polarizations of $0°$ and $90°$ where the contrast between atoms projected onto $|\Psi_V\rangle$ and $|\Psi_H\rangle$ is maximal. Especially at $0°$ most errors in the readout

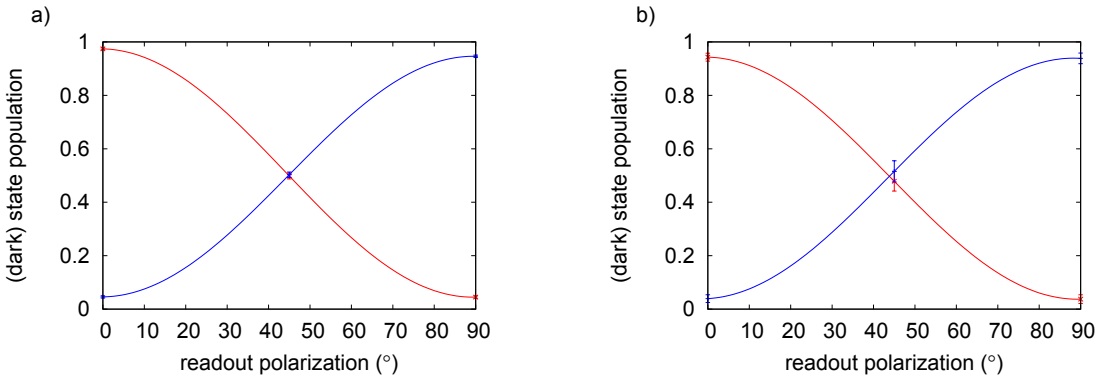

Figure 5.17.: Correlation measurement after optimal adjustment of all parameters before a Bell experiment (for photon polarizations $|H\rangle \mathrel{\hat{=}}$ blue, $|V\rangle \mathrel{\hat{=}}$ red). The number of settings is reduced to minimize the calibration time. a) Atom-photon correlations for the trap 1 setup. b) Atom-photon correlations for the trap 2 setup.

	trap 1			trap 2		
detected photon	A	$\Delta\phi(^\circ)$	c	A	$\Delta\phi(^\circ)$	c
$\|V\rangle$	0.901	-0.45	0.054	0.901	-1.71	0.061
$\|H\rangle$	0.929	-0.70	0.026	0.906	-0.74	0.057

Table 5.4.: Fit parameters for optimal correlations after the measurement time delay for trap 1 and trap 2.

scheme would be visible and the 90° measurement shows the quality of the rephasing due to oscillations in the ODT. A third measurement is done at 45° where the sensitivity to the phase of the correlation curve is maximal and magnetic z-fields are easily visible. Optimal results for these three settings for both trap setups are shown in figure 5.17 for the relevant measurement time delays of $10.7\,\mu$s (lab 1 (in a)) and $7.0\,\mu$s (lab 2 (in b)). The amplitudes (visibilities), phase shifts and offsets of these measurements are summarized in table 5.4. These data were measured before the experimental run to violate Bell's inequality that will be presented in the next chapter.

5.4. Summary

This chapter described the different mechanisms leading to dephasing of the atomic states. These are in particular the Zeeman shift of atoms in a magnetic field and the AC-Stark shift induced by the light of the optical dipole trap. Both effects lead to an undesired time dependence of the atomic states that has to be avoided for long-time measurement, where these shifts vary over time.

Ambient magnetic fields are therefore compensated by applying compensation fields according to the feedback signal of a magneto-resistive sensor placed close to the atom trap. Unfor-

tunately, the sensor shows drifts when it is exposed to the strong field of the MOT coils and a recalibration based on the comparison of this sensor with a long-term stable external sensor is necessary. Additionally, elliptical polarization of the dipole trap laser causes an AC-Stark shift similar to a magnetic field in the z-direction. This is minimized by setting a linear polarization for the trap beam in the confocal microscope. However, drifts of the birefringence of different optical components lead to varying polarization directions. To reduce these fluctuations, the setup was improved with a better temperature stabilization.

A further effect that is caused by focusing the dipole trap laser is the presence of longitudinally polarized components in the focal region. The resulting AC-Stark shift is equivalent to a (spatially varying) magnetic field in the y-direction. The resulting time evolution is quite complex and shows fast dephasing of the atomic states. Due to the inhomogeneity, it is not easy to suppress or compensate this field, but an extensive investigation of the resulting time evolution of atomic states and the comparison of simulations with experiments, allowed us to find time delays at which the initial atomic state is restored.

The combination of these efforts allowed us to verify atom-photon entanglement for time delays of about $10\,\mu$s which is a requirement for long-distance atom-atom entanglement. Correlation measurements of the atom-photon state show high visibilities of about $V \approx 0.9$ that are well suited for an atom-atom entanglement verification by a violation of Bell's inequality that will be discussed in the next chapter.

6. Violation of Bell's inequality simultaneously closing the detection and the locality loophole

Bell's inequality allows to test the validity of any local-realistic description of nature [2]. This can be achieved by evaluating correlations between the measurement outcomes on two distant particles. According to Bell's findings these correlations have a stringent bound for local-realistic theories. Such theories have two important assumptions namely realism and locality: Realism means that certain properties are already assigned quantitatively to the system before it is measured. These properties thus exist independent of a measurement. The principle of locality states that any system can be causally influenced only by events in its backward light cone. Or with other words, any interaction between two particles can not propagate faster than at the speed of light.

Quantum mechanics, on the contrary, is not a local-realistic theory and the bound of Bell's inequality can be exceeded. To achieve that, the total quantum system, consisting of two particles, has to be in an entangled state. If the particles are measured along suitable directions, the measurement results exhibit correlations not explainable by classical statistics. Experimental tests were performed already soon after Bell's proposal [4, 5, 6, 75] and confirmed the prediction of quantum mechanics. But most experiments so far relied on additional assumptions, opening so-called loopholes for local-realistic descriptions [76, 77]. Here, I will present the results of a test violating Bell's inequality by measurements on spins of atoms entangled over a distance of $398\,\mathrm{m}$. The experimental scheme allowed us to close the two most important loopholes in a single experiment, thereby supporting the predictions of quantum mechanics and rejecting the possibility of local-hidden variables (LHV).

6.1. Bell's inequality

A test of Bell's inequality requires measurements on two separated spin 1/2 particles. On each side, one of two measurement directions is selected, $a \in \{\alpha, \alpha'\}$ for particle 1 and $b \in \{\beta, \beta'\}$ for particle 2, respectively. The state measurements provide the result $|\uparrow\rangle_{a/b}$ or $|\downarrow\rangle_{a/b}$ and comparing the results on both sides, the states can be either correlated ($|\uparrow\rangle_a |\uparrow\rangle_b$ or $|\downarrow\rangle_a |\downarrow\rangle_b$) or anti-correlated ($|\uparrow\rangle_a |\downarrow\rangle_b$ or $|\downarrow\rangle_a |\uparrow\rangle_b$). The trials are repeated several times in an experimental run and a total number of N events are recorded. We write the number of events in each combination of measurement directions as $N_{a,b} = N_{a,b}^{\uparrow\uparrow} + N_{a,b}^{\uparrow\downarrow} + N_{a,b}^{\downarrow\uparrow} + N_{a,b}^{\downarrow\downarrow}$. The evaluation of the experiment is based on the calculation of correlators $\langle \sigma_a \sigma_b \rangle$:

$$\langle \sigma_a \sigma_b \rangle \;=\; \frac{1}{N_{a,b}} \left(N_{a,b}^{\uparrow\uparrow} + N_{a,b}^{\downarrow\downarrow} - N_{a,b}^{\uparrow\downarrow} - N_{a,b}^{\downarrow\uparrow} \right) \tag{6.1}$$

If all measurement results are correlated, this correlator will have a value of $+1$. On the other hand a measurement of only anti-correlated spins will yield the value -1.

Bell's inequality is then tested in the form developed by Clauser, Horne, Shimony and Holt (CHSH) [3]

$$S \;=\; |\langle \sigma_\alpha \sigma_\beta \rangle + \langle \sigma_\alpha \sigma_{\beta'} \rangle| + |\langle \sigma_{\alpha'} \sigma_\beta \rangle - \langle \sigma_{\alpha'} \sigma_{\beta'} \rangle| \;\leq\; 2 \tag{6.2}$$

that only requires the evaluation of four correlators for obtaining the parameter S. The theorem then states that S cannot exceed a value of 2 for any local-realistic theory. In quantum mechanics, with an appropriate choice of measurement directions we can violate this inequality. The atoms in our experiment are prepared (with a certain fidelity) in the entangled Bell-states $|\Psi^{\pm}\rangle = \frac{1}{\sqrt{2}} \left(|\uparrow\downarrow\rangle_x \pm |\downarrow\uparrow\rangle_x \right)$. In this case, for the settings $\alpha = 0°$, $\alpha' = 90°$, $\beta = -45°$ and $\beta' = +45°$ (defined in the spin space) a value of $S > 2$ can be reached.

6.2. Loopholes

A conclusive Bell test imposes very strict requirements on the experiments to avoid loopholes. The test is loophole-free when it only requires a minimal set of basic assumptions that cannot be reduced any further in experiments. The two most important loopholes are the locality and the detection efficiency loophole which will be described in detail in the following.

6.2.1. Detection efficiency loophole

The detection efficiency loophole arises, if a critical fraction of particle pairs prepared for measurements is not detected due to inefficient detectors or other losses. Then, one has to assume that the not detected particles behave the same way as the detected ones in the evaluation of Bell's inequality. This is called the fair-sampling assumption which is not justified for all possible LHV-theories, thus the experiment has to be performed such that this assumption is not required. The loophole was first closed in experiments with entangled ions [8]. The required detection efficiencies of particles ($\approx 83\%$ for the CHSH inequality provided perfect alignment of all other parameters) are much easier to achieve with matter particles than with photons that are always affected by photon loss. Photonic Bell tests therefore use a different formulation of Bell's inequality that only requires a detection efficiency of $\approx 67\%$ [78]. This formulation, together with significant progress in the generation of entangled photon pairs [79, 80] and the development of highly efficient single photon detectors [81] enabled the closing of the detection efficiency loophole also for those experiments [9, 10].

In our experiment, we use an event-ready scheme [24] whose main feature is that the setup provides a (binary) measurement result for every event. Then, the fair sampling assumption is not

required and this loophole is closed. Any inefficiency of detectors, e.g. of the channel-electron multipliers (CEM), only affect the fidelity of the measurement.

6.2.2. Locality loophole

To close the locality loophole, one has to avoid all possibilities of causal dependence between the two measurements. This is fulfilled when the state analyses by the two observers are space-like separated which means that no signal propagating at most at the speed of light can communicate information between the two setups within the measurement time. The overall time for a state measurement for that purpose has to start with the choice of the analysis direction by a quantum random number generator (QRNG). The end of a measurement is considered to be reached when the outcome has been converted into a classical signal. We assume this is the case when the outcome of the measurement is a macroscopic voltage pulse that is perfectly cloneable. Then, according to the no-cloning theorem [82], the signal is a classical entity that exists without observation. Closing of the locality loophole was first reached with photons from a down-conversion source [7]. In that work, the photons were separated by $400\,\mathrm{m}$ to guarantee space-like separation, however the photon detection efficiency was to low to close both major loopholes simultaneously.

In our experiment, the locality loophole is closed by performing correlation measurements on entangled atoms that are separated by $398\,\mathrm{m}$. The result of the state measurements is obtained within $1.1\ \mu\mathrm{s}$ which fulfills the requirement of space-like separation.

6.2.3. Closing the two main loopholes in one experiment

Until recently, all experiments closed at most one of the two loopholes, while the other one was left open. Therefore, each of the experiments can still be explained in a local-realistic way. To achieve a rigorous violation of Bell's inequality, both loopholes have to be closed simultaneously. Closing both the locality and the detection loophole in a single experiment was achieved only very recently [11, 13, 14]. The first experiment was based on entangled spins in NV-centers over a distance of $1.3\,\mathrm{km}$. The other two experiments were realized with entangled photons from a down-conversion source.

6.2.4. Further frequently mentioned loopholes

There are further loopholes that have to be considered in an experiment. The first one I want to discuss is the memory loophole [83]. It arises if one has to assume that every trial (every measured event) in a Bell test is independent from previous trials. For finite statistics, however, a systematic violation of Bell's inequality can be reached for a system described by an LHV-theory with knowledge about previous events. Furthermore, allowing for memory effects means that the experiment cannot be evaluated with Gaussian statistics (that require independent trials). Anyway, this loophole can be closed, if the evaluation of the measurement results accounts for this effect and the hypothesis tests used in the evaluation of our experiment were designed to fulfill this criterion.

The second loophole that is often referred to is the free-will (or freedom of choice) loophole [77, 84]. It targets the independence of the basis settings on the two sides from the local hidden variables and from previous events. If the LHVs are defined in a space-time region that is not space-like separated from both QRNGs, then the QRNGs may influence the LHVs or vice-versa. It is however difficult to assign a certain time to the generation of the LHVs governing the current experimental trial. A typical moment in an event-ready scheme as it is used here would be the projection of the atoms onto an entangled state by the Bell-state measurement (BSM). Since our QRNGs are located next to the atom traps (see figure 4.1) and the atomic states are measured only after receiving the heralding signal, this loophole is not accounted for in our experiment.

Except for the last loophole, which can not be closed in principle, but only reduced to assumptions about correlations of events in the near or far past [18], all other loopholes were closed in this work.

6.3. Closing the locality loophole

To test Bell's inequality we generate entangled atom pairs according to the methods explained in chapter 4. When the successful state preparation is registered at the BSM arrangement (see section 2.6) and the heralding signal is transmitted to both trap setups (see section 4.2.3), the atomic states are analyzed simultaneously. A space-time diagram of the experimental sequence is shown in figure 6.1 indicating that the measurements on both sides are space-like separated.

Closing the locality loophole requires fast measurements which is possible with our state selective ionization scheme. In the first part of this section I will describe the different steps of the measurement sequence. In the second part the focus will be on the timings and durations for all individual steps as well as the overall measurement time. Finally, I compare the obtained measurement times with the signal transmission times resulting from the distance between the atom traps to derive the criterion of space-like separation and thereby prove that the locality loophole is closed in our experiment.

6.3.1. Atomic state analysis

The complete atomic state analysis consists of the selection of the measurement direction, the switching of the desired readout polarization, the state-selective ionization, the detection of ionization fragments and the signal processing. The relevant components are depicted in figure 6.2.

Selection of the measurement direction

A crucial requirement to rule out LHV-theories is that locally no information is available about the choice of the measurement direction of the other side until the state analysis is finished. Therefore, each direction has to be chosen by a trustworthy random number generator whose output can not be predicted beforehand. Since any random number generator requires assumptions on its functioning this is a difficult task that will be briefly discussed here. Further details

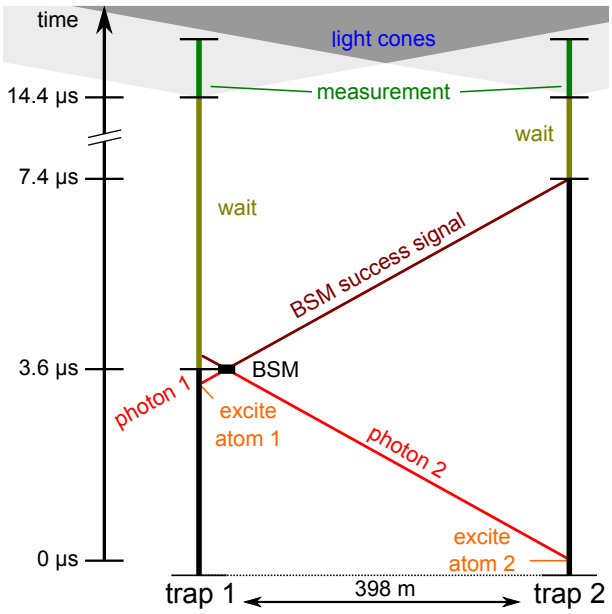

Figure 6.1.: Space-time diagram of the experimental sequence. Atoms in trap 1 and trap 2 are excited and emit photons. In lab 1, a BSM on the photons is performed. Note, that the position of the BSM is not scaled correctly in this diagram (The distance to trap 1 is only about $2\,\mathrm{m}$). After a successful BSM, the signal is transmitted to both traps and measurements can be performed. The measurements are space-like separated when the total measurement time is shorter than a speed-of-light signal needs to propagate between the two laboratories (indicated by the light cones)

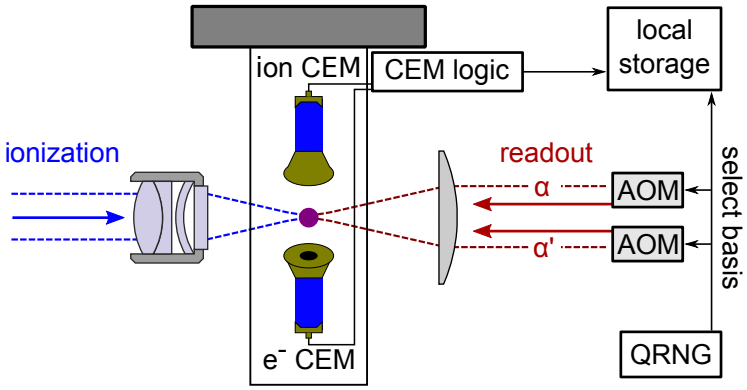

Figure 6.2.: Schematic of the state analysis in the Bell test. The output bit of the quantum random number generator (QRNG) selects which of the two AOMs is switched on. Each AOM provides a different polarization (α, α') of the readout beam that determines the measurement direction. Detection events of the CEMs are recorded by a local storage (together with the random bit) to evaluate the result of each trial.

will be explained in another thesis [85].

In our experiment, the measurement direction on each side is chosen by a quantum random number generator (QRNG) [16]. It is based on counting the parity of photons detected from an attenuated LED by a photo multiplier tube (PMT) within a certain time window. Depending on the result it returns either the bit 0 or 1. The physical model relies on the assumption that the photon detection events from an LED source are fully uncorrelated. Thus, the parity of detected photons does not depend on any event in the past and is independent of the LHVs.

Ideally, we want to obtain both outputs with the same probability of 0.5, otherwise the QRNG has a bias. The attenuated light of the LED has a Poissonian photon statistics that theoretically does not allow for a zero-bias operation. However, the dead-time of the PMT can be used to reduce the bias to values of less than 10^{-5} without any post-processing. This system generates random bits at a rate of $50\,\mathrm{MHz}$ and the bits do not have measurable correlations to all bits generated more than $80\,\mathrm{ns}$ earlier. A further analysis of the obtained random bits, their bias and correlations are presented in [15]. There, we also present an enhanced physical model of the QRNG that allows us to estimate its predictability.

Switching of the measurement basis

To analyze the atomic state in the desired basis, the polarization of the readout laser has to be set accordingly. While the conventional approach of switching the polarization by means of an electro-optical modulator (EOM) turned out to be unpracticable [86], we followed another approach. For that purpose, the readout beam is split into two paths of different polarization α, α' (β, β' for trap 2) that are both switchable with AOMs. The decision which AOM is activated is made according to the output bit of the QRNG. The two paths are overlapped and directed onto the atom trap. The polarization is thus set by activating only one of the AOMs that provides the desired polarization.

Detection of the measurement result

As the readout beam is applied to the atom, the dark and bright states are defined in dependence on its polarization according to equation 2.6. Atoms in the bright state get ionized, the fragments are accelerated towards the CEMs and are detected after a certain time-of-flight. The particles impinge on the detectors where they generate an electron avalanche that produces a small current pulse at the output. The electric pulse is then converted to a logical TTL-pulse by a comparator. At this point we consider the measurement as being finished, because the logical TTL-pulse is perfectly cloneable and surely a classical signal.

An arrival time histogram of ionization fragments in the trap 1 setup is shown in figure 6.3. The time $t = 0$ corresponds to the time when the CU starts the measurement, i.e. when it sends the request for a random bit. The measured particle arrival times then correspond to the time when the signal is converted to a logical pulse. The obtained histograms allow us to define two fixed time-windows in which the detection events of the ionization fragments are expected. A logical gate acting on the TTL-pulses of detected particles enables time filtering of events and

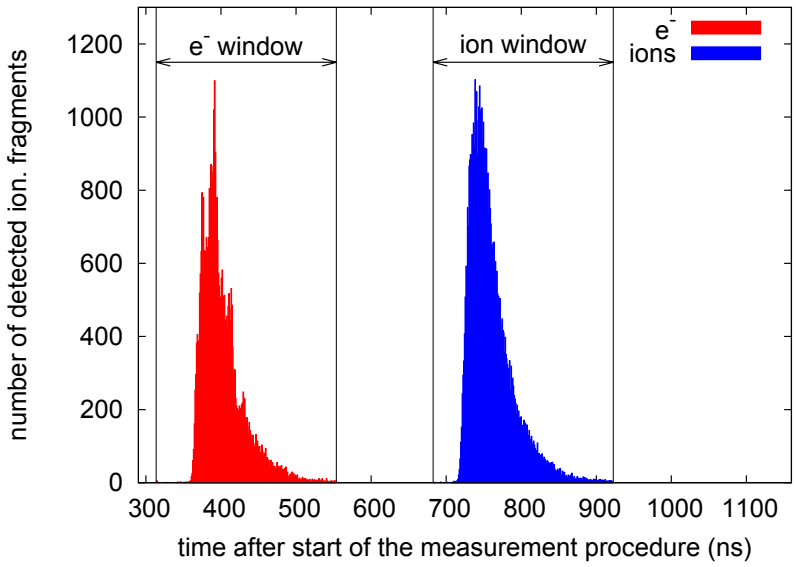

Figure 6.3.: Arrival time histogram of ionization fragments. Electrons (red) and ions (blue) are detected in different time-windows. All events outside the time-windows are rejected.

optimizing the signal to noise ratio. The acceptance time windows are indicated in figure 6.3 by black lines.

Every requested random bit which was used for a measurement is saved by a local storage. For each measurement, the local storage also records all CEM clicks that arrive within a defined time window. The result is then obtained by checking if at least one ionization fragment was detected after a measurement was initiated. If this is the case, the result is associated with the state $|\uparrow\rangle_{a/b}$, otherwise the result of the measurement is set to the state $|\downarrow\rangle_{a/b}$.

6.3.2. Timings of the state analysis procedure

Figure 6.4 shows a space-time diagram of all relevant processes of the state analysis. The origin of the time axis is the generation of the common start signal by the FPGA after a successful two-photon coincidence in lab 1. This signal is transmitted to both CUs. The connection to the local CU is done with a $50\,\mathrm{cm}$ coaxial electrical cable resulting in a delay of $2.5 \pm 0.2\,\mathrm{ns}$. To transmit the signal to the distant CU in lab 2 it is converted by an asynchronous electro-optical converter and sent via the $700\,\mathrm{m}$ optical link. The propagation time is measured by sending a signal to the other side and back. The measured delay yields a propagation time to the remote CU of $3717 \pm 7\,\mathrm{ns}$. Additional waiting times are appended to achieve rephasing of the atomic states (section 5.2). These delays are chosen such that the atoms perform one full transversal oscillation in the trap before the measurement. Once the states are rephased (after $10.74\,\mu\mathrm{s}$ and $7.0\,\mu\mathrm{s}$, respectively) the CUs initiate the state analysis. The oscillation periods were chosen with the aim to start the measurements on both sides almost simultaneously (trap 2 starts $28.5\,\mathrm{ns}$ earlier).

The measurement itself is initiated by the request of a random bit of the QRNG. Electrical propagation and the internal processing of the QRNG take $59 \pm 1.5\,\mathrm{ns}$ and $56 \pm 1.5\,\mathrm{ns}$ in the two setups, respectively. The random bit determines the measurement direction which is associated in our setup with the activation of one of two AOMs. The switching time of an AOM is mainly determined by the propagation of an acoustic wave in its crystal. To minimize this time we adjust the AOM in a way that the light passes the crystal close to the transducer (more details are given in reference [45]). Together with the propagation times in cables and fibers, the readout laser beam arrives at the atom $217 \pm 4\,\mathrm{ns}$ and $204 \pm 4\,\mathrm{ns}$ after the QRNG returns an output signal, respectively. Ionized fragments get accelerated towards the CEM detectors. From calculations, we obtain a time-of-flight of electrons to the detector of about $3\,\mathrm{ns}$. Using this, we extract the ionization time and the time-of-flight from arrival time histograms of electrons and ions (see figure 6.3). The length of the time-windows in the experiment are $240\,\mathrm{ns}$ ($160\,\mathrm{ns}$) for electrons and $240\,\mathrm{ns}$ ($220\,\mathrm{ns}$) for ions in the respective setup, trap 1 (trap 2). The time between the first detected electrons and the end of the ion acceptance window indicates the maximal time needed for the ionization process and the time-of-flight of particles to the detectors which is $570 \pm 3\,\mathrm{ns}$ and $725 \pm 3\,\mathrm{ns}$ on the two sides, respectively. The uncertainty of $3\,\mathrm{ns}$ results from the poor statistics in the determination of the detection times of the first electrons in the arrival time histograms. In contrast, the cut-off of the last ions is known very precisely as it is defined by the time window. The flight times on the two sides differ because of different applied acceleration voltages which are set to values that allow an operation without high-voltage breakdowns. In

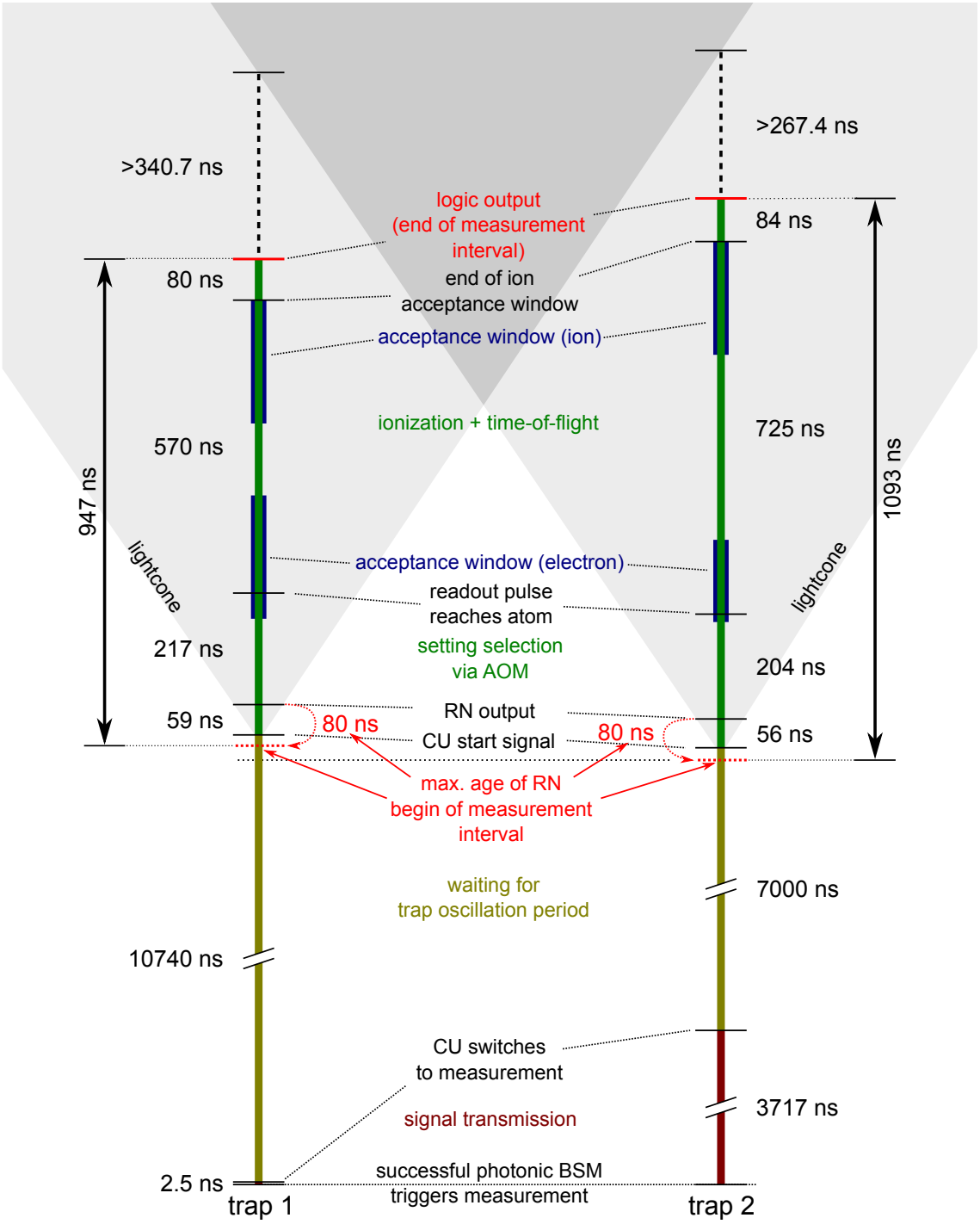

Figure 6.4.: Space-time diagram of the state measurements in trap 1 and trap 2.

particular, the trap 2 setup is more susceptible to breakdowns and has to be operated at a lower voltage. The end of the measurement is reached when the output of the CEMs is converted to a logical TTL- pulse by a comparator. This happens $80\,\mathrm{ns}$ and $84\,\mathrm{ns}$ after the detection.

The overall time for a measurement is then obtained by including the maximal age of the random bit which is assumed to be $80\,\mathrm{ns}$. We get a value of $947 \pm 1\,\mathrm{ns}$ for trap 1 and $1093 \pm 1\,\mathrm{ns}$ for trap 2, respectively. The uncertainties are smaller than for the single durations in the space-time diagram, because the overall time is obtained by comparing two signals of the CU. These are on the one hand, a trigger signal of the CU that is recorded by a time-to-digital converter (TDC) at the beginning of the state analysis and on the other hand, the end of the ion acceptance window that is also defined by the CU and which would be the last moment where the (cloneable) TTL-pulse from the CEM comparator would be accepted. The overall measurement time is derived from this time difference by subtracting propagation times in cables and electrical converters which can be done with low uncertainty.

6.3.3. Space-like separation

Knowing the measurement times and the distances between the QRNGs and atom traps on both sides we can verify that the measurements are space-like separated. In chapter 4.1.1 and in particular in table 4.1 we specify the distances:

- QRNG 1 $\leftrightarrow$ trap 2: $402.7\,\mathrm{m}$
- QRNG 2 $\leftrightarrow$ trap 1: $398.0\,\mathrm{m}$

Assuming a maximal error in the determination of these distances of about $30\,\mathrm{cm}$, we reduce them each by $1\,\mathrm{m}$ to guarantee that the actual distance is above this value. The minimal propagation times of signals from one side to the other are therefore:

- QRNG 1 $\leftrightarrow$ trap 2: $401.7\,\mathrm{m}/c \;=\; 1339.9\,\mathrm{ns}$
- QRNG 2 $\leftrightarrow$ trap 1: $397.0\,\mathrm{m}/c \;=\; 1324.2\,\mathrm{ns}$

Space-like separation of the measurements is achieved, when information from one side (starting with the generation of the random number) cannot influence the measurement on the other side. This potential signal (assumed to propagate at the speed of light) is indicated by the light cones in figure 6.4. Using the results from the previous section, the maximal measurement times are $948\,\mathrm{ns}$ and $1094\,\mathrm{ns}$ in trap 1 and trap 2, respectively. Here, we also assume the maximal error and therefore the maximal time within the error range. Furthermore, we include the uncertainty of $7\,\mathrm{ns}$ of the transmission time of the heralding signal to lab 2 and the earlier starting time of the state measurement in lab 2 of $28.5\,\mathrm{ns}$. Then, we can calculate time margins $\triangle t_{1,2}$ for both sides which are the times between the end of the measurement and the earliest arriving time of information from the other side. For the setup in lab 1 we obtain

$$\triangle t_1 \;=\; 1324.2\,\mathrm{ns} - 28.5\,\mathrm{ns} - 7\,\mathrm{ns} - 948\,\mathrm{ns} \;=\; 340.7\,\mathrm{ns} \tag{6.3}$$

and for lab 2

$$\triangle t_2 \;=\; 1339.9\,\mathrm{ns} + 28.5\,\mathrm{ns} - 7\,\mathrm{ns} - 1094\,\mathrm{ns} \;=\; 267.4\,\mathrm{ns}. \tag{6.4}$$

These time margins indicate that the state analysis is space-like separated even if we assume timing errors in the experiment of up to $267.4\,\mathrm{ns}$. In principle, the smallest time margin could be increased by further delaying the state analysis in trap 1. Then the time margins would become symmetric and both reach a value of $304.0\,\mathrm{ns}$.

6.4. Experimental results

For performing a Bell test, a preselected number of 10000 events were measured, thereof 5000 for each heralded atom-atom state $|\Psi^-\rangle$ and $|\Psi^+\rangle$. This number was chosen to achieve sufficient statistics and get a significant violation within a reasonable overall time. The data were measured within 4 days, including a daily maintenance break of about 3 hours. The event rate was about 2 events per minute which is close to the maximum we can achieve.

6.4.1. Evaluation of Bell's inequality

Figure 6.5 shows the results as event tables according to the measurement outcome. The tables include the total number of events per measurement basis combination $N_{a,b}$ and event numbers for the possible results of the state measurements, e.g correlated ($\uparrow\uparrow$ and $\downarrow\downarrow$) and anti-correlated ($\uparrow\downarrow$ and $\downarrow\uparrow$). From the event numbers we calculate the correlators according to equation 6.1 that are also shown in the plot above the table.

Using these data we evaluate the S-parameters (equation 6.2)

$$S^- \;=\; 2.240 \pm 0.047 \tag{6.5}$$

$$S^+ \;=\; 2.204 \pm 0.047 \tag{6.6}$$

for the states $|\Psi^-\rangle$ and $|\Psi^+\rangle$, respectively, with errors being one standard deviation according to Gaussian statistics. They show a clear violation of Bell's inequality by 5.1 and 4.3 standard deviations to the LHV-limit of $S = 2$. The two obtained S-parameters can also be combined. This can be done by calculating the average S-parameter weighted with the event numbers which yields $S_m = 2.222 \pm 0.033$.

6.4.2. Analysis of the results

The obtained S-parameter is in good agreement with our expectation from previous experiments over a shorter distance [25]. Despite the increased challenge to entangle atoms over such a long distance the fidelity of the atomic state analysis and the stability of the setup could be increased leading to a slightly higher S-parameter.

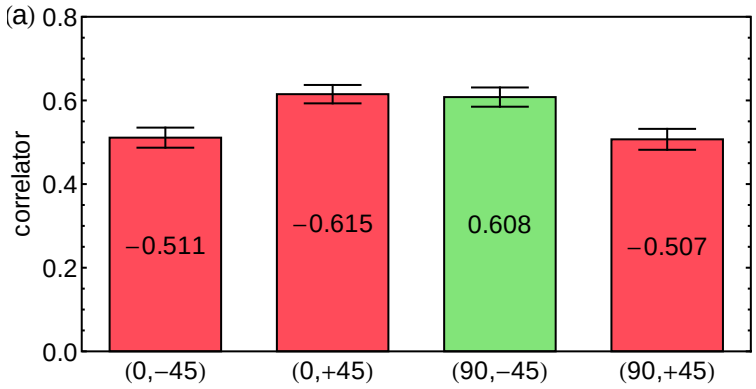

a, b	$N_{a,b}$	↑↑	↓↓	↑↓	↓↑	$\langle\sigma_a\sigma_b\rangle$
$0, -45$	1296	168	149	443	536	-0.511 ± 0.024
$0, +45$	1241	122	117	492	510	-0.615 ± 0.022
$90, -45$	1239	535	461	115	128	0.608 ± 0.023
$90, +45$	1224	172	130	439	483	-0.507 ± 0.025

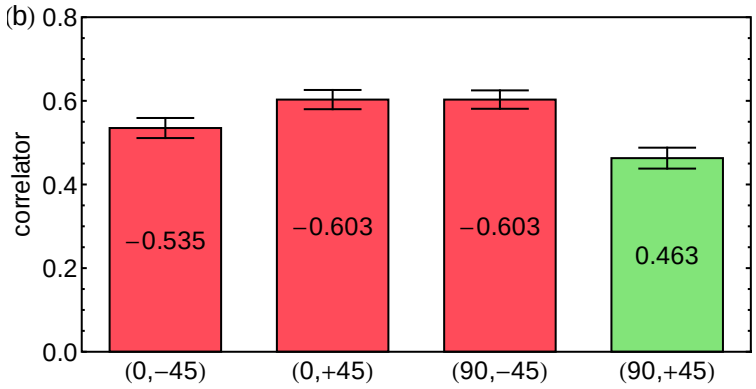

a, b	$N_{a,b}$	↑↑	↓↓	↑↓	↓↑	$\langle\sigma_a\sigma_b\rangle$
$0, -45$	1243	154	135	483	471	-0.535 ± 0.024
$0, +45$	1220	135	107	471	507	-0.603 ± 0.022
$90, -45$	1263	134	117	499	513	-0.603 ± 0.023
$90, +45$	1274	489	443	160	182	0.463 ± 0.025

Figure 6.5.: Event tables and correlators of the presented experimental run. Results are given for atoms in the state $|\Psi^-\rangle$ (a) and $|\Psi^+\rangle$ (b).

It is noticeable that the S-parameter for atoms heralded in the state $|\Psi^+\rangle$ is lower than for atoms in the state $|\Psi^-\rangle$. If we also consider further runs that are presented in [15], this difference is significant. However, the S-parameter does not contain enough information to analyze this effect. To extract additional information we can take a closer look at the single correlators. In the ideal case all 4 correlators should have the same value (besides the sign). In the case of a maximally entangled state this is $\langle\sigma_a\sigma_b\rangle = \pm 1/\sqrt{2} \approx \pm 0.707$. For the S-parameters reached in our experiment we would thus expect correlators of about ± 0.56 and ± 0.55 for atoms heralded in the state $|\Psi^-\rangle$ and $|\Psi^+\rangle$, respectively. The presented correlators are however pairwise shifted, two to higher values and two to lower values. This indicates a phase on the atom-atom state that can be caused either by a misalignment of the measurement directions or, more likely, an effective magnetic field. During the maintenance, measurements of the time evolution of the states revealed small fields in the z-direction of about $1\,\mathrm{mG}$ each day. As stated earlier (see section 5.1.6), we assume that these drifts are mainly caused by the drifting ellipticity of the polarization of the ODT light. The actual difference between the correlators is however small and making them symmetric would only slightly increase the reachable S-parameter.

If there are magnetic z-fields in both atom traps, the effect on the correlators will be different for atoms in the state $|\Psi^-\rangle$ and $|\Psi^+\rangle$ and depend on the relative direction (the sign) of the magnetic field. When the field strength on both sides is identical, the correlators for atoms prepared in the state $|\Psi^-\rangle$ ($|\Psi^+\rangle$) will not be influenced for fields pointing in the same (opposite) direction, respectively. Thus, a different value of the S-parameter for both states can also originate from magnetic fields. However, we expect this effect to be smaller than the observed deviations. To further investigate this and maybe find ways to improve the results (especially for the state $|\Psi^+\rangle$), a measurement of the density matrix of the entangled atom-atom state might be helpful.

6.4.3. Hypothesis test

A significant rejection of local-realistic theories requires a rigorous statistical analysis of the results obtained in a Bell test. In such analysis, one tests the hypothesis that LHVs can reproduce the measured data. The probability that an experiment governed by LHVs can produce a violation that is equal (or larger) to the one observed in the experiment is the p-value that can be calculated with different methods. One of them is a game formalism [87] in which two parties (representing the LHVs) get random inputs (measurement directions) and try, based on any strategy allowed by local-realistic theories, to violate Bell's inequality. They "win" one trial, if the results are anti-correlated for three combinations of measurement settings and correlated for the fourth combination. The maximal probability for winning β_{win} is bounded for local-realistic theories ($\beta_{\mathrm{win}} \approx 0.75$, the exact value depends on the predictability of the random inputs). Thus, the probability that the number of "wins" reaches at least the number observed in the experiment can be calculated from a binomial distribution. If applied to our experiment, the measured data provide a p-value of $p = 1.739 \times 10^{-10}$ [15] which rules out the possibility that the experiment can be explained in a local-realistic way with a very high level of significance. The hypothesis tests done in our group can be found in reference [15] and will be described in detail in another thesis [85].

6.5. Summary

Based on the preparation described in the previous chapters we performed a test of Bell's inequality with atoms entangled over a distance of $398\,\mathrm{m}$. Both the locality and the detection efficiency loophole were closed and the obtained data violates Bell's inequality and agrees well with the quantum mechanical prediction. In particular, we obtained S-parameters of $S = 2.240 \pm 0.047$ and $S = 2.204 \pm 0.047$ for the two entangled atom-atom states which rules out the possibility that the experiment can be explained by an LHV-theory with a p-value of 1.739×10^{-10}. The significance of the experiment is therefore very high, making our experiment an important contribution to the history of Bell tests.

7. Summary and Outlook

This work presented experiments on long-distance atom-photon and atom-atom entanglement with neutral $^{87}\mathrm{Rb}$-atoms. Atom-photon entanglement is generated in a spontaneous emission process that entangles the polarization state of the emitted photon with the Zeeman state of the atom. In a first experiment we used the atom-photon pair to teleport the polarization state of an attenuated laser pulse onto the atom over a distance of $20\,\mathrm{m}$. The crucial Bell-state projection of photons emitted by the atom and photons of the laser pulse requires a high overlap of the photonic wave functions. In particular the temporal shape and the central frequency of the laser pulse have to be adjusted with high precision. Besides that, an analysis of the Poissonian photon statistics of an attenuated laser pulse leads to a criterion for the required attenuation to achieve a high fidelity of the teleported state. Although this criterion reduces the achievable event rate to less than 1 event per minute, it enables the teleportation of an arbitrary polarization state and proved the possibility to use a laser source for quantum teleportation. We measured density matrices for different input states and obtained fidelities exceeding 0.76 for every teleported state.

Additionally, atom-photon entanglement provides the possibility to generate atom-atom entanglement. This is done using the entanglement swapping protocol. Therefore, two independent atom traps are operated at a certain distance and atom-photon entanglement is generated in each of them. The photons are overlapped at a beam splitter and projected onto a Bell-state to transfer the entanglement onto the atoms. In this work, the distance of the atom traps was increased from initially $20\,\mathrm{m}$ to $398\,\mathrm{m}$ which was necessary to be able to perform space-like separated measurements on the atoms. Improvements of the setup and the experimental sequence allowed a sufficient event rate of about 2 events per minute.

A consequence of the long distance between the atom traps is that there are mandatory time delays for both trap setups between the generation of atom-photon entanglement and the atomic state measurement. Thus, longer coherence times are necessary to be able to measure the atomic state with a time delay on the order of $10\,\mu\mathrm{s}$. To achieve this, we worked on the compensation and stabilization of magnetic fields to reduce energy shifts due to the Zeeman effect leading to a time evolution of atomic states. Major improvements of the long-term stability of a magnetic field sensor were necessary. Besides magnetic fields the light of the dipole trap induces an AC-Stark shift of the atomic states. In the case of elliptical polarization this shift is state dependent and leads (like the Zeeman shift) to a time evolution of atomic states. This is especially relevant, because the focused dipole trap beam always has elliptical polarization around the focal region and the spin-states of atoms moving in the trap potential show dephasing. A study of this process allowed us to find times when the atomic states rephase and this problem could be avoided. Altogether we could reach visibilities of more than $V = 0.9$ in time delayed atom-photon correlation measurements which provides the basis for high fidelity atom-atom experiments over long distances.

The generation of long-distance atom-atom entanglement together with the efficient and reliable analysis of the atomic states allowed us to violate Bell's inequality with both the detection efficiency and the locality loophole closed. The detection efficiency loophole is closed by employment of the event-ready scheme providing a signal on the availability of an entangled atom-atom state. Thus, whenever the atomic states are requested the system gives an answer corresponding to a detection efficiency of 1 in the context of a Bell experiment. The locality loophole is closed by applying a fast state measurement scheme that enables the analysis of both atomic states within $1093\,\mathrm{ns}$. Due to the long distance between the two atom traps of $398\,\mathrm{m}$, the propagation of any signal at the speed of light between the two laboratories takes at least $267.4\,\mathrm{ns}$ longer than the overall measurement time. In an experiment with significant statistics of 10000 events, a (combined) S-parameter of $S = 2.222 \pm 0.033$ was reached, resulting in a violation of the LHV limit by 6.7 standard deviations. This provides a very strong evidence against local-realism as a valid description of nature.

The experiment provides several opportunities for future work. Currently an upgrade of the confocal microscope is performed. The microscope objective is replaced with a high NA objective that will increase the collection efficiency of photons. This will allow higher event rates that, besides the reduction of the time needed for an experimental run, will also reduce noise due to dark counts. Another advantage of the new microscope might be that the alignment of the vacuum cell can be improved and that the asymmetry of the dipole trap field as explained in chapter 5.2.4 can be reduced.

A next milestone of the project will be the implementation of a device-independent quantum key distribution (DIQKD) protocol [28, 29, 30]. DIQKD has essential advantages compared to common QKD protocols, because the security is based on fewer assumptions. In particular, there are only basic assumptions regarding the measurement devices that, in principle, could be under the control of an eavesdropper. The security of these protocols relies on a rigorous violation of Bell's inequality, i.e. with all loopholes closed. Therefore, our experiment fulfills the mandatory requirements which rises the ambitions to achieve this next step. However, the criteria to implement such a protocol are quite harsh. To be immune against all collective attacks, the system must be able to violate Bell's inequality with an S-parameter of $S > 2.43$ to be able to extract a secret key [28]. Thus, the performance of the experiment has to be further improved.

Another planned project is the implementation of telecom conversion technologies. The emitted photons have a wavelength of $780\,\mathrm{nm}$ which is not optimal for long distance communication regarding the damping in optical fibers. Currently the photon loss is $4.0\,\mathrm{dB/km}$ corresponding to $48\,\%$ in the $700\,\mathrm{m}$ long fiber. A further increase of the distance between the atom traps therefore is limited, unless the photons are converted into the telecom bands. Frequency conversion of single photons is possible using three-wave-mixing and four-wave-mixing techniques in nonlinear crystals [88]. Experiments already demonstrated the conversion of visible and near infrared photons into the telecom range. Important properties of the single photons like the coherence times and the photon anti-bunching [89] as well as time-energy entanglement of an entangled photon pair [90] are preserved during this process. In the near future, further development will allow for conversion that also preserves the polarization state of the converted photon. This can then be used to generate atom-photon entanglement with a telecom photon and consequently atom-atom entanglement over much longer distances.

A. Physical constants and abbreviations

constant	description	value
$\hbar = \frac{h}{2\pi}$	reduced Planck constant	$1.054571726 \cdot 10^{-34}\,\mathrm{J \cdot s}$
c	speed of light in vacuum	$2.99792458 \cdot 10^{8}\,{}^{m}/_{\mathrm{s}}$
μ_0	permeability of free space	$1.25663770614 \cdot 10^{-6}\,{}^{N}/_{\mathrm{A}^2}$
$\epsilon_0 = \frac{1}{c^2\mu_0}$	permittivity of free space	$8.8541878176 \cdot 10^{-12}\,{}^{F}/_{\mathrm{m}}$
e	elementary charge	$1.602176565 \cdot 10^{-19}\,\mathrm{C}$
u	atomic mass unit	$1.660538921 \cdot 10^{-27}\,\mathrm{kg}$
k_B	Boltzmann constant	$1.38064852 \cdot 10^{-23}\,\frac{\mathrm{m^2 kg}}{\mathrm{s^2 K}}$
μ_B	Bohr magneton	$9.274009994 \cdot 10^{-24}\,{}^{J}/_{\mathrm{T}}$
$m_{^{87}Rb}$	mass	$86.90918020 \cdot u$
Γ_{D1}	decay rate of the $D1$ transition	$2\pi \cdot 5.7500\,\mathrm{MHz}$
Γ_{D2}	decay rate of the $D2$ transition	$2\pi \cdot 6.0666\,\mathrm{MHz}$
d_{D1}	dipole matrix element of the $D1$ transition	$2.53766 \cdot 10^{-29}\,\mathrm{C \cdot m}$
d_{D2}	dipole matrix element of the $D2$ transition	$3.58424 \cdot 10^{-29}\,\mathrm{C \cdot m}$

Table A.1.: Physical constants and properties of ^{87}Rb

LHV	local hidden variable	CEM	channel electron multiplier
DI	device independent	HWP	half-wave plate
QKD	quantum key distribution	QWP	quarter-wave plate
AOM	acousto-optical modulator	ND	neutral density (filter)
UHV	ultra-high vacuum	AWG	arbitrary waveform generator
ODT	optical dipole trap	QRNG	quantum random number generator
MOT	magneto-optical trap	CU	control unit
APD	avalanche photo diode	TDC	time-to-digital converter
BSM	Bell-state measurement	PMT	photo multiplier tube
(P)BS	(polarizing) beam splitter	EOM	electro-optical modulator

Table A.2.: Abbreviations

B. Laser system and transition frequencies

The atomic quantum system is controlled and manipulated by different laser beams with frequencies matching the atomic transitions (figure B.1). Each of these beams is obtained from one of three diode lasers that are frequency stabilized using Doppler-free saturation spectroscopy:

- The "cooling" laser is used for transitions between the hyperfine level $5^2S_{1/2},\ F = 2$ and the hyperfine levels of $5^2P_{3/2}$.
- The "repump" laser is used for transitions between the hyperfine level $5^2S_{1/2},\ F = 1$ and the hyperfine levels of $5^2P_{3/2}$.
- The "readout" laser is resonant to the transition $5^2S_{1/2},\ F = 1 \rightarrow 5^2P_{1/2},\ F' = 1$

The cooling and repump beams are then split into several beams by polarizing beam splitters (PBS). A half-wave plate in front of every PBS allows us to set the relative power ratio of the beams. The frequency is then fine-tuned to match the atomic transition frequency by acousto-optic modulators that are also used to switch the beams on and off and fine-tune the optical power. The derived beams and their labeling is shown in figure B.1. The extracted transitions of the cooling laser are:

- cooling: For laser cooling of atoms
- cycling: To excite and remove atoms from the $F = 2$ ground level
- pump2-1: Used for state preparation

The repump laser is also split into three beams for the transitions:

- repump: To maintain the cooling cycles
- excitation: To generate atom-photon entanglement
- pump1-1: Used for state preparation

In addition to the frequency stabilized transitions there are two free running laser diodes, the optical dipole trap laser (ODT) at a wavelength of $852\,\mathrm{nm}$ and the ionization laser at a wavelength of $473\,\mathrm{nm}$.

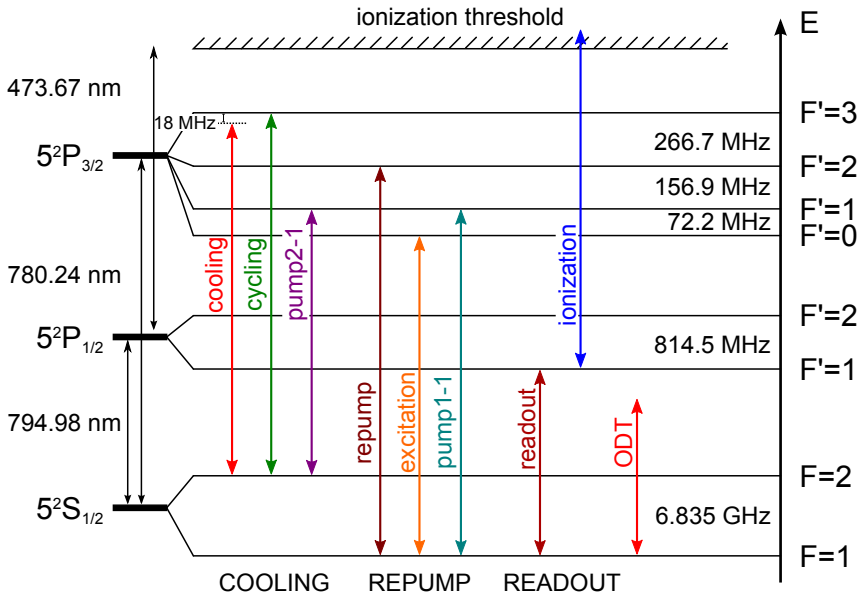

Figure B.1.: Laser frequencies and their labeling as used in the experiment.

C. Photonic and atomic measurement bases

Measurements on the photons and atoms are performed in different measurement bases depending on the requirements. Thus, a consistent definition of the bases, their eigenstates and transformations is needed. The quantization axis of the atom is defined as the direction in which the emitted photons are collected. In the laboratory frame this axis is referred to as z -axis. The spin orientation of atoms (in the ground level $F = 1$) is the projection of the spin on the quantization axis with the possible quantum numbers $m_F = 0, \pm 1$. In the qubit system the states are referred to as $|m_F = +1\rangle_z = |\uparrow\rangle_z$ and $|m_F = -1\rangle_z = |\downarrow\rangle_z$.

Photon polarizations

The polarization of photons in the reference frame of the atom is defined in the following way. When a photon is absorbed by the atom the angular momentum of the system "photon + atom" has to be preserved. If the photon is σ^+-polarized the projection of the atomic spin changes by a value $\triangle m_F = +1$. A σ^--polarized photon causes a change of the spin projection by $\triangle m_F = -1$ [91] and a π-polarized photon does not change the projection of the spin. In the laboratory frame, the polarization of photons with a wave vector $\vec{k}$ along the quantization axis is σ^+ if the photon is left circularly polarized and σ^- in the case of right circular polarization [41]. The polarization states are thus defined as

$$\begin{aligned} |L\rangle &\hat{=} \sigma^+, \\ |R\rangle &\hat{=} \sigma^-, \end{aligned} \tag{C.1}$$

which holds for both photons from the readout beam and photons emitted by the atom in a spontaneous decay, since the readout pulse is applied in the direction of the z-axis as well as the emitted photons are collected along this direction. The polarization state of photons can be transformed into different bases with the relations according to reference [41]:

$$
\begin{aligned}
|H\rangle &= \frac{1}{\sqrt{2}}\left(|L\rangle + |R\rangle\right), \\
|V\rangle &= \frac{i}{\sqrt{2}}\left(|L\rangle - |R\rangle\right), \\
|+\rangle &= \frac{1}{\sqrt{2}}e^{i\frac{\pi}{4}}\left(|L\rangle - i|R\rangle\right), \\
|-\rangle &= \frac{-1}{\sqrt{2}}e^{-i\frac{\pi}{4}}\left(|L\rangle + i|R\rangle\right)
\end{aligned}
\tag{C.2}
$$

Atomic measurement basis

The measurements on the atomic qubit are performed in a measurement basis selected by the polarization of the readout pulse. We define three sets of basis vectors $\{|\uparrow\rangle_x, |\downarrow\rangle_x\}$, $\{|\uparrow\rangle_y, |\downarrow\rangle_y\}$ and $\{|\uparrow\rangle_z, |\downarrow\rangle_z\}$ which are eigenvectors to the Pauli-operators $\hat{\sigma}_x$, $\hat{\sigma}_y$ and $\hat{\sigma}_z$, respectively. Transformations between the bases are executed according to [41]

$$
\begin{aligned}
|\uparrow\rangle_x &= \frac{1}{\sqrt{2}}\left(|\uparrow\rangle_z + |\downarrow\rangle_z\right), \\
|\downarrow\rangle_x &= \frac{i}{\sqrt{2}}\left(|\uparrow\rangle_z - |\downarrow\rangle_z\right), \\
|\uparrow\rangle_y &= \frac{1}{\sqrt{2}}e^{i\frac{\pi}{4}}\left(|\uparrow\rangle_z - i\,|\downarrow\rangle_z\right), \\
|\downarrow\rangle_y &= \frac{-1}{\sqrt{2}}e^{-i\frac{\pi}{4}}\left(|\uparrow\rangle_z + i\,|\downarrow\rangle_z\right).
\end{aligned}
\tag{C.3}
$$

The selection rules for the state-selective excitation is derived from the dipole matrix elements (Clebsch-Gordan (CG) coefficients) for transitions between the states $5^2S_{1/2}$, $F = 1$, $m_F = \pm 1$ and $5^2P_{1/2}$, $F' = 1$, $m_{F'} = 0$. The ground state $|m_F = -1\rangle_z$ is a dark state for a σ^+-polarized readout pulse, whereas $|m_F = +1\rangle_z$ is a dark state for a σ^--polarized readout pulse. Due to the different signs of the CG coefficients for σ^+ and σ^- transitions, a superposition of both polarizations $\cos(\alpha')\sigma^- + e^{i\phi'}\sin(\alpha')\sigma^+$ results in an atomic dark state [40]

$$
|\Psi\rangle_{\mathrm{D}} = \cos(\alpha')\,|\downarrow\rangle_z + e^{i\phi'}\sin(\alpha')\,|\uparrow\rangle_z\,. \tag{C.4}
$$

In the presented experiments the readout polarization is typically linear. Therefore, it is useful to transform the criterion for a dark state into another basis (with equations C.2 and C.3) which results in equation 2.6 presented in the main text.

Entangled atom-photon state

Using the relations in equation C.2 and C.3 allows to transform the entangled atom-photon state into different bases. The state transforms according to

$$\begin{aligned} |\Psi\rangle_{\mathrm{AP}} &= \frac{1}{\sqrt{2}}\left(|\uparrow\rangle_z |R\rangle + |\downarrow\rangle_z |L\rangle\right) \\ &= \frac{1}{\sqrt{2}}\left(|\uparrow\rangle_x |H\rangle + |\downarrow\rangle_x |V\rangle\right) \\ &= \frac{1}{\sqrt{2}}\left(|\,|\uparrow\rangle_y |-\rangle + |\downarrow\rangle_y |+\rangle\right), \end{aligned} \tag{C.5}$$

which agrees with the basic property of entanglement that the transformation into a different basis maintains the entanglement.

D. Quantum teleportation scheme

I will present the calculations necessary to determine the expected atomic state after the teleportation of an arbitrary input state $|\Psi\rangle_{\mathrm{I}} = \beta|L\rangle + \gamma|R\rangle$. The three-particle state is the product of the input state and the entangled atom-photon state $|\Psi\rangle_{\mathrm{AP}} = \frac{1}{\sqrt{2}}\left(|\uparrow\rangle_z |R\rangle + |\downarrow\rangle_z |L\rangle\right)$ (see equation 2.3) yielding

$$|\Psi\rangle_{\mathrm{I}} \otimes |\Psi\rangle_{\mathrm{AP}} = (\beta|L\rangle + \gamma|R\rangle)_{\mathrm{I}} \otimes \frac{1}{\sqrt{2}}\left(|\uparrow\rangle_z |R\rangle + |\downarrow\rangle_z |L\rangle\right)_{\mathrm{AP}}. \tag{D.1}$$

The Bell-state measurement of photons is performed in the H/V-basis. It is thus convenient to transform the photon states into this basis according to the relations in the previous section $|R\rangle = \frac{1}{\sqrt{2}}\left(|H\rangle + i|V\rangle\right)$ and $|L\rangle = \frac{1}{\sqrt{2}}\left(|H\rangle - i|V\rangle\right)$:

$$\begin{aligned} |\Psi\rangle_{\mathrm{I}} \otimes |\Psi\rangle_{\mathrm{AP}} &= \frac{1}{\sqrt{2}}\left(\beta\left(|H\rangle_{\mathrm{I}} - i|V\rangle_{\mathrm{I}}\right) + \gamma\left(|H\rangle_{\mathrm{I}} + i|V\rangle_{\mathrm{I}}\right)\right)_{\mathrm{I}} \\ &\otimes \frac{1}{\sqrt{2}}\left(|\uparrow\rangle_x |H\rangle_{\mathrm{P}} + |\downarrow\rangle_x |V\rangle_{\mathrm{P}}\right)_{\mathrm{AP}} \end{aligned} \tag{D.2}$$

The term is then rearranged to

$$\begin{aligned} |\Psi\rangle_{\mathrm{I}} \otimes |\Psi\rangle_{\mathrm{AP}} &= \frac{1}{2}\beta\left(|H\rangle_{\mathrm{I}}|H\rangle_{\mathrm{P}} |\uparrow\rangle_x - i|V\rangle_{\mathrm{I}}|H\rangle_{\mathrm{P}} |\uparrow\rangle_x\right) \\ &+ \frac{1}{2}\gamma\left(|H\rangle_{\mathrm{I}}|H\rangle_{\mathrm{P}} |\uparrow\rangle_x + i|V\rangle_{\mathrm{I}}|H\rangle_{\mathrm{P}} |\uparrow\rangle_x\right) \\ &+ \frac{1}{2}\beta\left(|H\rangle_{\mathrm{I}}|V\rangle_{\mathrm{P}} |\downarrow\rangle_x - i|V\rangle_{\mathrm{I}}|V\rangle_{\mathrm{P}} |\downarrow\rangle_x\right) \\ &+ \frac{1}{2}\gamma\left(|H\rangle_{\mathrm{I}}|V\rangle_{\mathrm{P}} |\downarrow\rangle_x + i|V\rangle_{\mathrm{I}}|V\rangle_{\mathrm{P}} |\downarrow\rangle_x\right) \end{aligned} \tag{D.3}$$

$$\begin{aligned} &= \frac{1}{2}|H\rangle_{\mathrm{I}}|H\rangle_{\mathrm{P}} \otimes (\beta + \gamma) |\uparrow\rangle_x \\ &+ \frac{1}{2}|V\rangle_{\mathrm{I}}|V\rangle_{\mathrm{P}} \otimes (-i\beta + i\gamma) |\downarrow\rangle_x \\ &+ \frac{1}{2}|H\rangle_{\mathrm{I}}|V\rangle_{\mathrm{P}} \otimes (\beta + \gamma) |\downarrow\rangle_x \\ &+ \frac{1}{2}|V\rangle_{\mathrm{I}}|H\rangle_{\mathrm{P}} \otimes (-i\beta + i\gamma) |\uparrow\rangle_x . \end{aligned} \tag{D.4}$$

The photons are projected onto one out of four maximally entangled Bell-states

$$\begin{aligned} |\Psi^{\pm}\rangle &= \frac{1}{\sqrt{2}}\left(|H\rangle|V\rangle \pm |V\rangle|H\rangle\right)_{\mathrm{IP}}, \\ |\Phi^{\pm}\rangle &= \frac{1}{\sqrt{2}}\left(|H\rangle|H\rangle \pm |V\rangle|V\rangle\right)_{\mathrm{IP}}. \end{aligned} \tag{D.5}$$

This measurement projects the atoms onto a defined state depending on the result of the BSM, which is:

$$\begin{aligned} {}_{\mathrm{IP}}\langle\Psi^{-}||\Psi\rangle_{\mathrm{I}} \otimes |\Psi\rangle_{\mathrm{AP}} &= \frac{1}{\sqrt{2}}\left((\beta+\gamma)\,|\downarrow\rangle_x - (-i\beta+i\gamma)\,|\uparrow\rangle_x\right)_{\mathrm{A}}, \\ {}_{\mathrm{IP}}\langle\Psi^{+}||\Psi\rangle_{\mathrm{I}} \otimes |\Psi\rangle_{\mathrm{AP}} &= \frac{1}{\sqrt{2}}\left((\beta+\gamma)\,|\downarrow\rangle_x + (-i\beta+i\gamma)\,|\uparrow\rangle_x\right)_{\mathrm{A}}, \\ {}_{\mathrm{IP}}\langle\Phi^{-}||\Psi\rangle_{\mathrm{I}} \otimes |\Psi\rangle_{\mathrm{AP}} &= \frac{1}{\sqrt{2}}\left((\beta+\gamma)\,|\uparrow\rangle_x - (-i\beta+i\gamma)\,|\downarrow\rangle_x\right)_{\mathrm{A}}, \\ {}_{\mathrm{IP}}\langle\Phi^{+}||\Psi\rangle_{\mathrm{I}} \otimes |\Psi\rangle_{\mathrm{AP}} &= \frac{1}{\sqrt{2}}\left((\beta+\gamma)\,|\uparrow\rangle_x + (-i\beta+i\gamma)\,|\downarrow\rangle_x\right)_{\mathrm{A}} \end{aligned} \tag{D.6}$$

The Bell-states form a complete basis of the two-photon Hilbert space. The final state of all three particles is thus the sum of the Bell-states times the respective projection of the atom. The final state is then obtained by transforming the atomic states back to the $|\uparrow\rangle_z$, $|\downarrow\rangle_z$ basis and simplifying the different terms:

$$\begin{aligned} |\Psi\rangle_{\mathrm{I}} \otimes |\Psi\rangle_{\mathrm{AP}} = {} & \frac{i}{2\sqrt{2}}\left(|H\rangle|V\rangle - |V\rangle|H\rangle\right)_{\mathrm{IP}} \otimes \left(\beta\,|\uparrow\rangle_z - \gamma\,|\downarrow\rangle_z\right)_{\mathrm{A}} \\ & + \frac{i}{2\sqrt{2}}\left(|H\rangle|V\rangle + |V\rangle|H\rangle\right)_{\mathrm{IP}} \otimes \left(\gamma\,|\uparrow\rangle_z - \beta\,|\downarrow\rangle_z\right)_{\mathrm{A}} \\ & + \frac{1}{2\sqrt{2}}\left(|H\rangle|H\rangle - |V\rangle|V\rangle\right)_{\mathrm{IP}} \otimes \left(\gamma\,|\uparrow\rangle_z + \beta\,|\downarrow\rangle_z\right)_{\mathrm{A}} \\ & + \frac{1}{2\sqrt{2}}\left(|H\rangle|H\rangle + |V\rangle|V\rangle\right)_{\mathrm{IP}} \otimes \left(\beta\,|\uparrow\rangle_z + \gamma\,|\downarrow\rangle_z\right)_{\mathrm{A}} \end{aligned} \tag{D.7}$$

E. Calculation of the magnetic field generated by the MOT coils

A numerical calculation of the magnetic field generated by the MOT coils is evaluated with Mathematica using the Biot-Savart law for a single circular wire of radius R with a current I. The center of the coordinate system is the position of the atom, the coils (in an anti-Helmholtz configuration) are displaced along the y-axis by $\pm a$ and each coil consists of N windings. The resulting magnetic field of one wire is

$$\begin{aligned} \vec{B}_{\text{wire}}(\vec{r}) &= \frac{\mu_0 I}{4\pi} \int d\vec{r'} \times \frac{\vec{r} - \vec{r'}}{\left|\vec{r} - \vec{r'}\right|^3} \\ &= \frac{\mu_0 I}{4\pi} \int R d\theta \begin{pmatrix} \cos(\theta) \\ 0 \\ -\sin(\theta) \end{pmatrix} \times \frac{\vec{r} - \vec{r'}}{\left|\vec{r} - \vec{r'}\right|^3}, \end{aligned} \tag{E.1}$$

with the integral being a line integration along the wire and the coordinates $\vec{r} = (x,\, y,\, z)$ and $\vec{r'} = (R\sin(\theta),\, a,\, R\cos(\theta))$. The magnetic field of the second coil is obtained by replacing $I \to -I$ and $a \to -a$ in equation E.1 and the overall magnetic field is calculated by adding all windings of both coils.

The parameters of the MOT coils for trap 1 and trap 2, the corresponding positions of the magneto resistive sensors and the resulting magnetic field vectors at these positions are summarized in table E.1. The parameter that describes the confinement of the MOT is the gradient of the field along the axis of the coils which is in our setup $\frac{dB_y}{dy}$. The design of the coils and the current are chosen with the aim to achieve a high loading rate of atoms. This is obtained for gradients of about $10\,\frac{\text{G}}{\text{cm}}$ at the center. The resulting magnetic field for the sensor is $26.25\,\text{G}$ and $40.92\,\text{G}$ for the two trap setups, respectively, with the dominant field component pointing in the y-direction.

a) MOT coil configuration

	R	a	N	I	$\frac{dB_y}{dy}$
trap 1	$40\,\mathrm{mm}$	$35\,\mathrm{mm}$	140	$1.6\,\mathrm{A}$	$11.15\,\frac{\mathrm{G}}{\mathrm{cm}}$
trap 2	$40\,\mathrm{mm}$	$35\,\mathrm{mm}$	140	$1.8\,\mathrm{A}$	$12.54\,\frac{\mathrm{G}}{\mathrm{cm}}$

b) sensor position (relative to the center of the coils)

	x	y	z
trap 1	$-1\,\mathrm{mm}$	$18.5\,\mathrm{mm}$	$-14\,\mathrm{mm}$
trap 2	$-12.5\,\mathrm{mm}$	$30\,\mathrm{mm}$	$-2\,\mathrm{mm}$

c) magnetic field at sensor position

	$\lvert B_x\rvert$	$\lvert B_y\rvert$	$\lvert B_z\rvert$
trap 1	$0.55\,\mathrm{G}$	$25.10\,\mathrm{G}$	$7.68\,\mathrm{G}$
trap 2	$3.84\,\mathrm{G}$	$40.73\,\mathrm{G}$	$0.61\,\mathrm{G}$

Table E.1.: a) Parameters of the MOT coils and b) the position of the magneto-resistive sensors for both trap setups. c) Calculated magnetic field at the position of the sensors.

Bibliography

[1] A. Einstein, B. Podolsky, and N. Rosen. *Can Quantum-Mechanical Description of Physical Reality Be Considered Complete?* Phys. Rev., **47**, 777–780, May 1935.

[2] J. Bell. *On the Einstein-Podolsky-Rosen paradox*. Physics, **1** (3), 195–200, 1964.

[3] J. F. Clauser, M. A. Horne, A. Shimony, and R. A. Holt. *Proposed Experiment to Test Local Hidden-Variable Theories*. Phys. Rev. Lett., **23**, 880–884, Oct 1969.

[4] S. J. Freedman and J. F. Clauser. *Experimental Test of Local Hidden-Variable Theories*. Phys. Rev. Lett., **28**, 938–941, Apr 1972.

[5] A. Aspect, P. Grangier, and G. Roger. *Experimental Tests of Realistic Local Theories via Bell's Theorem*. Phys. Rev. Lett., **47**, 460–463, Aug 1981.

[6] A. Aspect, P. Grangier, and G. Roger. *Experimental Realization of Einstein-Podolsky-Rosen-Bohm Gedankenexperiment : A New Violation of Bell's Inequalities*. Phys. Rev. Lett., **49**, 91–94, Jul 1982.

[7] G. Weihs, T. Jennewein, C. Simon, H. Weinfurter, and A. Zeilinger. *Violation of Bell's Inequality under Strict Einstein Locality Conditions*. Phys. Rev. Lett., **81**, 5039–5043, Dec 1998.

[8] M. A. Rowe, D. Kielpinski, V. Meyer, C. A. Sackett, W. M. Itano, C. Monroe, and D. J. Wineland. *Experimental violation of a Bell's inequality with efficient detection*. Nature, **409** (6822), 791–794, February 2001.

[9] B. G. Christensen, K. T. McCusker, J. B. Altepeter, B. Calkins, T. Gerrits, A. E. Lita, A. Miller, L. K. Shalm, Y. Zhang, S. W. Nam, N. Brunner, C. C. W. Lim, N. Gisin, and P. G. Kwiat. *Detection-Loophole-Free Test of Quantum Nonlocality, and Applications*. Phys. Rev. Lett., **111**, 130406, Sep 2013.

[10] M. Giustina, A. Mech, S. Ramelow, B. Wittmann, J. Kofler, J. Beyer, A. Lita, B. Calkins, T. Gerrits, S. W. Nam, R. Ursin, and A. Zeilinger. *Bell violation using entangled photons without the fair-sampling assumption*. Nature, **497** (7448), 227–230, May 2013.

[11] B. Hensen, H. Bernien, A. E. Dreau, A. Reiserer, N. Kalb, M. S. Blok, J. Ruitenberg, R. F. L. Vermeulen, R. N. Schouten, C. Abellan, W. Amaya, V. Pruneri, M. W. Mitchell, M. Markham, D. J. Twitchen, D. Elkouss, S. Wehner, T. H. Taminiau, and R. Hanson. *Loophole-free Bell inequality violation using electron spins separated by 1.3 kilometres*. Nature, **526** (7575), 682–686, October 2015.

[12] B. Hensen, N. Kalb, M. Blok, A. Dréau, A. Reiserer, R. Vermeulen, R. Schouten, M. Markham, D. Twitchen, K. Goodenough, D. Elkouss, S. Wehner, T. Taminiau, and R. Hanson. *Loophole-free Bell test using electron spins in diamond: second experiment and additional analysis*. arXiv:1603.05705v2, 2016.

[13] M. Giustina, M. A. M. Versteegh, S. Wengerowsky, J. Handsteiner, A. Hochrainer, K. Phelan, F. Steinlechner, J. Kofler, J.-A. Larsson, C. Abellán, W. Amaya, V. Pruneri, M. W. Mitchell, J. Beyer, T. Gerrits, A. E. Lita, L. K. Shalm, S. W. Nam, T. Scheidl, R. Ursin, B. Wittmann, and A. Zeilinger. *Significant-Loophole-Free Test of Bell's Theorem with Entangled Photons*. Phys. Rev. Lett., **115**, 250401, Dec 2015.

[14] L. K. Shalm, E. Meyer-Scott, B. G. Christensen, P. Bierhorst, M. A. Wayne, M. J. Stevens, T. Gerrits, S. Glancy, D. R. Hamel, M. S. Allman, K. J. Coakley, S. D. Dyer, C. Hodge, A. E. Lita, V. B. Verma, C. Lambrocco, E. Tortorici, A. L. Migdall, Y. Zhang, D. R. Kumor, W. H. Farr, F. Marsili, M. D. Shaw, J. A. Stern, C. Abellán, W. Amaya, V. Pruneri, T. Jennewein, M. W. Mitchell, P. G. Kwiat, J. C. Bienfang, R. P. Mirin, E. Knill, and S. W. Nam. *Strong Loophole-Free Test of Local Realism*. Phys. Rev. Lett., **115**, 250402, Dec 2015.

[15] W. Rosenfeld, D. Burchardt, R. Garthoff, K. Redeker, N. Ortegel, M. Rau, and H. Weinfurter. *Event-Ready Bell Test Using Entangled Atoms Simultaneously Closing Detection and Locality Loopholes*. Phys. Rev. Lett., **119** (1), 010402–, July 2017.

[16] H. Fürst, H. Weier, S. Nauerth, D. G. Marangon, C. Kurtsiefer, and H. Weinfurter. *High speed optical quantum random number generation*. Opt. Express, **18** (12), 13029–13037, 2010.

[17] C. Abellán, W. Amaya, D. Mitrani, V. Pruneri, and M. W. Mitchell. *Generation of Fresh and Pure Random Numbers for Loophole-Free Bell Tests*. Phys. Rev. Lett., **115** (25), 250403–, Dec 2015.

[18] J. Handsteiner, A. S. Friedman, D. Rauch, J. Gallicchio, B. Liu, H. Hosp, J. Kofler, D. Bricher, M. Fink, C. Leung, A. Mark, H. T. Nguyen, I. Sanders, F. Steinlechner, R. Ursin, S. Wengerowsky, A. H. Guth, D. I. Kaiser, T. Scheidl, and A. Zeilinger. *Cosmic Bell Test: Measurement Settings from Milky Way Stars*. Phys. Rev. Lett., **118** (6), 060401–, February 2017.

[19] C. A. Kocher and E. D. Commins. *Polarization Correlation of Photons Emitted in an Atomic Cascade*. Phys. Rev. Lett., **18** (15), 575–577, April 1967.

[20] B. B. Blinov, D. L. Moehring, L.-M. Duan, and C. Monroe. *Observation of entanglement between a single trapped atom and a single photon*. Nature, **428** (6979), 153–157, March 2004.

[21] J. Volz, M. Weber, D. Schlenk, W. Rosenfeld, J. Vrana, K. Saucke, C. Kurtsiefer, and H. Weinfurter. *Observation of Entanglement of a Single Photon with a Trapped Atom*. Phys. Rev. Lett., **96**, 030404, Jan 2006.

[22] T. Wilk, S. C. Webster, A. Kuhn, and G. Rempe. *Single-Atom Single-Photon Quantum Interface*. Science, **317** (5837), 488–490, 2007.

[23] S. Ritter, C. Nolleke, C. Hahn, A. Reiserer, A. Neuzner, M. Uphoff, M. Mucke, E. Figueroa, J. Bochmann, and G. Rempe. *An elementary quantum network of single atoms in optical cavities*. Nature, **484** (7393), 195–200, April 2012.

[24] M. Żukowski, A. Zeilinger, M. A. Horne, and A. K. Ekert. *"Event-ready-detectors" Bell experiment via entanglement swapping*. Phys. Rev. Lett., **71**, 4287–4290, Dec 1993.

[25] J. Hofmann, M. Krug, N. Ortegel, L. Gérard, M. Weber, W. Rosenfeld, and H. Weinfurter. *Heralded Entanglement Between Widely Separated Atoms*. Science, **337** (6090), 72–75, 2012.

[26] H. Bernien, B. Hensen, W. Pfaff, G. Koolstra, M. S. Blok, L. Robledo, T. H. Taminiau, M. Markham, D. J. Twitchen, L. Childress, and R. Hanson. *Heralded entanglement between solid-state qubits separated by three metres*. Nature, **497** (7447), 86–90, May 2013.

[27] A. K. Ekert. *Quantum cryptography based on Bell's theorem*. Phys. Rev. Lett., **67**, 661–663, Aug 1991.

[28] A. Acín, N. Brunner, N. Gisin, S. Massar, S. Pironio, and V. Scarani. *Device-Independent Security of Quantum Cryptography against Collective Attacks*. Phys. Rev. Lett., **98**, 230501, Jun 2007.

[29] U. Vazirani and T. Vidick. *Fully Device-Independent Quantum Key Distribution*. Phys. Rev. Lett., **113**, 140501, Sep 2014.

[30] E. A. Aguilar, R. Ramanathan, J. Kofler, and M. Pawłowski. *Completely device-independent quantum key distribution*. Phys. Rev. A, **94** (2), 022305–, Aug 2016.

[31] C. H. Bennett, G. Brassard, C. Crépeau, R. Jozsa, A. Peres, and W. K. Wootters. *Teleporting an unknown quantum state via dual classical and Einstein-Podolsky-Rosen channels*. Phys. Rev. Lett., **70**, 1895–1899, Mar 1993.

[32] S. Pirandola, J. Eisert, C. Weedbrook, A. Furusawa, and S. L. Braunstein. *Advances in quantum teleportation*. Nat Photon, **9** (10), 641–652, October 2015.

[33] X.-L. Wang, X.-D. Cai, Z.-E. Su, M.-C. Chen, D. Wu, L. Li, N.-L. Liu, C.-Y. Lu, and J.-W. Pan. *Quantum teleportation of multiple degrees of freedom of a single photon*. Nature, **518** (7540), 516–519, February 2015.

[34] X.-S. Ma, T. Herbst, T. Scheidl, D. Wang, S. Kropatschek, W. Naylor, B. Wittmann, A. Mech, J. Kofler, E. Anisimova, V. Makarov, T. Jennewein, R. Ursin, and A. Zeilinger. *Quantum teleportation over 143 kilometres using active feed-forward*. Nature, **489** (7415), 269–273, September 2012.

[35] R. Valivarthi, M. G. Puigibert, Q. Zhou, G. H. Aguilar, V. B. Verma, F. Marsili, M. D. Shaw, S. W. Nam, D. Oblak, and W. Tittel. *Quantum teleportation across a metropolitan fibre network*. Nat Photon, **10** (10), 676–680, October 2016.

[36] J.-G. Ren, P. Xu, H.-L. Yong, L. Zhang, S.-K. Liao, J. Yin, W.-Y. Liu, W.-Q. Cai, M. Yang, L. Li, K.-X. Yang, X. Han, Y.-Q. Yao, J. Li, H.-Y. Wu, S. Wan, L. Liu, D.-Q. Liu, Y.-W. Kuang, Z.-P. He, P. Shang, C. Guo, R.-H. Zheng, K. Tian, Z.-C. Zhu, N.-L. Liu, C.-Y. Lu, R. Shu, Y.-A. Chen, C.-Z. Peng, J.-Y. Wang, and J.-W. Pan. *Ground-to-satellite quantum teleportation*. arXiv:1707.00934, 2017.

[37] N. Sangouard, C. Simon, H. de Riedmatten, and N. Gisin. *Quantum repeaters based on atomic ensembles and linear optics*. Rev. Mod. Phys., **83** (1), 33–80, March 2011.

[38] H. J. Kimble. *The quantum internet*. Nature, **453** (7198), 1023–1030, June 2008.

[39] M. Weber. *Quantum optical experiments towards atom-photon entanglement*. PhD thesis, Ludwig-Maximilians-Universität München, 2005.

[40] J. Volz. *Atom-Photon Entanglement*. PhD thesis, Ludwig-Maximilians-Universität München, Juli 2006.

[41] W. Rosenfeld. *Experiments with an Entangled System of a Single Atom and a Single Photon*. PhD thesis, Ludwig-Maximilians-Universität München, November 2008.

[42] F. Henkel. *Photoionisation detection of single ^{87}Rb-atoms using channel electron multipliers*. PhD thesis, Ludwig-Maximilians-Universität München, November 2011.

[43] J. Hofmann. *Heralded Atom-Atom Entanglement*. PhD thesis, Ludwig-Maximilians-Universität München, 2014.

[44] M. Krug. *Title to be announced*. PhD thesis, Ludwig-Maximilians-Universität München.

[45] N. Ortegel. *State readout of single Rubidium-87 atoms for a loophole-free test of Bell's inequality*. PhD thesis, Ludwig-Maximilians-Universität München, 2016.

[46] D. A. Steck. *Rubidium 87 d line data*. http://steck.us/alkalidata/rubidium87numbers.pdf, version 2.1.5 from 5 January 2015.

[47] L. Ricci, M. Weidemüller, T. Esslinger, A. Hemmerich, C. Zimmermann, V. Vuletic, W. König, and T. W. Hänsch. *A compact grating-stabilized diode laser system for atomic physics*. Optics Communications, **117** (5), 541–549, 1995.

[48] M. Weber, J. Volz, K. Saucke, C. Kurtsiefer, and H. Weinfurter. *Analysis of a single-atom dipole trap*. Phys. Rev. A, **73**, 043406, Apr 2006.

[49] E. L. Raab, M. Prentiss, A. Cable, S. Chu, and D. E. Pritchard. *Trapping of Neutral Sodium Atoms with Radiation Pressure*. Phys. Rev. Lett., **59**, 2631–2634, Dec 1987.

[50] H. Metcalf and P. van der Straten. *Laser cooling and trapping*. Springer Verlag, New York, 1999.

[51] T. W. Hänsch and A. L. Schawlow. *Cooling of gases by laser radiation*. Optics Communications, **13** (1), 68 – 69, 1975.

[52] S. Chu, L. Hollberg, J. E. Bjorkholm, A. Cable, and A. Ashkin. *Three-dimensional viscous confinement and cooling of atoms by resonance radiation pressure*. Phys. Rev. Lett., **55** (1), 48–51, July 1985.

[53] J. Dalibard and C. Cohen-Tannoudji. *Laser cooling below the Doppler limit by polarization gradients: simple theoretical models*. J. Opt. Soc. Am. B, **6** (11), 2023–2045, Nov 1989.

[54] R. Grimm, M. Weidemüller, and Y. B. Ovchinnikov. *Optical dipole traps for neutral atoms*. arXiv:physics/9902072, 1999.

[55] N. Schlosser, G. Reymond, and P. Grangier. *Collisional Blockade in Microscopic Optical Dipole Traps*. Phys. Rev. Lett., **89**, 023005, Jun 2002.

[56] R. Gehr, J. Volz, G. Dubois, T. Steinmetz, Y. Colombe, B. L. Lev, R. Long, J. Estève, and J. Reichel. *Cavity-Based Single Atom Preparation and High-Fidelity Hyperfine State Readout*. Phys. Rev. Lett., **104** (20), 203602–, May 2010.

[57] J. Bochmann, M. Mücke, C. Guhl, S. Ritter, G. Rempe, and D. L. Moehring. *Lossless State Detection of Single Neutral Atoms*. Phys. Rev. Lett., **104** (20), 203601–, May 2010.

[58] F. Henkel, M. Krug, J. Hofmann, W. Rosenfeld, M. Weber, and H. Weinfurter. *Highly Efficient State-Selective Submicrosecond Photoionization Detection of Single Atoms*. Phys. Rev. Lett., **105**, 253001, Dec 2010.

[59] J.-W. Pan, D. Bouwmeester, H. Weinfurter, and A. Zeilinger. *Experimental Entanglement Swapping: Entangling Photons That Never Interacted*. Phys. Rev. Lett., **80**, 3891–3894, May 1998.

[60] C. K. Hong, Z. Y. Ou, and L. Mandel. *Measurement of subpicosecond time intervals between two photons by interference*. Phys. Rev. Lett., **59**, 2044–2046, Nov 1987.

[61] N. Lütkenhaus, J. Calsamiglia, and K.-A. Suominen. *Bell measurements for teleportation*. Phys. Rev. A, **59** (5), 3295–3300, May 1999.

[62] W. Rosenfeld, J. Hofmann, N. Ortegel, M. Krug, F. Henkel, C. Kurtsiefer, M. Weber, and H. Weinfurter. *Towards high-fidelity interference of photons emitted by two remotely trapped Rb-87 atoms*. Optics and Spectroscopy, **111** (4), 535–, 2011.

[63] D. Bouwmeester, J.-W. Pan, K. Mattle, M. Eibl, H. Weinfurter, and A. Zeilinger. *Experimental quantum teleportation*. Nature, **390** (6660), 575–579, December 1997.

[64] S. Olmschenk, D. N. Matsukevich, P. Maunz, D. Hayes, L. M. Duan, and C. Monroe. *Quantum teleportation between distant matter qubits*. Science, **323** (5913), 486–9, jan 2009.

[65] C. Nölleke, A. Neuzner, A. Reiserer, C. Hahn, G. Rempe, and S. Ritter. *Efficient Teleportation Between Remote Single-Atom Quantum Memories*. Phys. Rev. Lett., **110** (14), 140403–, April 2013.

[66] J. G. Rarity and P. R. Tapster. *Three-particle entanglement from entangled photon pairs and a weak coherent state*. Phys. Rev. A, **59** (1), R35–R38, January 1999.

[67] W. Rosenfeld, M. Weber, J. Volz, F. Henkel, M. Krug, A. Cabello, M. Zukowski, and H. Weinfurter. *Towards a Loophole-Free Test of Bell's Inequality with Entangled Pairs of Neutral Atoms*. Advanced Science Letters, **2** (4), 469–474, 2009.

[68] U. Schünemann, H. Engler, R. Grimm, M. Weidemüller, and M. Zielonkowski. *Simple scheme for tunable frequency offset locking of two lasers*. Review of Scientific Instruments, **70** (1), 242–243, January 1999.

[69] R. Garthoff. *Präparation von Lichtpulsen zur Interferenz mit Einzelphotonen emittiert von Rb-Atomen*. Bachelor's Thesis, Ludwig-Maximilians-Universität München, 2012.

[70] D. F. V. James, P. G. Kwiat, W. J. Munro, and A. G. White. *Measurement of qubits*. Phys. Rev. A, **64** (5), 052312–, October 2001.

[71] K. L. Corwin, S. J. M. Kuppens, D. Cho, and C. E. Wieman. *Spin-Polarized Atoms in a Circularly Polarized Optical Dipole Trap*. Phys. Rev. Lett., **83**, 1311–1314, Aug 1999.

[72] J. D. Thompson, T. G. Tiecke, A. S. Zibrov, V. Vuletić, and M. D. Lukin. *Coherence and Raman Sideband Cooling of a Single Atom in an Optical Tweezer*. Phys. Rev. Lett., **110**, 133001, Mar 2013.

[73] E. Wolf. *Electromagnetic Diffraction in Optical Systems. I. An Integral Representation of the Image Field*. Proc R Soc Lond A Math Phys Sci, **253** (1274), 349–, December 1959.

[74] B. Richards and E. Wolf. *Electromagnetic Diffraction in Optical Systems. II. Structure of the Image Field in an Aplanatic System*. Proc R Soc Lond A Math Phys Sci, **253** (1274), 358–, December 1959.

[75] A. Aspect, J. Dalibard, and G. Roger. *Experimental Test of Bell's Inequalities Using Time-Varying Analyzers*. Phys. Rev. Lett., **49**, 1804–1807, Dec 1982.

[76] J. F. Clauser and A. Shimony. *Bell's theorem. Experimental tests and implications*. Reports on Progress in Physics, **41** (12), 1881–, 1978.

[77] J.-Å. Larsson. *Loopholes in Bell inequality tests of local realism*. Journal of Physics A: Mathematical and Theoretical, **47** (42), 424003–, 2014.

[78] P. H. Eberhard. *Background level and counter efficiencies required for a loophole-free Einstein-Podolsky-Rosen experiment*. Phys. Rev. A, **47** (2), R747–R750, February 1993.

[79] A. Fedrizzi, T. Herbst, A. Poppe, T. Jennewein, and A. Zeilinger. *A wavelength-tunable fiber-coupled source of narrowband entangled photons*. Opt. Express, **15** (23), 15377–15386, 2007.

[80] P. Trojek and H. Weinfurter. *Collinear source of polarization-entangled photon pairs at nondegenerate wavelengths*. Appl. Phys. Lett., **92** (21), 211103–, May 2008.

[81] A. E. Lita, A. J. Miller, and S. W. Nam. *Counting near-infrared single-photons with 95% efficiency*. Opt. Express, **16** (5), 3032–3040, Mar 2008.

[82] W. K. Wootters and W. H. Zurek. *A single quantum cannot be cloned*. Nature, **299** (5886), 802–803, October 1982.

[83] J. Barrett, D. Collins, L. Hardy, A. Kent, and S. Popescu. *Quantum nonlocality, Bell inequalities, and the memory loophole*. Phys. Rev. A, **66** (4), 042111–, Oct 2002.

[84] T. Scheidl, R. Ursin, J. Kofler, S. Ramelow, X.-S. Ma, T. Herbst, L. Ratschbacher, A. Fedrizzi, N. K. Langford, T. Jennewein, and A. Zeilinger. *Violation of local realism with freedom of choice*. PNAS, **107** (46), 19708–19713, November 2010.

[85] K. Redeker. *Title to be announced*. PhD thesis, Ludwig-Maximilians-Universität München.

[86] J. Rohland. *Konfiguration und Test eines elektrooptischen Modulators mit Lithiumniobat-Kristall*. Bachelor's Thesis, Ludwig-Maximilians-Universität München, June 2012.

[87] D. Elkouss and S. Wehner. *(Nearly) optimal P values for all Bell inequalities*. Npj Quantum Inf., **2**, 16026–, October 2016.

[88] S. Blum, G. A. Olivares-Rentería, C. Ottaviani, C. Becher, and G. Morigi. *Single-photon frequency conversion in nonlinear crystals*. Phys. Rev. A, **88** (5), 053807–, November 2013.

[89] S. Zaske, A. Lenhard, C. A. Keßler, J. Kettler, C. Hepp, C. Arend, R. Albrecht, W.-M. Schulz, M. Jetter, P. Michler, and C. Becher. *Visible-to-Telecom Quantum Frequency Conversion of Light from a Single Quantum Emitter*. Phys. Rev. Lett., **109** (14), 147404–, October 2012.

[90] A. Lenhard, J. Brito, M. Bock, C. Becher, and J. Eschner. *Coherence and entanglement preservation of frequency-converted heralded single photons*. Opt. Express, **25** (10), 11187–11199, 2017.

[91] V. Letokhov. *Laser Control of Atoms and Molecules*. Oxford University Press Inc., New York, 2007.

Danksagung

Ich möchte mich an dieser Stelle noch bei allen Menschen bedanken, die mich bei der Arbeit unterstützt und mir diese überhaupt erst ermöglicht haben. Ganz besonders bedanken möchte ich mich bei:

- Prof. Harald Weinfurter für sein Vertrauen und die Möglichkeit an diesem spannenden Projekt zu arbeiten.
- Wenjamin Rosenfeld für all die Hilfe in den letzten Jahren und dafür, dass er immer Zeit für Fragen und Diskussionen gefunden hat.
- Markus Weber für seine Unterstützung in der Anfangszeit und seine mitreißende, fröhliche Art.
- Meinen Kollegen am Atom-Projekt, die mich durch diese Jahre begleitet haben: Julian Hofmann, Michael Krug, Norbert Ortegel, Kai Redeker, Robert Garthoff und Tim van Leent. Sowie bei allen anderen Mitgliedern der Arbeitsgruppe Weinfurter: Juliane Bahe, Jan Dziewior, Peter Freiwang, Florian Henkel, Lukas Knips, Lars Liebermeister, Jasmin Meinecke, Sebastian Nauerth, Markus Rau, Daniel Richart, Daniel Schlenk, Christian Schwemmer, Toshiyuki Tashima, Gwenaelle Vest und Martin Zeitlmair für die gute Arbeitsatmosphäre, der gegenseitigen Unterstützung und die gemeinsamen Aktivitäten.
- Frau Gschwendtner, Frau Schmidt und Herrn Scheich für ihre Hilfsbereitschaft.
- Und natürlich auch bei meiner Familie und meinen Freunden für den Rückhalt und die Motivation die diese mir während meiner Promotion gegeben haben.